Analysis of unsteady effects in fighter aircraft aerodynamics

Karthick Rajkumar

Vollständiger Abdruck der von der
Fakultät für Luft- und Raumfahrttechnik
der Universität der Bundeswehr München
zur Erlangung des akademischen Grades eines
Doktor-Ingenieurs (Dr.-Ing)
genehmigten Dissertation.

Gutachter:

1. Univ.-Prof. Dr.-Ing. habil. Markus Klein, Universität der Bundeswehr München
2. Prof. Dr. Peng Shia-Hui, Chalmers University Sweden

Die Dissertation wurde am 08.04.2024 bei der Universität der Bundeswehr München eingereicht und durch die Fakultät für Luft- und Raumfahrttechnik am 19.07.2024 angenommen. Die mündliche Prüfung fand am 13.09.2024 statt.

Declaration of Authorship

I, Karthick RAJKUMAR, declare that this thesis titled "Analysis of unsteady effects in fighter aircraft aerodynamics" and the research presented within it were entirely my own work carried out during my tenure as a research assistant at the University of the Bundeswehr Munich. By making this declaration, I confirm that:

- The research endeavours undertaken for this thesis were conducted by the academic standards and ethical guidelines set forth by the university.
- Any prior submissions of this thesis, whether for a degree at this university or any other institution, have been disclosed explicitly.
- Consistently clear and accurate attributions have been provided when referencing the works of others, ensuring proper acknowledgement of their contributions to the research.
- All materials quoted or derived from external sources are appropriately cited, upholding academic integrity and intellectual honesty.
- All primary sources of assistance and support received during the research process have been duly acknowledged, expressing gratitude for their invaluable contributions.

This declaration confirms an accurate reflection of the commitment to academic integrity and the responsible conduct of research.

Signed:

Date:

Abstract

The study encompasses an efficient CFD methodology for simulating weapon bay flows, which results in more than 90% computational efficiency than the commonly-used DES method and superior accuracy compared to the industry-standard RANS approach. In particular, several scale-adaptive simulation (SAS) variants are tested for an open cavity configuration under transonic conditions and compared against DES results and experimental data. The study investigates the efficacy of SAS models in predicting cavity spectra with high computational efficiency compared to wall-resolved DES models. Combining SAS with wall functions (SAS-WF) led to over-prediction of modal magnitudes due to strong vortical structures inside the cavity. In order to address this, a forcing feature was employed to resolve turbulent structures, yielding results comparable to wall-resolved SAS and reference DES results. It also explores Rossiter modes under sideslip conditions, revealing significant interference of waves in highly three-dimensional flow. It is observed that the skewed shear-layer dynamics primarily influence Mode 1, while higher modes exhibit fewer skewed shear-layer characteristics and include spanwise reflecting waves. Besides streamwise waves, there is notable wave interference in the spanwise direction due to flow impingement on the leeward door.

Furthermore, the study presents a detailed numerical investigation of double- and triple-delta wing configurations under transonic flow conditions using the k-ω SST and SAS turbulence models, focusing on leading-edge vortical flows. It investigates the responses of double-delta and triple-delta wings to vortex breakdown and shock buffet at an angle of attack of 20 degrees. The double-delta wing experiences shock-induced vortex breakdown, leading to transient adjustments in the shock position and resulting in a shock buffet. In contrast, the breakdown in the triple-delta wing is associated with a stationary shock induced by the wing's planform kink. Using the SAS model, a quasi-periodic oscillation of the pitching moment is observed in the triple-delta wing, revealing the evolution of the lambda shock. Analysis of the enstrophy transport equation suggests that the lambda-shock drives vortex breakdown in the double-delta wing. These findings highlight the complex interplay between shock-induced effects and vortex dynamics, providing insights into the aerodynamic behaviour of these wing planforms.

Kurzfassung

Die Studie befasst sich mit einer effizienten CFD-Methodik zur Simulation von Strömungsvorgängen in Waffenschächten, die den Bedarf an Rechenaufwand um mehr als 90% reduziert im Vergleich zum DES-Ansatz. Die Studie untersucht die Wirksamkeit der recheneffizienten skalenadaptiven Simulation-Modelle (SAS) bei der Vorhersage von Kavitätsspektren im Vergleich zu wandaufgelösten DES-Modellen. Die Kombination von SAS mit Wandfunktionen führte zu einer Überschätzung bei der Vorhersage der modalen Größen aufgrund starker Wirbelstrukturen innerhalb der Kavität. Um diese Problemstellung zu lösen, wurde eine Forcing-Funktion eingesetzt, um turbulente Strukturen aufzulösen, was zu Ergebnissen führte, die mit wandaufgelösten SAS und DES-Referenzdaten vergleichbar sind. Die Studie untersucht zudem Rossiter-Moden unter Sideslip-Bedingungen und zeigt, dass die erste Mode vorwiegend von der schiefen Scherschichtdynamik beeinflusst wird, während die höheren Moden weniger Merkmale einer schiefen Scherschicht aufweisen und Wellenreflexionen in Spannweitenrichtung beinhalten. Neben den Wellen in Strömungsrichtung gibt es eine bemerkenswerte Welleninterferenz in Spannweitenrichtung, die durch die Strömungseinwirkung auf die leeseitige Tür entstehen.

Außerdem wird eine numerische Untersuchung von Doppel- und Dreifach-Delta- Flügelkonfigurationen unter Verwendung der k-ω SST- und SAS-Turbulenzmodelle vorgestellt, wobei der Schwerpunkt auf Wirbelströmungen an der Vorderkante liegt. Es werden die Reaktionen von die Flügeln auf Wirbelzerfall und Stoßwellen bei einem Anstellwinkel von 20 Grad untersucht. Es wird festgestellt, dass der Doppel-Delta-Flügel einen schockinduzierten Wirbelabbruch erfährt, der zu vorübergehenden Anpassungen der Schockposition führt und ein Schockbuffet verursacht. Im Gegensatz dazu ist der Zusammenbruch beim Dreifach-Delta-Flügel mit einem stationären Schock verbunden, der durch den Knick in der Tragflächenform verursacht wird. Mit Hilfe des SAS-Modells wird eine quasi-periodische Oszillation des Nickmoments im Triple-Delta-Flügel beobachtet, die die Entwicklung des Lambda-Stoßes aufzeigt. Die Analyse der Enstrophie-Transportgleichung deutet darauf hin, dass der Lambda-Schock den Wirbelabbruch im Doppel-Delta-Flügel vorantreibt. Diese Ergebnisse verdeutlichen das komplexe Zusammenspiel zwischen stoßinduzierten Effekten und Wirbeldynamik und geben Einblicke in das aerodynamische Verhalten dieser Flügelformen.

Acknowledgements

I am grateful for the opportunity to conduct research at the Institute of Applied Mathematics and Scientific Computing within the Department of Aerospace Engineering at the University of Bundeswehr.

I extend my sincere appreciation to my supervisor, Univ.-Prof. Dr.-Ing. habil. Markus Klein, for his invaluable guidance throughout this endeavour. Special thanks to Dr. Eike Tangermann for his expertise in external aerodynamics, which greatly contributed to this work. Their consistent support and insightful discussions were instrumental in achieving our project's goals. I also want to acknowledge the collaboration of my office partner, Tony Di Fabbio, over the past four years.

I am thankful for the financial support provided by Airbus Defence and Space (ADS) for the project "Analysis of unsteady effects in fighter aircraft aerodynamics." Dr. Ketterl's assistance from ADS, especially during and after COVID-19, is highly appreciated, and it helped in successful collaboration through regular meetings. I am also grateful to my colleagues, staff and students for their support.

Furthermore, I appreciate the German Aerospace Center (DLR) granting access to the TAU code and Ennova Technologies for their meshing software. Special thanks to the Gauss Centre for Supercomputing for providing the necessary computing resources for this study.

Lastly, I extend my gratitude to my wife, Ashwini, for her unwavering support, patience, and love, which have been crucial throughout this demanding journey.

Contents

List of Figures

List of Tables

List of Abbreviations

ADS	Airbus Defense and Space
AoA	Angle of attack
AoS	Side slip angle
CFD	Computational Fluid Dynamics
CPU	Central Processing Unit
CFL	Courant-Friedrichs-Lewy number
CTU	Convective time units
DES	Detached Eddy Simulation
DES-WF	SA-IDDES model with wall-modelled approach
DNS	Direct Numerical Simulation
DLR	German Aerospace Center
DTS	Dual-time stepping scheme
DW1 and DW2	Double-delta wing and Triple-delta wing
FCAS	Future combat air system
FVS	Flux-vector splitting schemes
FVM	Finite volume method
FFT	Fast Fourier Transformation
IBV	Inboard vortex
(I)DDES	(Improved) Delayed Detached Eddy Simulation
k-ω SST	Menter k-ω Shear Stress Transport model
LE	Leading edge
LES	Large Eddy Simulation
LEV	Leading-edge Vortices
MBV	Midboard vortex
NACA	The National Advisory Committee for Aeronautics
NATO	North Atlantic Treaty Organization
NGWS	Next generation weapon system
OBV	Outboard vortex
PIV	Particle-Image Velocimetry

(U)RANS	Unsteady Reynolds averaged Navier-Stokes equations
RCS	Radar Cross Section
RMS	Root Mean Square
SA-IDDES	Spalart-Allmaras - Improved Delayed Detached Eddy Simulation
SA	Spalart-Allmaras one-equation model
SAneg	Spalart-Allmaras model with negative turbulent viscosity correction
SAnegRC	Spalart-Allmaras model with negative and Rotation/Curvature correction
SDIRK	Singly diagonally implicit Runge-Kutta method
SAS	Scale-adaptive Simulation
SAS-F	Scale-adaptive Simulation with wall modelled and forcing
SAS-WF	Scale-adaptive Simulation with wall-modelled approach
SAS-WR	Scale-adaptive Simulation with wall-resolved approach
SPL	Sound pressure level
STO	Science and Technology Organization
TWG	Transonic wind-tunnel in Göttingen
(U)RANS	(Unsteady) Reynolds Averaged Navier-Stokes
VB	Vortex breakdown

List of Symbols

Greek symbols

α	Angle of attack [°]
α_N	Angle of attack normal to leading-edge [°]
β	Side slip angle [°]
γ	Specific heat ratio
γ_{ij}	Kronecker delta
Γ	Diffusion coefficient
δ	Boundary-layer thickness $[m]$
ϵ	Turbulent dissipation rate $[m^2/s^3]$
$\epsilon_{(2,4)}$	Coefficients to control the amount of 2nd and 4th order dissipation
η	Kolmogorov scale $[m]$
θ	Phase delay constant
θ_t	Turbulent velocity scale $[m/s]$
θ_w	Wing sweep angle [°]
κ	von Karman constant
κ_c	Ratio of convection velocity of vortical structure to the free-stream velocity
κ_T	Thermal conductivity of the fluid $[W/mK]$
$\wedge$	Aspect ratio of wing
μ	Dynamic viscosity of the fluid $[Kg/ms]$
μ_o	Reference dynamic viscosity of the fluid $[Kg/ms]$
ν_t	Eddy viscosity $[m^2/s]$
ρ	Density of the fluid $[kg/m^3]$
ρ_∞	Free-stream density of the fluid $[kg/m^3]$
τ_{ij}	Viscous stress tensor $[N/m^2]$
τ_{ij}^R	Reynolds stress tensor $[N/m^2]$
τ_w	Wall-shear stress $[N/m^2]$
$\overline{\phi_i}$	RANS-averaged variable
$\widetilde{\phi_i}$	Mass-averaged variable

ϕ_1, ϕ_2, ϕ_3	Sweep angles of leading edges in DW1 and DW2 [°]
ϕ_{TE}	Sweep angle of trailing edge in DW1 and DW2 [°]
ω	Specific turbulence dissipation rate $[1/s]$
ω_i	Vorticity vector $[1/s]$

Latin symbols

c	Speed of sound $[m/s]$
C_r	Aerodynamic chord of DW1 and DW2 $[m]$
C_L	Lift coefficient
C_{m_x}	Rolling moment coefficient
C_{m_y}	Pitching moment coefficient
C_p	Pressure coefficient
D_c	Depth of the cavity $[m]$
E	Specific energy of a fluid $[J/Kg]$
f	Frequency $[Hz]$
$\overline{\overline{F}}$	Flux density vector
h	Specific enthalpy $[J/Kg]$
h_o	Specific total enthalpy $[J/Kg]$
i	Internal energy of a fluid $[J/Kg]$
k	Turbulent kinetic energy $[m^2/s^2]$
Kn	Knudsen number
l_t	Turbulent length scale $[m]$
l_1, l_2, l_3	Section lengths of leading edges in DW1 and DW2 $[m]$
L	Characteristic length scale $[m]$
$L1 - L8$	Measurement probe location in the cavity
L_{vK}	von Karman length scale $[m]$
L_c	Length of the cavity $[m]$
L_x	Distance from the leading edge of the cavity rig $[m]$
m	Mode number
Ma_N	Mach number perpendicular to leading edge
Ma_∞	Free-stream Mach number
n_i	Unit normal vector
p	Pressure $[N/m^2]$
p_∞	Free-stream pressure $[N/m^2]$
q_i	Heat flux vector $[W/m^2]$

R	Specific gas constant $[J/kgK]$
Re_∞	Free-stream Reynolds number
Re_{crit}	Critical Reynolds number
Ro	Rossby number
Re_x	Local Reynolds number
S_{ref}	Reference area $[m^2]$
S_{ij}	Strain rate tensor $[1/s]$
S_ϕ	Source terms in governing equations
t	Wing thickness $[m]$
t_i	Unit tangential vector
T_f	Temperature of the fluid $[K]$
T_o	Reference temperature of the fluid $[K]$
T_∞	Free-stream temperature of the fluid $[K]$
u, v, w	Instantaneous velocity components $[m/s]$
u_i	Instantaneous velocity components in index notation $[m/s]$
u', v', w'	Fluctuating velocity components $[m/s]$
u^+	Velocity scale in the near-wall region
u_τ	Friction velocity $[m/s]$
U	Characteristic velocity scale $[m/s]$
U_∞	Free-stream velocity $[m/s]$
U_{axial}	Maximum axial velocity at the vortex core $[m/s]$
U_{Ymax}	Maximum in-plane Y-velocity $[m/s]$
W_c	Width of the cavity $[m]$
$\vec{W}$	Vector of conservative variables
x, y, z	Cartesian coordinates
X, Y, Z	Cartesian coordinate axes
y^+	Non-dimensional wall distance

Chapter 1

Introduction

The development of newer aircraft incorporates the latest technological advancements, including stealth capabilities, advanced avionics, enhanced manoeuvrability, and increased range and speed. These developments ensure superiority over older models and potential adversaries. One significant project is the FCAS (Future Combat Air System) or NGWS (Next Generation Weapon System). It represents collaborative efforts among European countries to develop a new generation of fighter aircraft. FCAS aims to create an interconnected system comprising manned and unmanned aerial vehicles, stealth capabilities and enhanced network-centric warfare capabilities. It responds to the growing complexity of modern warfare and the need for interconnected, technologically advanced systems.
Predicting unsteady effects in fighter aircraft is essential because of the challenges new-generation fighter aircraft face. Computational fluid dynamics (CFD) is fundamental in predicting complex flow phenomena but remains expensive and challenging. The thesis discusses CFD-based analysis of unsteady effects in fighter aircraft aerodynamics for two critical applications: weapon bays and leading-edge vortices on hybrid-delta wing configurations.

1.1 Background

External weapons mounted on hardpoints under the wings or fuselage increase aerodynamic drag, reducing an aircraft's speed, manoeuvrability, and fuel efficiency. It leads to incorporating internal weapon bays, which contribute significantly to an aircraft's stealth profile by reducing its radar cross-section. By internally storing weapons, the aircraft's external surfaces remain smoother, reducing the number of protruding edges or surfaces that can reflect radar waves. This stealth capability allows the aircraft to operate with reduced detectability, enhancing its survivability in modern contested environments. However, several challenges arise when these bays are opened to release the payload.

During this process, the environment inside the bay becomes highly unsteady, which causes unpredictable oscillations in the payload and can lead to potential aero-elastic coupling issues. Additionally, there are high acoustic loads, with noise levels exceeding $160dB$. Resonant tones as high as $140dB$ can occur, potentially causing acoustic fatigue and damage to avionics equipment [1]. Furthermore, longitudinal pressure gradients may induce pitch-up moments on the payload after release. It could alter the payload's trajectory and sometimes lead to it colliding with the launching aircraft. The presence of these pressure fluctuations has been a driving force behind extensive research on cavities over the past six decades.

These challenges must be addressed or controlled for the safe and effective use of these weapon bays. It makes managing cavity flow problems a critical aspect of the design of many contemporary military aircraft. This emphasis on mitigating issues within the bay environment ensures that the release of stores remains as safe and efficient as possible, aligning with the stringent requirements of modern combat aircraft design.

Additionally, the development of low radar signature fighter aircraft requires the exploration of innovative airframe concepts to achieve reduced radar cross section (RCS) and superior flight performance, which delta wings with their swept leading edges are known to offer. On a delta wing, the vortices are generated over the leading edges, providing the aircraft with additional lift over a wide range of incidence angles. For instance, a delta wing with a 70° sweep can enhance its lift up to approximately 40° of the angle of attack [2]. In contrast, a steady NACA 0012 airfoil operating in two dimensions will achieve its peak lift at an angle of attack of approximately 15°. The balance between the vorticity generated at the leading edge and the vorticity convection over the wing makes the vortex stationary, responsible for the additional lift of a delta wing [2].

Two counter-rotating vortices observed on either side of the delta wing originate from separated shear layers near the leading edge. In the case of a wing with a rounded leading edge, Earnshaw and Lawford [3] noted that these vortices did not manifest until the angle of attack exceeded 5°. However, on a wing with a sharp leading edge, the separation vortices initiated at a lower angle of attack (as reported by Ericsson and Reding [4]). These leading-edge vortices, often called LE vortices, possess a transverse dimension of approximately half the wing's span. These spiralling vortices generate a substantial portion of the wing's lift, resulting in suction patterns on the wing's upper surface. Pressure measurements indicate that the regions of maximum suction coincide with the core regions of these vortices [5]. Fig. 1.1 depicts the open weapon bay of the F-22 Raptor aircraft, alongside a vortex formation observed over the F-35 aircraft.

Contemporary wing designs often exhibit moderate leading-edge sweep angles with

FIGURE 1.1: F-22 Raptor shows its weapon bay (left) [6] and a vortex forms around the body of the F35 aircraft (right) [7]

rounded, possibly spanwise-varying, leading-edge contours. Unlike traditional slender wings with sharp edges, the leading-edge vortices in these modern configurations are no longer geometrically fixed, making their characterization and prediction significantly more challenging.

1.2 Motivation

Weapon bays feature a highly unsteady and turbulent phenomenon related to combat aircraft configurations. Opening a weapons bay during transonic and supersonic flight generates a strong acoustic field comprising broadband and tonal noise. Rossiter has described these modes [8]. This, in consequence, leads to a highly complex, turbulent flow field with pressure oscillations that may induce fatigue or failure of structure and weapons [9]. A literature review suggests the following physical picture: As the shear layer hits the cavity rear wall, pressure waves are reflected inside the cavity. It generates robust and low-frequency cavity modes, which excite the shear layer motion and vice versa. Subsequently, the feedback further amplifies the resonance, and the cavity modes lock to their final frequencies [9]. The numerical simulation of this kind of flow is very complex and costly due to the inherent unsteady nature of turbulence. Lawson [10] has shown that Large Eddy Simulation (LES) and Detached Eddy Simulation (DES) can correctly predict cavity flows. Babu et al. [11] have successfully validated the Scale Adaptive Simulation (SAS) for square cavities with and without doors and demonstrated at the same time a significant reduction in CPU time compared to DES.

For engineering applications, even faster estimates of the amplitude and frequency of the cavity noise field would be an advantage and a few methods are reviewed in [10]. Another early approach is documented in [12], which is based on the Minimized Domain

CFD method. This method allows the collection of store force and moment data on a relatively small 'minimized' domain, which receives the boundary conditions from a separate baseline CFD solution of the entire aircraft. In this context, it is also worth mentioning that the presence of a store in the cavity does not alter the fundamental acoustic modes [13].

Another highly complex mechanism in delta-wing planforms is the formation and breakdown of vortex systems in sub- and transonic flows. For the flight dynamical stability and control of combat aircraft, the aerodynamic understanding of this process is fundamental for a successful aircraft design. The swept leading edges produce leading-edge vortices, which are highly turbulent and transient. At high angles of attack, vortex breakdown can occur, which leads to a loss of lift and introduces even more unsteady turbulence effects. Nowadays, the system of leading-edge vortices on slender delta wings with sharp leading edges is well understood. However, increased complexity, such as rounded leading edges, swept trailing edges, or multiple delta planforms, requires detailed simulations to reveal their flow physics. Individual configurations like the lambda-shaped SACCON within NATO RTO task group AVT-161 [14] or the diamond-shaped SAGITTA [15] have been investigated in research consortia and their flow physics are well documented. However, it is impossible to conclude the flow around new configurations from these individual configurations. A system of several leading-edge vortices can be produced by geometric variations, which then interact with each other.

For future aircraft configurations, predicting the system of leading-edge vortices and their interaction is likely to become very relevant. Control devices on the leading edge can modify the vortices in a desirable way [16]. Therefore, how the control device influences the entire vortex system and what its effect on flight dynamics needs to be known in detail since this prediction depends strongly upon the flow separation on the leading edge and the propagation of the turbulent vortex, high-fidelity turbulence-resolving approaches are necessary to capture the underlying flow phenomena accurately.

Understanding and predicting these crucial flow mechanisms of weapon bay and hybrid delta-wing configurations are vital for the successful design of modern fighter aircraft. Aiding these two industrially relevant design aspects by numerical simulations forms the core of this work.

1.3 Research Objectives

Specific to cavity flow, this thesis addresses the complex unsteady flow and acoustic field generated when opening weapons bays during transonic and supersonic flight. The primary goal is to develop a CFD methodology that balances efficiency, accuracy, and robustness. The scale-adaptive Simulation (SAS) model, known for its improved computational efficiency compared to DES, will be further studied in the context of cavity flows. The objective is to establish a more efficient approach for predicting cavity flows while maintaining accurate results.

The thesis's contribution to hybrid delta-wing airframes addresses the fundamental analysis of vortex flow phenomena on generic delta-wing planforms. The wide operating range of highly agile modern combat aircraft, ranging from sub- to supersonic conditions and including high angles of attack and side slip, can be ideally met by medium or low-aspect-ratio wing configurations. In particular, the flow field at transonic flow conditions is characterized by vortex formation and breakdown, vortex-vortex and vortex-shock interaction, which may influence longitudinal and lateral stability. This work investigates two different planforms of the ADS-NA2 configuration (DW1 and DW2). Besides standard analysis methods needed for comparison with experimental data, a variety of non-standard analysis tools are implemented in the postprocessing software Tecplot and Python. Examples include budgets of the vorticity transport equation illustrating transport, production and destruction of vorticity. The final assessment addresses vortices' effect on the aircraft's stability and control. Although the answers depend on the flow regime and configuration under consideration, the analysis of the whole dataset provides deeper insights to improve engineering rules to guide the design process.

The research relies on advanced CFD techniques, employing high-fidelity turbulence-resolving methods for accurate predictions and engineering-oriented models for efficiency. The methodology involves rigorous simulation studies and comparison with available experimental data and Airbus-provided information.

This thesis contributes to the aerospace engineering community by providing deeper insights into modern fighter aircraft design, cavity flow and leading-edge vortices on a delta wing. Investigating cavity flows will yield an efficient CFD methodology for predicting unsteady flow and acoustic characteristics, aiding in assessing potential fatigue, structural failure, and electronic component damage. Analyzing vortex systems on delta wing planforms will offer comprehensive insights into fighter aircraft stability, control, and design guidelines. By combining numerical simulations with experimental data, the thesis will advance the understanding of complex, unsteady aerodynamic phenomena,

guiding future aircraft design processes.

1.4 Outline of the Thesis

In this introductory overview, the chapters and their content have been outlined in the following manner.

Chapter 2: Fundamentals of cavity flows and delta-wing aerodynamics - This chapter is structured into two primary subsections, one dedicated to examining cavity flow and the other to analyzing Leading-Edge Vortices (LEV) over delta-wing planforms. Section 2.1 reviews various studies on cavity flows and their acoustic field analysis. It introduces the semi-empirical model introduced by Rossiter [8] and is followed by a list of studies that improved Rossiter's model by variation in assumptions from the original model. This part also describes various CFD methodologies followed in weapon bay flows and their accuracy and efficiency in predicting the acoustic modes. Section 2.2 introduces the past studies on leading-edge vortices. It describes the state-of-the-art understanding of the vortex system under subsonic, transonic and supersonic conditions. It summarises several studies undertaken to comprehend the vortex breakdown characteristics and its effect on aerodynamic stability.

Chapter 3: Theoretical background - This chapter introduces the flow governing equations, the Navier-Stokes equations, turbulence theory, and the Kolmogorov energy spectrum, followed by the law of the wall.

Chapter 4: Numerical approach - This chapter presents the numerical approach employed in this work, the Finite-volume method. The discretization procedure and schemes have been briefly explained. One of the most critical challenges in CFD is the treatment of turbulence, which is explained using different approaches and models that are employed in this work. Furthermore, near-wall treatment is explained in this chapter.

Chapter 5: Simulation configurations - This chapter introduces the two flow configurations simulated in this study, namely cavity and hybrid delta-wing configurations. Moreover, the meshing strategy and the simulation setup with the boundary conditions are shown for both flow configurations.

Chapter 6: Results of cavity flow - This chapter presents and analyses the results from the simulations of cavity flows. It discusses the implications of different simulation methodologies for predicting the acoustic field generated by weapons bays. Several turbulence approaches are compared, and guidelines for efficient turbulence treatments are summarized to predict cavity spectra.

Chapter 7: Results of leading-edge vortices on delta wings- This chapter provides insights into the characteristics of vortex systems for double- and triple-delta wing planforms. Reynolds Averaged Navier-stokes (RANS) based simulations are performed and validated with experimental data. Simulations show its ability to identify the vortex behaviour under various incidence angles. A few specific cases that involve vortex breakdown and vortex-shock interactions are then reviewed with scale-adaptive simulation, and its unsteady characteristics, namely vortex-vortex, vortex-shock interactions, and shock-buffet, are shown in detail. The final assessment of the planforms is addressed to identify the impacts of physical phenomena on the aerodynamic design considerations.

Chapter 8: Summary and Outlook This chapter summarises the research outcomes, achievements, and contributions to the design of modern combat aircraft. It discusses the limitations encountered during the study and proposes directions for future research.

Chapter 9: Publications This section comprehensively compiles all the works produced, encompassing journal papers, book chapters, and conference publications generated throughout the project.

Chapter 10: Appendices This chapter includes additional materials that support the primary content with supplementary simulation results.

Chapter 2

Fundamentals of cavity flows and delta-wing aerodynamics

Section 2.1 presents a comprehensive literature review of cavity flows. It shows the studies undergone to comprehend the physics behind resonance in open cavity configuration, followed by a series of studies dedicated to numerically predicting the modes with different turbulence modelling approaches. Section 2.2 reviews prior investigations into leading-edge vortices within the context of delta wing planforms. These investigations span a wide range, from modelling and simulation to gaining insights into the intricate flow dynamics over these planforms.

2.1 Cavity Flows and Acoustic Field Prediction

Cavities can be classified into three main types: closed, open and transitional flow [10]. A closed cavity is associated with shallow cavities, like those found in missile bays of military aircraft, and is usually defined by length-to-depth (L_c/D_c) ratios greater than 13. In a closed cavity, the incoming airflow separates from the front edge of the cavity but lacks sufficient energy to bridge the entire cavity. Consequently, the airflow attaches along the cavity floor at some point. Downstream, it separates from the floor again and reattaches at the trailing edge. This type of flow does not lead to the formation of acoustic tones. However, the region near the front wall experiences low pressure. In contrast, the region near the back wall experiences high pressure, potentially causing a nose-up pitching moment when a store is released. Open cavities are typically found in bomb bays, with L_c/D_c ratios less than or equal to 10. The incoming flow separates at the front edge of the cavity, forming a shear layer between the external flow and the flow within the cavity. This shear layer extends along the cavity's length and impinges on the rear wall. This configuration generates substantial circulation within the cavity, leading to a

uniform static pressure distribution along the cavity floor, with only a slight rise at the back wall. This even distribution is advantageous for safe store separation. However, the impingement of the shear layer on the back wall results in high-intensity acoustic tones, which can induce vibrations in the store and the surrounding cavity structure [10]. Finally, transitional flow occurs in the intermediate range between open and closed cavity flow. As the L_c/D_c ratio decreases from the closed cavity type, impingement and exit shocks merge into a single shock. However, significant longitudinal pressure gradients along the cavity persist, which can exert substantial pitching moments on a store.

In 1964, a study by Rossiter [8] was one of the foremost studies that provided a solid understanding of the physics-based acoustic-flow dynamic interaction for open-cavity configurations. He performed a series of wind tunnel experiments and found that the periodic pressure oscillation frequencies could be formulated in the semi-empirical model (Eq. 2.1). He envisioned that a physical phenomenon, similar to the generation of edge tones, arises from the periodic shedding of vortices at the front edge of the cavity and an acoustic source at the rear edge. This phenomenon gives rise to multiple periodic fluctuations characterized by frequencies within the $(m-\theta)$ sequence. When one of these components aligns closely with the natural frequency of the air volume within the cavity, resonance is triggered.

$$f = \frac{U_\infty}{L_c} \frac{m-\theta}{Ma_\infty + 1/\kappa_c} \tag{2.1}$$

In Eq. 2.1 f is the frequency, U_∞ is the freestream velocity, L_c is the length of the cavity, m is the mode number, θ is the phase delay constant, Ma_∞ is the Mach number and κ_c is the proportion of the free-stream speed at which the vortices travel over the cavity, in other words the ratio of convection velocity of vortical structure to the freestream velocity.

The resonant modes are predominantly longitudinal, and in simple rectangular configurations, their frequencies can be reasonably estimated using the semi-empirical Rossiter model. The Rossiter model is still widely used to predict the modes, particularly in the subsonic and transonic flow conditions. However, the model has shown some inaccuracies in supersonic flow conditions as the model assumes that the propagation speed of sound waves inside the cavity is equal to the freestream speed of sound. It introduces only a tiny error at low Mach numbers, but at high Mach numbers, the error is much greater [17]. Heller et al. [17] modified the Rossiter model by assuming that the speed of sound is equal to the freestream stagnation sound speed, thereby improving the model for a higher Mach number range (Eq. 2.2).

$$f = \frac{U_\infty}{L_c} \frac{m-\theta}{Ma_\infty/(\sqrt{1+(\gamma-1)Ma_\infty^2/2}) + 1/\kappa_c} \tag{2.2}$$

In general, appropriate values of the empirical parameters θ and κ_c, along with their relationship to flow conditions and L_c/D_c, remain unresolved. In particular, κ_c lacks a universally agreed-upon value and should depend on a range of variables such as Mach number Ma_∞, Reynolds number Re_∞, boundary layer thicknesses δ/D_c, δ/L_c, and other aspects of the cavity geometry [18].

Numerous investigators have conducted experimental visualizations of the waves propagating within the cavity. Handa et al. [19] conducted a study involving the visualization of pressure wave generation and propagation in a deep rectangular cavity during supersonic flow of $Ma_\infty = 1.7$, employing the Schlieren method. The investigation elucidated the underlying mechanisms responsible for pressure wave generation and tracked the trajectory of these waves. The findings revealed the presence of multiple compression waves propagating within the cavity, with particular emphasis on two waves directed toward the leading edge of the cavity. One of these waves originated from the trailing edge due to shear-layer motion, while the other resulted from the third reflection of the former wave at the rear wall. These waves, individually or collectively, stimulated the shear layer at the leading edge, playing a crucial role in the feedback mechanism governing self-sustained oscillations. The study, thus, provided a comprehensive understanding of the interplay between shear-layer motion, pressure-wave generation, and pressure oscillations within the cavity.

Wagner et al. [20] performed Particle image velocimetry (PIV) measurements to identify the flow structure associated with the cavity resonant tones. Tests were conducted at $Ma_\infty = 0.91$ within a cavity characterized by $L_c/D_c = 5.0$ and a square planform. The incoming turbulent boundary layer with a 99% boundary layer thickness represents approximately half of the cavity depth. The study showed the correlation of large-scale flow oscillations to the first Rossiter mode, while higher-order modes were correlated to the coherent structures generated in the shear layer.

The noteworthy observation in the study by Gloerfelt et al. [21] involves the alternating sizes of dominant structures within the shear layer. This alternation signifies a transition between modes I and II, corresponding to lower and higher frequencies in the spectra, respectively. Cattafesta et al. [22] extensively investigated this phenomenon using Schlieren photographs in a turbulent cavity flow setting ($L_c/D_c = 2$, $Ma_\infty = 0.4$, $Re_\infty = 2.5 \times 10^6$). Their findings reveal dynamic changes in the size of dominant structures over time, leading to switches between modes I, II, and III. This mode-switching behaviour is consistent with the variability in the number of vortices between the cavity corners, known as the Rossiter mode number. Comparative analyses with Lin and Rockwell's [23] cinema PIV sequence, conducted in a water flow with similar conditions ($L_c/D_c = 2$) and Reynolds number

based on momentum thickness, demonstrate remarkable similarities. Lin and Rockwell's time trace near the impingement corner indicates significant modulation between low and high-frequency components, further supporting the observed mode-switching phenomenon.

In the literature, there exist several cavity studies discussing the effect of different parameters on the acoustic spectrum, namely the L_c/D_c, Re_∞ and presence of stores from subsonic to supersonic flow conditions [17, 24, 25].

Woo et al. [24] studied the three-dimensional effects of supersonic cavity flow due to the variation of cavity aspect and width ratios using the RANS $k-\omega$ turbulence model. The compressible NS equations were solved with the 4^{th}-order Runge-Kutta method and the FVS method with van Leer's flux limiter. The study concluded the oscillation mode 2 appeared as a dominant oscillation frequency regardless of the aspect ratio of the cavity in the two-dimensional flow, and oscillation modes 1 and 2 appeared in three-dimensional cavities of small aspect ratios. With the increase in the aspect ratio or the width ratios, only the modes 2 or 3 appeared as a dominant frequency.

Conducting a direct computational analysis of the aerodynamic and acoustic fields by solving the compressible Navier–Stokes equations provides a means to explore the relationships among various factors. These factors include changes in flow structure, their interactions with the downstream edge, the behaviour of the separated shear layer, the internal recirculating flow, and alterations in flow conditions due to variations in geometry and flow parameters, all of which influence the generation of substantial radiated noise.

Gloerfelt et al. [21] conducted a Direct Numerical Simulation (DNS) of the two-dimensional compressible Navier-Stokes equations for a cavity with an aspect ratio of 2.0. Their investigation revealed the mechanisms behind lower frequency ranges, suggesting evidence of the possibility of mode-switching and robust coupling between the shear layer at the leading edge and the recirculation region forming within the cavity. Mode-switching is an additional complexity in the transient nature of resonating cavity flows. While a specific cavity flow may be linked to multiple tonal frequencies, these tones may not necessarily manifest simultaneously [26] .

Rowley et al. [27] conducted numerical analyses that reveal a transition in the behaviour of supersonic cavity flows. A shear-layer mode dominates for shorter cavities and lower Mach numbers, while a wake mode becomes prevalent for longer cavities and higher Mach numbers. The shear-layer mode is notably distinguished by the acoustic feedback process, as described by Rossiter. Disturbances in the shear layer align closely with predictions based on a linear stability analysis of the Kelvin-Helmholtz mode. On the other hand, the wake mode is characterized by large-scale vortex shedding, with the Strouhal number

remaining independent of the Mach number.

Several attempts have been made to study the cavity flows numerically. Although much of the cavity research has been experimental, numerical studies have shown to be an effective tool in understanding the spectra and using the information for flow control devices in real-world applications, such as modifications of the weapon bay. Numerical studies offer the advantage of higher temporal and spatial resolutions in data extraction than physical measurement techniques, and low-resolution wind-tunnel measurements help validate the numerical simulations.

Many early researchers have performed numerical studies based on the URANS approach due to its inexpensive nature. Zhang [28] conducted a computational study to analyze oscillations in compressible flow caused by shear layer instabilities in a cavity with a L_c/D_c ratio of 3. The analysis was carried out at Mach numbers of 1.5 and 2.5, and it involved solving the mass-averaged Navier-Stokes equations. Turbulence modelling was done using a $k-\epsilon$ model with adjustments for compressibility. The results indicated that self-sustained oscillations occurred. The patterns of interaction between shock waves and expansion waves, the oscillation modes, sound pressure levels, and the time-averaged surface pressure were compared to experimental data from previous studies. The study agreed well with the predictions and experimental results, especially for time-averaged pressure. It suggested a significant improvement over earlier analyses based on simple algebraic turbulence closure models.

Shih et al. [29] have obtained results from simulating the unsteady supersonic flow over an open cavity with a freestream Mach number of 1.5 and a Reynolds number of 1.09×10^6 using simultaneous implicit numerical solution of the strongly coupled $k-\epsilon$ and compressible Navier-Stokes equations. The periodic shedding of vortices from the front edge and the shear layer's deflection caused by pressure waves moving both upstream and downstream were observed throughout the oscillation cycle.

Henderson et al. [25] have performed numerical computations for different cavity flow types. They performed time-accurate simulations of the Reynolds-averaged form of the Navier-Stokes equations through the use of the $k-\omega$ model for predicting the acoustic spectra. They reported that the acoustic spectra at positions along the cavity floor predicted the experimental cavity tones, although RMS pressure levels were over-predicted compared with the experimental values. However, it has been shown that URANS models cannot predict the broadband spectra.

It is understood that due to the nature of the URANS formulation, the method is unable to detect modes accurately. The lower frequencies are usually predicted better than the higher frequencies. A wide range of scales present in the cavity makes it harder to predict by

modelling the entire spectra of turbulence. Therefore, several studies have been dedicated to scale-resolving turbulence models such as LES. The study by Larcheveque et al. [30] shows the accuracy of employing LES or DES methods for a 3D cavity case where doors are present and aligned vertically. Using the SA model, Chang et al. [31] studied 3D incompressible flow past an open cavity. Although the predictions of the mean velocity field from the URANS and the scale resolving simulation were similar, the study found that the URANS predictions show poor agreement with LES and experimental results for the turbulent quantities.

Wang et al. [32] performed numerical investigations to analyze oscillations in supersonic open cavity flows using a hybrid RANS-LES approach. Subsequently, simulations are carried out to identify and analyze the different oscillation regimes and feedback mechanisms in the supersonic cavity flows. The characteristics of the oscillations in the flow of Mach number of 1.75 are captured in the calculation, wherein a mixed shear-layer/wake oscillation mode is observed to occur alternately.

To characterize both the narrowband and broadband spectra, turbulence resolving methods such as DES methods based on Spalart-Allmaras (SA) and $k-\omega$ Shear Stress Transport (SST) have been employed and provided better results in predicting the broadband spectra than the URANS models in the M219 configuration [33].

Nayyar et al. [34] showed the superior performance of the LES and detached eddy simulation (DES) models in predicting the noise level, frequency content and velocity profiles inside the cavity with $L_c/D_c = 5.0$ and $W_c/D_c = 1.0$ in comparison to the URANS approach. They showed that over-predicted spectral values are expected for most URANS computations. To achieve reasonable behaviour with URANS, some studies, such as Stanek et al. [35], have tried to limit the production of eddy viscosity based on the values produced along the boundary layer, without which hardly any oscillatory behaviour was seen.

DES simulations are still expensive, whereas the scale adaptive simulation (SAS) approach developed by Menter [36] has shown results nearly as good as DES or LES. Girimaji et al. [37] evaluated the SAS of M219 cavity flows for transonic flow conditions. The SAS results showed good agreement with the experimental data for the M219 cavity at a tenth of the time required for DES computations.

Under the scope of cavity flow investigations, an open cavity configuration with opened doors presented in the work by Mayer et al. [39] has been studied numerically using the DLR-TAU CFD code [40] for transonic flow conditions using a hybrid RANS-LES approach based on Spalart-Allmaras based on the improved delayed DES (SA-IDDES)

model. A scale adaptive simulation was conducted to investigate the feasibility of efficiently simulating the cavity flows. The numerical simulations have been performed under the flow conditions of $Ma_\infty = 0.8$ and $Re_\infty = 12 \times 10^6$. The numerically computed RMS values and wall spectra have been validated against the experimental data, which have been made available for this study by Airbus Defence and Space [39]. This work shows investigations on the different wall treatments in the framework of SAS towards reducing the computational cost of simulating cavity flows, maintaining good accuracy relative to the hybrid RANS-LES results and experimental data. Furthermore, this work focuses on the detailed investigations of the SAS approach, including the synthetic forcing technique for predicting spectra for straight flow conditions [41]. The configuration is then further studied under sideslip flow conditions to understand the directional impact of flow processes on the resonant modes and their modulations. Investigations into the 3D visualization of the resonant modes, which have received limited attention, are featured in this work.

Despite the significant advancements in turbulence modeling, LES and DES approaches remain computationally prohibitive for large-scale 3D industrial simulations, especially in capturing the complex resonant modes in weapon-bay flows. As a result, the current thesis focuses on the more efficient SAS model to reduce computational time while still capturing key flow characteristics. However, the SAS approach has limitations in quasi-steady conditions due to its reliance on inherent flow fluctuations. To address this, an enhanced SAS model with artificial forcing (SAS-F), proposed by Menter et al. [38], introduces flow perturbations based on modeled turbulence scales to improve turbulence resolution.

While open cavity flows have been extensively studied, very few investigations have addressed the 3D effects introduced by lateral walls or explored the modulation of resonant modes under asymmetric flow conditions. The present study aims to bridge these gaps by extending the SAS approach to weapon-bay cavity flows and examining the influence of lateral wall effects under non-symmetric conditions. This approach not only contributes to understanding the physical features of resonating cavities but also explores a more computationally efficient turbulence modeling technique suitable for industrial applications.

2.2 Delta-wing aerodynamics

Highly agile, high-performance aircraft configurations must encompass various performance and manoeuvrability demands. These demands have led to aircraft configurations

such as double-delta, strake trapezoidal, or canard delta wings. These designs leverage controlled vortex flows, which develop over the wings, to achieve high lift and manoeuvrability [42]. They are predominantly featured in combat aircraft, primarily for their aerodynamic advantages, which enhance the aircraft's overall performance and capabilities. Swept leading edges in delta wings can provide better stability at high speeds, especially during manoeuvres. This stability is critical for combat aircraft to maintain control. Different types of combat aircraft, such as interceptors, multi-role fighters, and stealth aircraft, may use slightly different wing sweep angles to optimize their performance characteristics for their designated roles.

2.2.1 Classification of vortex systems

The flow characteristics of a delta wing are influenced by various geometric parameters such as wing sweep ϕ_w, aspect ratio $\wedge$, relative wing thickness t/C_r, relative leading edge or nose radius, and the geometry of the trailing edge. Freestream conditions, including Ma_∞, Re_∞, angle of attack α, and sideslip angle β, play significant roles in delta wing aerodynamics. Lee and Ho [43] provide a comprehensive review of the impact of all these parameters. Among these factors, wing sweep, angle of attack, and Mach number emerge as the predominant variables governing the flow over delta wings. Stanbrook and Squire [44] demonstrated that for flat delta wings with high sweep, the flow is primarily influenced by the angle of attack α_N and the Mach number Ma_N perpendicular to the leading edge. These parameters are defined as follows:

$$\alpha_N = \arctan \frac{\tan\alpha}{\cos\phi} \tag{2.3}$$

$$Ma_N = M_\infty \, cos\phi \, \sqrt{1 + \sin^2\alpha \, \tan^2\phi} \tag{2.4}$$

Miller and Woods have further expanded this work [45], who distinguished between six different regimes of attached and separated flow conditions for the lee-side flow of a flat delta wing: (1) Separation bubble with no shock, (2) Classical vortex system, (3) Vortex with shock, (4) Separation bubble with shock, (5) Shock-induced separation, and (6) Shock with separation. These regimes are observed for both subsonic and supersonic perpendicular Mach numbers Ma_N.

2.2.2 Development of leading-edge vortex systems

The primary flow field characteristics are governed by the formation and progression of two large-scale vortices emanating from the leading edges of the delta wing. Vortex generation initiates at relatively low angles of attack, originating from the rear portion of the wing and extending towards the apex. The separating shear layers from both the upper and lower surfaces of the wing roll up due to self-induction, culminating in forming a vortex above the wing. This primary vortex attains full maturity when vorticity is continuously supplied over the leading edge. Within the vortex core, there are notable characteristics such as high axial velocities, low static pressures, and heightened dissipation, resulting in reduced total pressures, particularly in the sub-core region due to steep gradients in cross-flow components. The presence of leading-edge vortices augments velocities along the wing's upper surface, generating a substantial suction force evidenced by local pressure minima marking the trajectory of the vortex axis on the wing's surface. Consequently, fully developed and stable leading-edge vortices contribute to enhanced lift and an expanded maximum angle of attack, thereby significantly improving the manoeuvrability of highly agile aircraft. Flow attachment lines are discernible inward of the vortex sheets, indicating that air is drawn over these sheets and directed downward. This phenomenon precipitates a lift increase at specific angles of attack, commonly referred to as non-linear or vortex lift [46]. Understanding the behaviour of these vortices during manoeuvres is pivotal to comprehending airflow dynamics. A spanwise pressure gradient induces separation of the flow moving outward from the wing surface, just beyond the primary vortex core, resulting in the formation of secondary and tertiary vortices [47]. The correlation between wing sweep and angle of attack delineates distinct ranges associated with the evolution of the primary vortex [48]. Initially, the primary vortex begins evolving from the rear portion of the wing towards the apex. Within this range, the primary vortex is confined to the rearward region of the wing and is not yet fully rolled up. In the second range, the fully developed vortex axis shifts inboard and upward as the angle of attack increases. The transition from the first to the second range is contingent upon boundary layer conditions, specifically whether the boundary layer is laminar or turbulent. For a given wing sweep, a laminar boundary layer results in the fully developed vortex occurring at a smaller angle of attack compared to the turbulent case. The subsequent range signifies the presence of a span-wise fixed vortex, where the vortex axis shifts upward with increasing angle of attack. Similar to the transition between the first two ranges, the transition from the second to the third range depends on the boundary layer condition. Notably, the span-wise fixed vortex only develops for wing sweeps larger than a certain

threshold value. The aerodynamic advantages stemming from leading-edge vortices become constrained when vortex bursting significantly impacts the flow over the wing. At moderate wing sweeps, vortex bursting persists over a broad range of angles of attack until the maximum angle of attack is attained. These delineated ranges of leading-edge vortex conditions profoundly influence the manoeuvrability of aircraft, particularly at moderate and high angles of attack. The average axial velocity is approximately symmetrical around the axis, with a maximum speed of four to five times greater than the free stream velocity. This behaviour has been attributed to Kelvin-Helmholtz-type instability within the shear layer. The unsteady Kelvin-Helmholtz instability has been observed through various methods, including flow visualization, hot-wire velocity measurements, particle image velocimetry measurements, and numerical simulations [49].

2.2.3 Vortex breakdown

Under subsonic conditions, as the angle of incidence is increased, the vortex undergoes sudden expansion, known as vortex breakdown, which was first observed during water tunnel tests of a slender delta wing planform by Werl'e [50]. The vortex breakdown can be characterized by rapid deceleration of both axial and swirl components of the velocity field. It results in loss of lift and pitching moment and causes adverse roll at sideslip and eventual loss of directional stability [51].

Various vortex breakdowns have been identified in vortex tube experiments [52]. The most common breakdown forms on wings are bubble and spiral. The bubble mode exhibits an axisymmetric structure with a swirl axis stagnation point and an oval-shaped circulation bubble. In contrast, the spiral mode involves rapid core flow deceleration, forming a persistent spiral before transitioning into large-scale turbulence. Vortex tube experiments show that the spiral type occurs at low swirl speeds, transforming into the bubble form at a critical swirl speed [53].

The onset and progression of vortex breakdown are influenced by two crucial parameters: the swirl level and the external pressure gradient along the vortex core. An increase in either of these factors accelerates the onset of breakdown. In the context of leading-edge vortices, these parameters are intricately linked to wing geometry, including factors such as incidence and sweep angle, as discussed by Gursul [49].

The sudden breakdown of the vortex can significantly affect the aerodynamic behaviour of the wing. In conditions involving sideslip, the vortex breakdown exhibits asymmetry, with the breakdown point positioned further upstream on the windward side compared to the leeward side, as discussed in [54]. These characteristics are responsible for typical

longitudinal, lateral, and directional instabilities, such as pitch-up, roll reversal, and directional divergence. These instabilities have been observed in generic low-aspect-ratio wing/body configurations and various high-performance aircraft designs. Addressing or eliminating these instabilities could potentially expand the operational flight envelope of such configurations [55].

Several studies have explored the causes of vortex breakdown, including hydrodynamic instability, wave propagation, and flow stagnation. These factors have been extensively discussed in the literature and are summarised in various review articles [56, 57, 58, 59]. Numerical studies have helped us further comprehend the cause of the vortex breakdown. However, predicting vortex flow and its breakdown comes with challenges. The position of the vortex is significantly influenced by a secondary vortex resulting from the interaction between the surface boundary layer and the primary vortex. Many turbulence models produce a disproportionately high level of turbulent viscosity within the core of the primary vortex, which significantly impacts the flow pattern and, in some instances, prevents the observed vortex breakdown at high Reynolds numbers [60]. Furthermore, in transonic flow conditions, shock further complicates the dynamics of the vortex system and its breakdown characteristics.

The study by Menke et al. [61] demonstrated various unsteady flow phenomena occurring across a delta wing and categorized non-dimensional frequency (fC_r/U_∞) ranges for different flow mechanisms. These included:

1. Aerodynamic manoeuvres within the frequency range of $0.001 - 0.015$.
2. Oscillation of the breakdown location within the frequency range of $0.01 - 0.1$.
3. Vortex shedding at a frequency of approximately 0.5.
4. Helical mode instability within the frequency range of approximately 1.0.
5. Kelvin-Helmholtz instability is occurring at frequencies higher than 10.0.

Previous experiments [62, 63] have established the instability of vortex breakdown location in the streamwise direction, acknowledging its transient nature. Primary breakdown location fluctuations occur at extremely low frequencies. Studying these fluctuations is vital for improving the stability and control of highly manoeuvrable aircraft, with significant implications for wing and tail buffeting. Evidence suggests that breakdown location oscillations play a crucial role in fin buffeting over a delta wing [64]. Gursul and Yang [65] investigated the possible link between breakdown location fluctuations and the hydrodynamic instability of the "breakdown wake." Contrary to expectations, the helical

mode instability in the breakdown wake did not influence breakdown location fluctuations. The breakdown location fluctuation spectrum indicated lower frequencies than the hydrodynamic instability, mainly concentrated below $fC_r/U_\infty = 0.2$. Additionally, the Kelvin—Helmholtz instability of the shear layer from the leading edge, with a frequency range of $fC_r/U_\infty = 6$ to 30, was found unrelated to breakdown location fluctuations. It underscores the distinct nature of breakdown location fluctuations independent of these hydrodynamic instabilities.

Present engineering methodologies for simulating unsteady fluid flows of delta wing configurations rely on the solution of the Reynolds-averaged Navier-Stokes (RANS) equations. Although they can be effective in steady flows, RANS turbulence models struggle to provide precise predictions for phenomena involving vortex breakdown because the turbulence models in the RANS approach model the entire spectrum of turbulence.

In response to the limitations of RANS models for predicting flows with substantial separation, Spalart [66] introduced DES as a numerical technique that combines the advantages features of both RANS models and LES. This method offers a solution that can be effectively applied at high Reynolds numbers, similar to RANS while resolving geometry-dependent and unsteady three-dimensional turbulent motions akin to LES. The primary strength of DES lies in its capability to predict complex flows accurately, making it particularly useful in scenarios like vortex breakdown over slender delta wings at high Reynolds numbers. DES enables the capture of higher turbulent frequencies within the flow, enhancing the ability to predict complex flow behaviours. While it offers significant accuracy gains, it is computationally demanding, making it prohibitive for many CFD users due to its reliance on grid and time-step independence.

One approach to address the aerodynamic instabilities is to manipulate the leading-edge vortex in creating a system of multiple interconnected leading-edge vortices. It can be achieved through the design of the wing's planform. By carefully varying the leading-edge sweep along the wing's span, it is possible to stimulate the formation of more than one leading-edge vortex. The proximity of these vortices leads to their interaction, which, in turn, affects their characteristics. This interaction is intended to induce a stabilizing influence on the vortex system, ultimately enhancing overall aerodynamic stability. However, effectively harnessing vortex interaction necessitates a thorough understanding of the underlying flow physics. More complex planforms, such as double and triple delta-wing planforms in subsonic flow conditions, were studied by Pfnür et al. [67], which focused on investigating the interactions between inboard and mid-board vortex structures, as well as analyzing the properties and trajectories of these vortices. The study revealed that the breakdown behaviour associated with distinct vortex types exerted varying effects on the

stability of the mid-board vortex. Notably, both planforms exhibited significant instabilities in the medium to high angle-of-attack regimes. However, the onset and magnitude of instability were notably reduced for the triple-delta wing configuration.

In an attempt to determine the underlying theory behind vortex breakdown, numerous studies have been undertaken, primarily focusing on simple geometries such as torsionally driven cylinders and closed pipes. This research investigation has been gaining interest since Peckham [68] first observed this phenomenon over a delta-wing planform. In the context of straightforward geometric configurations, the breakdown phenomenon of an axisymmetric vortex is linked to the localized trapping and amplification of disturbances within the vortex core. Nevertheless, some researchers have raised doubts about whether the phenomenon observed in torsionally driven cylinders should be classified in the same category as that occurring over delta wings, as articulated by Darmofal in 1994 [69].

In transonic flow conditions, the breakdown position suddenly moves toward the apex as the angle of incidence increases. It was observed by Schiavetta et al. [70] over a 65° sharp edge delta-wing. They determined that the shock/vortex interaction was the cause of the sudden motion, and the presence and effect of this interaction were studied in terms of the Rossby number of the vortex and the axial flow properties. Furthermore, they found that the movement of the breakdown location is sensitive to the balance between vortex strength, axial flow and shock strength. However, in the context of shock interaction with the vortex system, there needs to be more emphasis on the unsteady aspects of these vortical flows, which impact aircraft stability and control [71]. For instance, shock-induced vortex breakdown is a transient phenomenon. It has a direct impact on the pitching moment coefficient. Understanding it might serve to control the stability of the aircraft better and ensure high manoeuvrability.

Despite significant advancements in developing the fundamental theory of vortex breakdown, this understanding has yet to yield effective control measures. Current control strategies rely on manipulating the vortex swirl ratio or the pressure gradient above the wing [72]. While these methods exhibit varying degrees of effectiveness, they need to leverage an understanding of the breakdown mechanism. A noteworthy contribution by Rusak and Lamb [73] demonstrated that the swirl ratio (defined as the ratio of the maximum azimuthal velocity to the maximum axial velocity within the vortex), previously utilized to indicate the susceptibility of flow to breakdown in open pipes, could be employed to predict the onset and location of breakdown over slender delta wings.

A study by Jones et al. [74] successfully confirmed the vorticity dynamics linked to vortex breakdown above a delta wing with less complex geometries. Additionally, the study demonstrated that the presence of negative azimuthal vorticity serves as an indicator for

the initiation of vortex breakdown. Moreover, the investigation delved into the mechanism responsible for generating this negative azimuthal vorticity and highlighted the role of radial vorticity turning, which opposes the onset of breakdown and the turning of axial vorticity into the azimuthal direction appears to be the main contributor to the onset of vortex breakdown.

A research initiative focused on investigating vortex interaction effects was led by Airbus Defence and Space (ADS), in collaboration with the German Aerospace Center (DLR). Within this initiative, double and triple-delta wing planforms referred to DW1 and DW2 in this study, were defined. The configuration under examination entails a generic low-aspect-ratio wing-fuselage setup, with active participation in the NATO AVT-316 task group titled "Vortex Interaction Effects Relevant to Military Air Vehicle Performance" [75, 76, 77]. Several studies have been undertaken to study these configurations over a range of subsonic and transonic Mach numbers [78, 79, 80]. These planforms are especially significant for combat aircraft, as they frequently encounter high angle of attack situations, requiring designs that ensure stability and control even in extreme flight conditions. The investigations encompasses alterations in geometry and flow conditions, with distinct wing sweep angles significantly amplifying flow intricacy. The geometric disparity at the leading edge results in the generation of vortices, each exhibiting differences in strength, stability, and characteristics, influenced by the sweep angles of their origin. Moreover, these vortices interact or combine in diverse manners contingent upon the angles of attack and side-slip.

Hövelmann et al. [78] conducted a joint experimental and numerical investigation employing URANS computations to analyze the aerodynamics of a generic triple-delta wing configuration at transonic velocities. The primary focus was on comprehending vortex flow phenomena, encompassing vortex development, vortex-vortex, and vortex-shock interactions. The research outcomes encompassed flow conditions at Mach numbers of 0.5 and 0.85, encompassing various angles of attack (up to 40°) and non-symmetric flows, including non-null side-slip angles. The findings indicate that the experimental and computational results generally concur at lower to medium angles of attack. However, discrepancies arise as the angle of attack increases, particularly concerning the prediction of vortex breakdown effects. These disparities are more evident in lateral motion scenarios, where experimental and numerical results highlight differing predictions of vortex breakdown effects.

Pfnür et al. [67] studied the double and triple delta-wing planforms in subsonic flow conditions, focusing on investigating the interactions between inboard and midboard vortex structures, as well as analyzing the properties and trajectories of these vortices. The

study revealed that the breakdown behaviour associated with distinct vortex types exerted varying effects on the stability of the midboard vortex. Notably, both planforms exhibited significant instabilities in the medium to high angle-of-attack regimes, but their onset and magnitude were notably reduced for the triple-delta wing configuration.
Previous study by Di Fabbio et al. [81] simulated the triple-delta wing planform and compared the performance of different turbulence approaches by analyzing different chord-wise locations and local surface pressure distribution. We showcased the capability of $k-\omega$ SST and SAS models to predict the aerodynamic coefficients more effectively than RANS models such as SA-negRC.
Under the scope of delta-wing aerodynamics, this study mainly focuses on investigating the physical aspects of vortex produced over the wing configurations. The flow around the double-delta wing DW1 is simulated using the $k-\omega$ SST RANS model and the SAS turbulence modeling approach to analyze the transient flow characteristics occurring over the wing. The simulations are conducted in the transonic regime at $Ma_\infty = 0.85$ and $Re_\infty = 12.53 \times 10^6$ with a sideslip angle of $\beta = 5^\circ$.
While previous studies have explored delta-wing aerodynamics, the current research addresses specific knowledge gaps:

- **Vortex-Vortex and Vortex-Shock Interactions**: Although many studies have focused on delta-wing aerodynamics, there is a lack of comprehensive investigations into the intricate vortex-vortex and vortex-shock interactions and their impact on the flow physics over double-delta and triple-delta wings, especially under transonic flow conditions.

- **Shock-Buffet and Its Relation to Vortex Dynamics**: Limited attention has been given to the impact of shock-buffet phenomena on the strength and stability of vortices, particularly for wings with different leading-edge sweep angles. This study aims to uncover the physical mechanisms behind vortex strength, shock position, and orientation, which have critical implications for aircraft design.

- **Vorticity Transport Analysis**: The use of vorticity transport terms to analyze vortex dynamics is not extensively covered in current literature. The present work will provide new insights into how these mechanisms influence vortex behavior over the delta wing configurations.

In summary, this research contributes to a deeper understanding of the transient flow physics, such as vortex-vortex and vortex-shock interactions, and highlights their potential significance in improving aerodynamic design and performance of transonic aircraft.

Chapter 3

Theoretical background

This chapter presents the governing equations of mass conservation, momentum conservation, and energy conservation, followed by an explanation of turbulent flows and boundary layer theory.

3.1 Flow governing equations

This section introduces the mathematical representation of the fundamental physical aspects of compressible fluid dynamics. It adopts a continuum approach, assuming a Knudsen number $Kn \ll 1.0$, allowing the study of fluid behaviour using macroscopic properties like velocity u_i, pressure p and density ρ. For practical considerations, air is treated as a Newtonian fluid characterized by a linear relationship between the viscous stresses at any given point and the local strain rate. This characteristic simplifies the mathematical modelling process. The mathematical framework for the fluid flow model is established by deriving it from the foundational laws of motion applied to infinitesimal fluid volumes. These laws encompass mass conservation, momentum conservation, and energy conservation principles. The continuity equation states that the increase of mass in the infinitesimal finite volume equals the net rate of flow of mass into the fluid element. This law is established as a differential equation for an unsteady compressible flow as

$$\frac{\partial \rho}{\partial t} + \frac{\partial (\rho u_i)}{\partial x_i} = 0 \, . \tag{3.1}$$

The momentum equation is derived from Newton's second law of motion applied to the infinitesimal finite volume of fluid flow. It states that the rate of increase of momentum of a fluid particle is balanced by the sum of forces on the fluid particle. There are two types of forces on fluid particles: surface forces (such as pressure, viscous, and gravity) and body forces. This law is defined as a non-linear partial differential equation for an unsteady

compressible flow in the absence of body forces as

$$\frac{\partial(\rho u_i)}{\partial t} + \frac{\partial(\rho u_i u_j)}{\partial x_j} = -\frac{\partial p}{\partial x_i} + \frac{\partial \tau_{ij}}{\partial x_j} \,. \tag{3.2}$$

In Eq. 3.2, a fluid element's stress state is determined in terms of the pressure and the six viscous stress components τ_{ij}. The pressure, a normal stress, is denoted by p. Viscous stresses are denoted by τ_{ij}. The suffices i and j in τ_{ij} indicate that the stress component acts in the j-direction on a surface normal to the i-th direction.
The energy equation is derived from the first law of thermodynamics, which states that the rate of energy increase of a fluid particle within an infinitesimal control volume equals the net rate of heat added to the fluid particle and the net rate of work done on the fluid particle. Eq. 3.3 represents the total energy balance in the control volume for a compressible Newtonian fluid.

$$\frac{\partial(\rho E)}{\partial t} + \frac{\partial(\rho u_i E)}{\partial x_j} = -\frac{\partial(p u_i)}{\partial x_i} + \frac{\partial(\tau_{ij} u_i)}{\partial x_j} - \frac{\partial q_j}{\partial x_j} \,. \tag{3.3}$$

In Eq. 3.3, the term $E = i + \frac{1}{2}(u_i u_i)$ denotes specific energy, representing the combined internal energy i and mechanical kinetic energy. The heat flux vector, q_i, is defined by Fourier's law as

$$q_i = \kappa_T \frac{\partial T_f}{\partial x_i} \tag{3.4}$$

where κ_T signifies the thermal conductivity of the fluid and T_f is the temperature of the fluid. Specific enthalpy, h, and specific total enthalpy, h_o, are defined as

$$h = i + \frac{p}{\rho} \quad \text{and} \quad h_o = h + \frac{1}{2}(u_i u_i) \,. \tag{3.5}$$

Combining these definitions with that of specific energy, E, yields

$$h_o = i + \frac{p}{\rho} + \frac{1}{2}(u_i u_i) = E + \frac{p}{\rho} \,. \tag{3.6}$$

In the set of governing equations for compressible flow, four vital thermodynamic variables remain unknown: pressure (p), density (ρ), internal energy (i) and temperature (T_f). Building connections between these variables is predicated on the assumption of thermodynamic equilibrium. Equations of state play a pivotal role in linking the energy equation to mass conservation and momentum equations. This linkage stems from density alterations arising due to fluctuations in pressure and temperature throughout the flow

field. When dealing with a perfect gas, the following widely recognized state equations prove valuable.

$$p = \rho R T_f \quad \text{and} \quad i = C_v T_f \tag{3.7}$$

The momentum equation (Eq. 3.2) introduces additional variables represented by the viscous stress components τ_{ij}. In formulating conservation equations for fluid flows, incorporating a model for these viscous stresses is often advantageous. In many fluid flow scenarios, expressing viscous stresses as functions of the local deformation rate proves beneficial. For a Newtonian fluid, the viscous stresses are directly related to the rate of deformation according to Newton's law of viscosity

$$\tau_{ij} = 2\mu S_{ij} - \frac{2}{3}\delta_{ij}\frac{\partial u_k}{\partial x_k} \tag{3.8}$$

with μ representing the dynamic viscosity, and S_{ij} denotes the viscous strain-rate tensor, defined as

$$S_{ij} = \frac{1}{2}\left(\frac{\partial u_i}{\partial x_j} + \frac{\partial u_j}{\partial x_i}\right) . \tag{3.9}$$

In Eq. 3.8, the dynamic viscosity is determined by Sutherland's law, establishing its dependence on temperature, expressed as

$$\frac{\mu}{\mu_0} = \left(\frac{T_f}{T_0}\right)^{3/2} \frac{T_0 + 110.4\ \text{K}}{T + 110.4\ \text{K}} \tag{3.10}$$

where $\mu_0 = 1.7894 \times 10^{-5} kg/ms$ represents the reference viscosity at the reference temperature $T_0 = 288.16$ K.

Speed of sound The freestream Mach number, Ma_∞, is a crucial parameter in fluid dynamics, particularly in situations where fluid compressibility becomes significant. It is defined as the ratio of the speed of an object moving through a medium to the speed of sound in that medium. If the Ma_∞ is higher than 0.3, the variation in density must be considered in the flow fields. This variation in density is a consequence of the compressibility effects and needs to be considered in analyzing the flow fields accurately. Neglecting these variations can lead to inaccurate predictions and analyses of fluid flow at high speeds.

$$Ma_\infty = \frac{U_\infty}{c} \tag{3.11}$$

For a perfect gas, the speed of sound depends only on the temperature of the gas as follows

$$c = \sqrt{\gamma R T_f} \tag{3.12}$$

with $\gamma = 1.4$ for air.

3.2 Turbulent flows

The Reynolds number serves as a metric for assessing the importance of inertia forces relative to viscous forces [82]. Experimental studies of fluid systems have revealed that below a certain critical Reynolds number, denoted as Re_{crit}, the flow maintains a smooth character, with neighbouring fluid layers exhibiting an orderly sliding motion past one another. Under conditions of constant boundary constraints over time, this flow type is characterized as laminar flow. It is defined as

$$Re = \frac{\rho U L}{\mu} \tag{3.13}$$

where U and L represent characteristic velocity and length scales, respectively. As the Reynolds number exceeds Re_{crit}, a complex sequence of events unfolds, ultimately drastically altering the flow's behaviour. The flow becomes inherently unsteady in this regime, known as turbulent flow. Velocity and other flow properties fluctuate randomly and chaotically. Turbulent fluctuations manifest in all three dimensions. Moreover, visualizations of turbulent flows unveil rotational flow structures termed turbulent eddies, which exhibit a broad spectrum of length scales. The largest eddies engage with and extract energy from the mean flow through a phenomenon known as vortex stretching. The characteristic velocity and characteristic length of larger eddies align closely with the velocity scale U and length scale L of the mean flow. Consequently, forming a 'large eddy' Reynolds number by incorporating these eddy scales with kinematic viscosity results in a significant value across all turbulent flows, indicating dominance by inertia effects with negligible influence from viscosity. These large-scale motions progressively fragment into smaller eddies due to

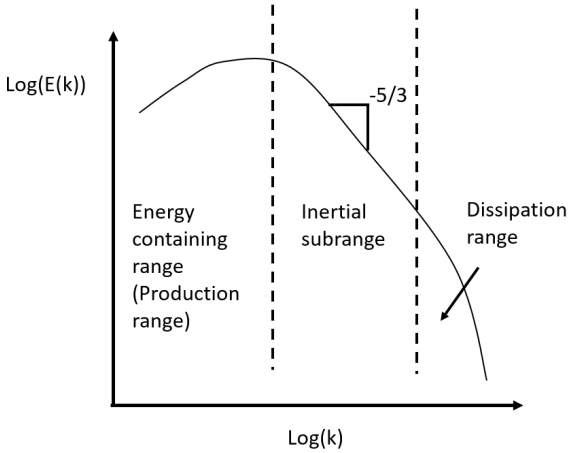

FIGURE 3.1: Kolmogorov energy spectrum [83]

turbulence's chaotic and nonlinear interactions. As energy transfers from larger eddies to smaller ones, kinetic energy redistributes across a spectrum of length scales. Kolmogorov's turbulence theory delineates an inertial subrange, where viscosity's effects pale compared to inertial forces across a range of length scales. Turbulent kinetic energy cascades down length scales within this subrange through interactions among turbulent eddies. Larger eddies transfer energy to smaller ones through stretching, shearing, and rotation interactions. This energy transfer persists until it reaches the Kolmogorov microscale, where viscous effects dissipate energy into heat. A schematic representation of the Kolmogorov spectrum [83] is depicted in Fig. 3.1.

3.3 Law of the wall

In this subsection, the near-wall behaviour of the fluid has been explained shortly. The effect of viscosity at high Reynolds numbers is confined to a very thin layer in the immediate neighbourhood of the solid wall. Due to the adherence of the fluid to a solid wall, the flow near the wall is retarded by the frictional forces. In this thin layer, the velocity of the fluid increases from zero at the wall to its full value away from the wall [84]. Cavity flow and leading-edge vortices involve flat-plate walls, and viscosity's effect in the near-wall regions is paramount. This theory is crucial for the cavity flow because of its importance in predicting the turbulent spectra. The following non-dimensional scales are used when dealing with boundary layer theory.

$$y^+ = \frac{y u_\tau}{\nu} \quad \text{and} \quad u^+ = \frac{u}{u_\tau} \tag{3.14}$$

In Eq. 3.14, y is the distance of the fluid volume away from the solid wall, y^+ is the dimensionless wall coordinate, u^+ is the velocity scale defined near the wall region, u is the mean velocity parallel to the wall and u_τ is the friction velocity defined as follows,

$$u_\tau^2 = \frac{\mu}{\rho}\left(\frac{\partial u_i}{\partial x_j} + \frac{\partial u_j}{\partial x_i}\right) n_j t_i \tag{3.15}$$

In Eq. 3.15, n_j represents the components of the normal to the surface outward unit vector and t_i represents the components of the unit tangential vector to the surface. According to Lumley et al., [85], the near-wall region can be virtually split into three regions based on y^+ values.

1. Viscous sublayer ($0 < y^+ < 5$) In the viscous sublayer, viscous stresses are higher than inertial ones. In the viscous sublayer, the flow is unsteady, but the velocity fluctuations do not contribute much to the total stress because of the viscosity.

$$\tau_w = \mu \frac{du}{dy} \tag{3.16}$$

   Using the definition of y^+ and u^+, Eq. 3.16 can be written as

$$u^+ = y^+ \tag{3.17}$$

2. Buffer layer ($5 < y^+ < 30$) The contribution of viscous and inertial forces is even in the buffer layer. Hence, neither of the forces can be neglected. This layer has maximum turbulent production and large variations in the turbulence source terms. This is the layer where the linear velocity in the viscous layer and the logarithmic velocity profile in the inertial sublayer are linked.

3. Logarithmic layer ($30 < y^+ < 100$) In this layer, the inertial forces are higher than the viscous forces and non-dimensional velocity u^+ follows a logarithmic pattern.

$$u^+ = \frac{1}{\kappa} ln y^+ + B \tag{3.18}$$

   In Eq. 3.18, κ is the von Karman constant equal to 0.41, and B is an empirical constant equal to 5.1.

Chapter 4

Numerical approach

The Finite Volume Method (FVM) is a numerical approach that discretizes partial differential equations representing conservation laws over discrete volumes. Like finite difference and finite element methods, it begins by discretizing the geometric domain into non-overlapping volumes. The partial differential equations are then transformed into algebraic equations by integrating them over each volume. The resulting system of algebraic equations is solved to determine dependent variable values for each volume. The FVM exhibits strict conservation due to treating some terms as face fluxes, making it a preferred method in Computational Fluid Dynamics (CFD). Notably, it accommodates unstructured polygonal meshes and allows straightforward implementation of boundary conditions. These attributes make the FVM well-suited for simulating fluid flow, heat, and mass transfer, evolving from simple physics on structured grids to handling complex applications in modern CFD.

4.1 General formulation of FVM

In this investigation, numerical simulations were conducted using the DLR-TAU code, a three-dimensional, parallel, hybrid finite volume code developed by the German Aerospace Center [40]. If we introduce a general variable ϕ, the conservative form of all fluid flow equations can usefully be written as [86]

$$\frac{\partial(\rho\phi)}{\partial t} + \frac{\partial(\rho\phi u_i)}{\partial x_i} = \frac{\partial}{\partial x_i}(\Gamma\frac{\partial\phi}{\partial x_i}) + S_\phi \tag{4.1}$$

which signifies that the combined effect of the rate of increase of ϕ within a fluid element and the net flow rate of ϕ out of the fluid element is equivalent to the sum of the rate of increase of ϕ due to diffusion and the rate of increase of ϕ due to sources. This equation serves as the initial point for computational procedures in the FVM. By setting ϕ to

1, u_i, h_o, the diffusion coefficient Γ, and appropriate source terms S_ϕ, we derive five partial differential equations governing mass, momentum, and energy conservation. The integration of Eq. 4.1 over a three-dimensional control volume V yields

$$\int_V \frac{\partial(\rho\phi)}{\partial t} dV + \int_V \frac{\partial(\rho\phi u_i)}{\partial x_i} dV = \int_V \frac{\partial}{\partial x_i}(\Gamma \frac{\partial \phi}{\partial x_i}) dV + \int_V S_\phi dV \ . \tag{4.2}$$

The volume integrals within the second term on the left-hand side (the convective term) and the first term on the right-hand side (the diffusive term) are reformulated as integrals across the entire bounding surface of the control volume, employing Gauss's divergence theorem as

$$\frac{\partial}{\partial t}\Big(\int_V (\rho\phi) dV \Big) + \int_S n_i \cdot (\rho\phi u_i) dS = \int_S n_i \cdot (\Gamma \frac{\partial \phi}{\partial x_i}) dS + \int_V S_\phi dV \ . \tag{4.3}$$

4.2 Application of FVM to NS equations

The Navier-Stokes equations for the three-dimensional case can be written in conservative form as

$$\frac{\partial}{\partial t} \iiint_V \vec{W} \, dV = - \iint_{\partial V} \overline{\overline{F}} \cdot \vec{n} \, dS \tag{4.4}$$

where

$$\vec{W} = \begin{pmatrix} \rho & \rho u_1 & \rho u_2 & \rho u_3 & \rho E \end{pmatrix}^\top \tag{4.5}$$

is the vector of the conserved quantities. V denotes an arbitrary control volume with the boundary ∂V and the outer normal $\vec{n}$. The flux density tensor $\overline{\overline{F}}$ is composed of the flux vectors in the three coordinate directions

$$\overline{\overline{F}} = (\vec{F}_i^c + \vec{F}_v^c) \cdot \vec{e_1} + (\vec{G}_i^c + \vec{G}_v^c) \cdot \vec{e_2} + (\vec{H}_i^c + \vec{H}_v^c) \cdot \vec{e_3} \tag{4.6}$$

with $\vec{e_1}$, $\vec{e_2}$ and $\vec{e_3}$ being unit vectors in the coordinate directions. The i and ν denote the inviscid and the viscous contributions, respectively. The viscous and the inviscid fluxes are

$$\vec{F_i}^c = \begin{pmatrix} \rho u_1 & \rho u_1^2 + p & \rho u_1 u_2 & \rho u_1 u_3 & \rho H u_1 \end{pmatrix}^\top \tag{4.7}$$

$$\vec{F_v}^c = -\begin{pmatrix} 0 & \tau_{11} & \tau_{12} & \tau_{13} & u_1\tau_{11} + u_2\tau_{12} + u_3\tau_{13} + \kappa_l \frac{\partial T}{\partial x_1} \end{pmatrix}^\top \tag{4.8}$$

$$\vec{G_i}^c = \begin{pmatrix} \rho u_2 & \rho u_1 u_2 & \rho u_2^2 + p & \rho u_1 u_3 & \rho H u_2 \end{pmatrix}^\top \tag{4.9}$$

$$\vec{G_v}^c = -\begin{pmatrix} 0 & \tau_{12} & \tau_{22} & \tau_{23} & u_1\tau_{12} + u_2\tau_{22} + u_3\tau_{23} + \kappa_l \frac{\partial T}{\partial x_2} \end{pmatrix}^\top \tag{4.10}$$

$$\vec{H_i}^c = \begin{pmatrix} \rho u_3 & \rho u_1 u_3 & \rho u_2 u_3 & \rho u_3^2 + p & \rho H u_3 \end{pmatrix}^\top \tag{4.11}$$

$$\vec{H_v}^c = -\begin{pmatrix} 0 & \tau_{13} & \tau_{23} & \tau_{11} & u_1\tau_{13} + u_2\tau_{23} + u_3\tau_{33} + \kappa_l \frac{\partial T}{\partial x_3} \end{pmatrix}^\top . \tag{4.12}$$

The temporal change of the conservative variables $\vec{W}$ can be derived as

$$\frac{\partial}{\partial t}\vec{W} = -\frac{\iint_{\partial V} \overline{\overline{F}} \cdot n dS}{\iiint_V dV} \tag{4.13}$$

and it can be rewritten as

$$\frac{\partial}{\partial t}\vec{W} = -\frac{1}{V} \cdot \vec{Q}^F \, . \tag{4.14}$$

Here, $\vec{Q}^F$ represents the fluxes over the boundaries of the control volume. If the boundary is divided into n faces, $\vec{Q}^F$ is given by

$$\vec{Q}^F = \sum_{i=1}^{n} \vec{Q_i}^F = \sum_{i=1}^{n} (\vec{Q}^{F,c} - D_i) \tag{4.15}$$

where $\vec{Q_i}^F$ denotes the inviscid fluxes over the respective faces and D_i represents dissipative flux. In order to determine the temporal evolution of flow properties within a control volume, it is crucial to compute the convective fluxes across its boundaries.

4.2.1 Concept of dual grid approach

A dual grid is created by taking the centroids of the elements (cells) in the original or primary grid and connecting them to form a new set of control volumes. Each cell in the dual grid is associated with a node in the primary grid. The primary and dual grids share the same points in physical space, however the dual grid consists of control volumes surrounding each grid point of the primary grid. The dual mesh defines these

control volumes in a way that aligns with the nodes of the primary mesh, improving the accuracy of flux calculations. Furthermore, the concept of dual mesh ensures that the control volumes are centered around the points where variables are stored. This alignment helps reduce numerical errors and provides better representation of gradients and fluxes, especially in complex geometries where unstructured meshes are used [87].
Consider points $P(j0)$ and $P(j1)$ separated by the face $F(i)$ (refer to Fig. 4.1). The convective fluxes across the face are determined by the flow conditions at points $P(j0)$ and $P(j1)$. These fluxes are regarded as exchanges between the control volumes enclosing points $P(j0)$ and $P(j1)$. The dimensions and direction of the face are characterized by the face normal vector. Consequently, the central fluxes across the face can be calculated as follows

$$\vec{Q}_F^{F,c} = \frac{1}{2}\left(\vec{F}_r(i) + \vec{F}_l(i)\right) - \frac{1}{2}\tilde{\alpha}(\vec{w}_r - \vec{w}_l) \tag{4.16}$$

where $\tilde{\alpha}$ describes the type of the dissipation, scalar or matrix dissipation. The difference $(\vec{w}_r - \vec{w}_l) = \vec{D}(j1)$ is computed as

$$\vec{D}(j1) = (\vec{w}_r - \vec{w}_l) = \epsilon_{(2)}(\vec{u}_r - \vec{u}_l) - \epsilon_{(4)}(L(\vec{u}_r) - L(\vec{u}_l)) \,. \tag{4.17}$$

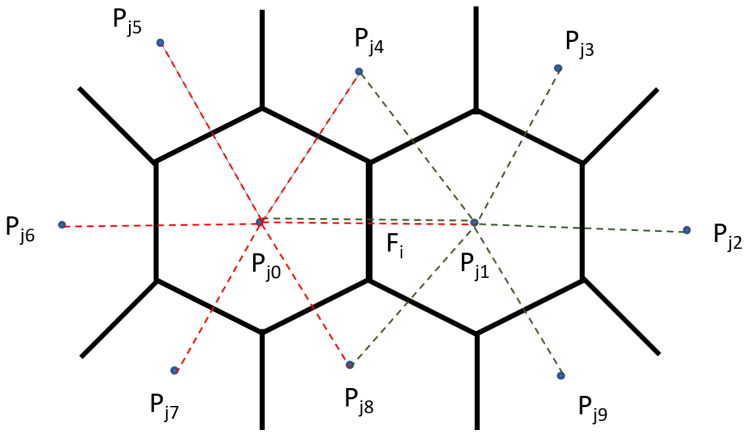

FIGURE 4.1: Illustration of the points needed for computing the flux over face F_i for a central scheme in dual control volumes

The vector $\vec{w}$ comprises the conservative variables ρ, ρu, ρv, ρw, and ρE. The subscripts l and r indicate variables on the left and right sides of the cell face respectively, while $\epsilon_{(2)}$ and $\epsilon_{(4)}$ act as coefficients controlling the magnitude of second and fourth-order dissipation introduced into the scheme. The Laplacian, denoted as $L(\vec{u}_i)$, is computed from adjacent

points as

$$L(\vec{u}_i) = \sum_{j=1}(\vec{u}_j - \vec{u}_i) \ . \tag{4.18}$$

For instance, in Fig. 4.1, the illustration depicts the points necessary for computing the flux across face F_i utilizing a central scheme, spanning from point P_{j0} to point P_{j9}. Notably, the impact of computing the Laplacian (utilizing fourth-order differences) is extensive. At point P_{j0}, the neighboring points include P_{j1}, P_{j4}, P_{j5}, P_{j6}, P_{j7}, and P_{j8}, interconnected by red dashed lines. Conversely, at point P_{j1}, the adjacent points consist of P_{j0}, P_{j8}, P_{j9}, P_{j2}, P_{j3}, and P_{j4}, linked by green dash-dot lines.

In the FVM formulation, the partial differential equations encompass various partial derivative terms that can be substituted with finite differences. This substitution leads to the formation of a difference equation, which serves as an algebraic expression representing the original partial differential equation. For illustration, considering the velocity u as constant and applying a forward difference scheme in time on the continuity equation, Eq. 3.1 takes the typical form of a linear convection equation discretized as

$$\frac{\rho_i^{n+1} - \rho_i^n}{\Delta t} = -\frac{u}{\Delta x}\left(\rho_{i+1/2}^n - \rho_{i-1/2}^n\right) \tag{4.19}$$

describing the transport of mass ρ by a flow of velocity u. In a first-order upwind scheme, the flux at $i + \frac{1}{2}$ and $i - \frac{1}{2}$ is determined based on the sign of the velocity u. For a positive velocity ($u > 0$), the fluxes at $i + \frac{1}{2}$ and $i - \frac{1}{2}$ can be approximated by ρ_i and ρ_{i-1}, respectively. The discretized equation then reads

$$\frac{\rho_i^{n+1} - \rho_i^n}{\Delta t} = -\frac{u}{\Delta x}\left(\rho_i^n - \rho_{i-1}^n\right) \tag{4.20}$$

Using a second order difference formula for the discretization of the spatial derivative of ρ at mesh point i and again a forward difference formula for the time derivative the discrete equation reads

$$\frac{\rho_i^{n+1} - \rho_i^n}{\Delta t} = -\frac{u}{2\Delta x}\left(\rho_{i+1}^n - \rho_{i-1}^n\right) \tag{4.21}$$

which is a second-order central scheme.

Unlike upwind schemes, which introduce numerical dissipation to stabilize solutions, central schemes utilize a centered stencil to approximate derivatives. They typically offer second-order accuracy and do not inherently introduce dissipation, making them advantageous for scenarios where maintaining solution accuracy is crucial.

While central schemes are less dissipative, they can exhibit non-physical oscillations near

discontinuities (such as shock waves) due to their non-dissipative nature. To stabilize the solution without excessively smearing out physical features, additional dissipation (artificial viscosity) needs to be selectively introduced. This dissipation needs to be computed for each grid point $P(i)$. The approach follows the strategy outlined by Mavriplis and Jameson [88] to determine an appropriate dissipation scaling for highly stretched cells.
The numerical dissipation associated with central schemes is crucial for maintaining both accuracy and stability in simulations involving discontinuities such as shock waves. As described in Eq. 4.17, the dissipation term is composed of two parts: the first part, denoted as $\epsilon_{(2)}$, is activated in the presence of strong discontinuities to prevent non-physical oscillations, while the second term, $\epsilon_{(4)}$, is conventionally included to enhance numerical stability in smooth flow regions. This distinction ensures that the scheme remains robust across different flow regimes, minimizing excessive dissipation in regions where the flow is continuous while still effectively handling shocks and other discontinuities. Thus, the numerical strategy employed strikes a balance between accuracy and stability, as evidenced by its formulation in Eq. 4.17.
Matrix dissipation method, proposed by Blazek [89], is used in this study, which introduces dissipation in a controlled manner. It involves computing the eigenvalues and eigenvectors of the flux Jacobian matrix, which are associated with the wave speeds and modes of the system. Dissipation is then incorporated based on these eigenvalues, ensuring alignment with the characteristic waves of the flow. This approach enables dissipation to act more efficiently and only where necessary, preserving the sharpness of shocks and interfaces.
When employing the matrix dissipation method with central schemes, the initial discretization is conducted using a central scheme, after which the matrix-based dissipation is added to stabilize the solution. The magnitude and direction of dissipation are determined by the local flow characteristics, as dictated by the Jacobian matrix of the system.

4.2.2 Solution approach for time-accurate computations

As the current study employs transient simulations, the solution approach for time-accurate computations is presented in this subsection. Consider $\left[0, T\right]$ represent the time interval, and $t_0 = 0 < t_1 < \cdots < t_n = T$ denote a partition of $\left[0, T\right]$. We examine the following time-dependent problem. The temporal evolution of the flow variables can be expressed in a general form for a point $P(j1)$ as

$$\frac{d}{dt}\vec{W}(j1) + \vec{R}(j1) = 0 \tag{4.22}$$

where

$$\vec{R}(j1) = \frac{1}{V(j1)} \cdot \vec{Q}^F(j1) \tag{4.23}$$

and the notation $\vec{R}(j1)$ indicates that the residual $\vec{R}$ for dual cell $j1$ was computed using the vector of conservative variables $\vec{W}$. In the first step, a backward difference formula (BDF) for discretizing the time derivative is employed. The TAU code provides BDF of the first, second, and third order accuracy. For example, the second-order accurate BDF reads

$$\frac{3}{2\Delta t}\vec{W}(j1)^{n+1} - \frac{4}{2\Delta t}\vec{W}(j1)^{n} + \frac{1}{2\Delta t}\vec{W}(j1)^{n-1} = -\vec{R}(\vec{W}^{n+1})(j1) \tag{4.24}$$

where $\vec{W}(j1)^{\nu}$ denotes the solution at time t_ν. We arrive at a sequence of (nonlinear) steady-state problems. For the iterative solution of an unsteady problem, one commonly used approach is Dual-Time stepping scheme, proposed by Jameson [90]. In this approach, the solution at each physical time step is obtained by treating it as a steady-state problem using an additional fictitious pseudo-time, t^*. Assuming that $\vec{W}(j1)^{n}$ and $\vec{W}(j1)^{n-1}$ have already been computed, we seek $\vec{W}(j1)^{n+1}$ by considering the following equation in fictitious pseudo time t^*,

$$\frac{d}{dt^*}\vec{W}(j1)^{n+1} = -\vec{R}^{DTS}(\vec{W}^{n+1})(j1) \tag{4.25}$$

with the modified residual

$$\vec{R}^{DTS}(\vec{W}^{\nu})(j1) = \vec{R}(\vec{W}^{\nu})(j1) + \frac{3}{2\Delta T}\vec{W}(j1)^{\nu} - \frac{4}{2\Delta T}\vec{W}(j1)^{n} + \frac{1}{2\Delta T}\vec{W}(j1)^{n-1} \tag{4.26}$$

This problem can be integrated using a K-stage Runge-Kutta scheme until a steady state in the fictitious pseudo-time τ is reached. The convergence of the solution in pseudo-time ensures that each physical time step has reached a steady-state solution before advancing to the next time step. Additionally, acceleration techniques for steady-state problems can be applied to speed up the convergence within each pseudo-time iteration.

4.3 Turbulence modelling

Most practical engineering scenarios and naturally occurring flows exhibit turbulence, underscoring the significance of turbulence modelling in understanding and analyzing these phenomena. Turbulence within a flow is marked by rapid mixing and is considered deterministic chaos. Its effects introduce randomly varying behaviours in the flow variables. Turbulence inherently possesses a three-dimensional and unsteady nature, characterized by a broad spectrum of scale motions. Consequently, the principal challenge

in numerically simulating (as well as measuring) turbulence arises from the vast range of scales that need to be accurately resolved. Turbulent fluid flow operates across a broad spectrum of time and length scales, demanding an extensive amount of data to comprehensively describe it [91]. While the precise physical characteristics of turbulence still need to be fully understood, it can be adequately modelled with a satisfactory level of accuracy in numerical simulations.
The most precise method for simulating turbulent flows is referred to as Direct Numerical Simulation (DNS), wherein the complete set of Navier–Stokes equations is directly solved through a finely discretized mesh. This approach captures all scales present in a given flow, ranging from the smallest to the largest eddies. However, due to its computational demands, DNS is prohibitively expensive, limiting its application to low Reynolds number flows over relatively simple geometries. The Kolmogorov scale η, defined by the theory of turbulence based on energy cascade, is represented by [92]

$$\eta = \left(\frac{\nu^3}{\epsilon}\right)^{\frac{1}{4}} . \tag{4.27}$$

In some cases, one is mainly interested in the steady-state fluid flow, and hence, it is optional to simulate the detailed instantaneous flow, leading to a significant reduction of computational time. It is the basis for the Reynolds-averaged Navier–Stokes (RANS) approach in which one solves only for the averaged quantities. At the same time, a turbulence model models the effect of all the scales of instantaneous turbulent motion. Due to its modest computing requirement, this approach has been the backbone of industrial CFD applications for the last few decades. Nevertheless, knowledge of the transient behaviour of the flow is necessary, and the RANS approach is therefore not sufficient in many cases, it fails to predict the flow behaviour, such as transition. By decomposing instantaneous variables using Reynolds decomposition, these equations yield time-averaged mean field and fluctuating field values. The solutions derived from these time-averaged Navier-Stokes equations elucidate mean flow characteristics incorporating turbulence effects.

4.3.1 Reynolds-averaged Navier-Stokes equations

Turbulence modelling involves the formulation of a set of partial differential equations to calculate turbulent flow, utilizing approximations of the precise Navier–Stokes equations. The Reynolds-averaged Navier–Stokes equations (RANS) begin with the Reynolds decomposition [93] of flow variables into mean and fluctuating components. Inserting these decomposed variables into the Navier–Stokes equations, followed by equation averaging,

leads to the emergence of the Reynolds-stress tensor. This tensor represents an unknown term that necessitates modelling for the successful solution of the RANS equations. The challenge in closing the system of Navier–Stokes equations essentially revolves around addressing this operation. Following Reynolds decomposition, any arbitrary field ϕ could be decomposed as follows [94]

$$\phi(x_i, t) = \overline{\phi(x_i)} + \phi^{'}(x_i, t) \tag{4.28}$$

where $\phi(x_i, t)$ is the instantaneous field, $\overline{\phi}$ is the time-averaged mean field and $\phi^{'}(x_i, t)$ is the fluctuating field. The term $\overline{\phi(x_i, t)}$ is defined as

$$\overline{\phi(x_i)} = \lim_{T \to \infty} \frac{1}{T} \int_t^{t+T} \phi(x_i, t) dt \ . \tag{4.29}$$

By time-averaging the equations governing mass, momentum, and energy, we derive the Reynolds-Averaged Navier-Stokes (RANS) equations. For incompressible turbulent flows, the continuity equation remains unchanged as it is linear concerning velocity. However, additional terms emerge in the momentum and energy equations due to the non-linearity inherent in the convection term. Assuming incompressible flow with constant viscosity, the momentum equation after time-averaging adopts the following expression

$$\frac{\partial \rho u_i}{\partial t} + \frac{\partial \rho u_i u_j}{\partial x_j} = -\frac{\partial p}{\partial x_i} + \mu \frac{\partial^2 u_i}{\partial x_j \partial x_j} + \frac{\partial}{\partial x_j}(\tau_{ij}^R) \tag{4.30}$$

where the mean value notation (overbar) has been omitted for clarity. A comparable outcome is achieved for the energy equation (Eq. 3.3). The additional components in Eq. 4.30 are referred to as the Reynolds Stresses, denoted as τ_{ij}^R in tensor notation. They are defined as $-\rho\overline{u_i' u_j'}$ and account for the influence of turbulent motions on average stresses. The Reynolds-stress tensor displays symmetry, where the diagonal components represent normal stresses, and the off-diagonal components represent shear stresses. The RANS equations system is not a closed system for calculating the dependent variables due to the Reynolds-stress tensor introducing six additional independent unknowns. Addressing the closure of the Reynolds-averaged Navier–Stokes equations involves primarily expressing the Reynolds-stress tensor as a function of mean-field and other variables through models. Experimental evidence showed that turbulence decays unless there is shear in isothermal incompressible flows [86]. Furthermore, turbulent stresses are found to increase as the mean rate of deformation increases. Boussinesq [95] proposed that Reynolds stresses

might be proportional to mean deformation rates as follows

$$\tau_{ij}^R = -\rho\overline{u_i' u_j'} = \mu_t \left[\left(\frac{\partial u_i}{\partial x_j} + \frac{\partial u_j}{\partial x_i} \right) - \frac{2}{3}\delta_{ij}\frac{\partial u_k}{\partial x_k} \right] - \frac{2}{3}\rho k \delta_{ij} \tag{4.31}$$

where k denotes the turbulent kinetic energy of the fluctuations, defined as

$$k = \frac{1}{2}(\overline{u_i' u_i'}) \, . \tag{4.32}$$

The first term of the right-hand side of Eq. 4.31 is analgous to Eq. 3.8 except for the appearance of the turbulent eddy viscosity μ_t. The second term on Eq. 4.31 ensures that the formula gives the correct result for the normal Reynolds stresses.
On dimensional grounds, kinematic turbulent viscosity, which has dimensions m^2/s, can be expressed as a product of a turbulent velocity scale θ_t (m/s) and a turbulent length scale l_t (m). If one velocity scale and one length scale suffice to describe the effects of turbulence, dimensional analysis yields

$$\nu_t = C\theta_t l_t \, . \tag{4.33}$$

Favre-averaging for compressible flows When addressing compressible flows, it is essential to consider not only fluctuations in velocity and pressure but also variations in density and temperature. When the governing equations are utilized with density expressed as the aggregate of its time-average and fluctuating components, the Reynolds averaging process generates supplementary terms involving correlations with fluctuating density ρ', thereby demanding more intricate turbulence closure models. For example, by time averaging the continuity equation and using the Reynolds averaging rules, the Reynolds-averaged continuity equation for compressible flows is as follows.

$$\frac{\partial \overline{\rho}}{\partial t} + \frac{\partial}{\partial x_i}(\overline{\rho u_i} + \overline{\rho' u_i'}) = 0 \tag{4.34}$$

To achieve closure, it is necessary to approximate the correlation between the fluctuating quantities $(\overline{\rho' u_i'})$ in some manner. The complexity increases for the momentum and energy equations, as they involve triple correlations that encompass density fluctuations. Therefore, to overcome this issue, the density-weighted averaging procedure proposed by Favre [96] is employed. The mass average for a velocity component $\widetilde{u_i}$, is defined as

$$\widetilde{u_i} = \frac{1}{\overline{\rho}} \lim_{T\to\infty} \frac{1}{T} \int_t^{t+T} \rho(\vec{x}, t) \; u_i(\vec{x}, t) dt = \frac{\overline{\rho u_i}}{\overline{\rho}} \tag{4.35}$$

$$\overline{\rho}\widetilde{u}_i = \overline{\rho u_i} \tag{4.36}$$

Using Reynolds decomposition and Reynolds averaging rules on RHS of Eq. 4.36 and substituting in Eq. 4.34 results as

$$\frac{\partial \overline{\rho}}{\partial t} + \frac{\partial}{\partial x_i}(\overline{\rho}\widetilde{u}_i) = 0 \tag{4.37}$$

which is the Favre-averaged compressible continuity equation. Similar to Reynolds averaging, the Favre-averaging technique breaks down the instantaneous flow variables into mass-averaged and fluctuating elements. This approach bears resemblance to Reynolds averaging in that it enables the decomposition of instantaneous flow variables into mass-averaged $\widetilde{\phi}_i$ and ϕ_i'' as $\phi_i = \widetilde{\phi}_i + \phi_i''$, where it is then multiplied by the density and time-averaged to form the Favre-averaged decomposition.
The Favre average of a fluctuating variable is zero, resulting in the time average of the density correlation being equivalent to the time-averaged density multiplied by the mass average of the variable,

$$\overline{\rho}\widetilde{\phi}_i = \overline{\rho\phi_i} \tag{4.38}$$

Similarly applying Favre averaging to the momentum and energy equations yields

$$\frac{\partial \overline{\rho}\widetilde{u}_i}{\partial t} + \frac{\partial \overline{\rho}\widetilde{u}_i\widetilde{u}_j}{\partial x_j} = -\frac{\partial \overline{p}}{\partial x_i} + \frac{\partial}{\partial x_j}\left(\overline{\tau_{ij}} + \tau_{ij}^R\right) \tag{4.39}$$

$$\frac{\partial \overline{\rho}\widetilde{E}}{\partial t} + \frac{\partial \overline{\rho}\widetilde{u}_i\widetilde{E}}{\partial x_j} = -\frac{\partial \overline{p}\widetilde{u}_i}{\partial x_i} + \frac{\partial}{\partial x_j}\Big(\left(\overline{\tau_{ij}} + \tau_{ij}^R\right)\widetilde{u}_i - \left(q_i + q_i^R\right)\Big) \tag{4.40}$$

These Favre-averaged equations share similarities with the incompressible RANS equations but incorporate the Reynolds stress tensor, which is defined as

$$\tau_{ij}^R = -\overline{\rho u_i'' u_j''} \tag{4.41}$$

While Favre averaging exhibits similarities to RANS equations, it does not entirely eradicate the influence of density fluctuations on turbulence within the flow. Despite being derived from compressible flow equations, Favre-averaged equations can often be reformulated to resemble the incompressible flow equations for the sake of simplicity and practical application. This transformation into an incompressible-like form proves beneficial for practical use and enables the utilization of established turbulence models developed for incompressible flows.

SA turbulence model

The Spalart-Allmaras model [97] involves one transport equation for kinematic eddy viscosity parameter $\widetilde{\nu}$ and a specification of a length scale using an algebraic formula and provides economic computations of boundary layers in external aerodynamics. The turbulent viscosity is related to $\tilde{\nu}$ by

$$\nu_t = \widetilde{\nu} \cdot f_{\nu 1} \tag{4.42}$$

where

$$f_{\nu 1} = \frac{\chi^3}{\chi^3 + c_{\nu 1}^3} \tag{4.43}$$

is a damping function, depending on the turbulence Reynolds number represented by the viscosity ratio

$$\chi = \frac{\widetilde{\nu}}{\nu} \tag{4.44}$$

with ν the average kinematic viscosity of the fluid, and $c_{\nu 1} = 7.1$.
The transport equation for $\widetilde{\nu}$ is as follows

$$\frac{\partial(\rho\widetilde{\nu})}{\partial t} + \frac{\partial(\rho\tilde{\nu}u_i)}{\partial x_i} = \rho P_{\widetilde{\nu}} - \rho D_{\widetilde{\nu}} - \rho\Phi_{\widetilde{\nu}} + \rho C_{\widetilde{\nu}} + \rho T_{\widetilde{\nu}} \tag{4.45}$$

where $\rho P_{\widetilde{\nu}}$ represents production, $\rho D_{\widetilde{\nu}}$ represents diffusion and $\rho\Phi_{\widetilde{\nu}}$ represents destruction. The terms $\rho D_{\widetilde{\nu}}$ and $\rho T_{\widetilde{\nu}}$ are modifications for compressibility and turbulence onset. Production, destruction and diffusion are defined as

$$\rho P_{\widetilde{\nu}} = c_{b1}(1 - f_{t2})\widetilde{S}\rho\widetilde{\nu} \tag{4.46}$$

$$\rho\Phi_{\widetilde{\nu}} = \left(c_{w1} f_w - \frac{c_{b1}}{\kappa^2} f_{t2}\right)\rho\left[\frac{\widetilde{\nu}}{d}\right]^2 \tag{4.47}$$

$$\rho D_{\widetilde{\nu}} = \frac{1}{\sigma}\left(\frac{\partial}{\partial x_k}\left[\rho(\nu + \widetilde{\nu})\frac{\partial\widetilde{\nu}}{\partial x_k}\right] + c_{b2}\rho\frac{\partial\widetilde{\nu}}{\partial x_k}\frac{\partial\widetilde{\nu}}{\partial x_k}\right) \tag{4.48}$$

respectively, where the model coefficients take the following values

$$c_{b1} = 0.1355, \quad c_{b2} = 0.622, \quad \sigma = 2/3, \quad \kappa = 0.41, \quad c_{w1} = \frac{c_{b1}}{\kappa^2} + \frac{1 + c_{b2}}{\sigma}\,. \tag{4.49}$$

Furthermore, d is the distance to the closest wall. In the production term, $\widetilde{S}$ is a scalar measure of the velocity gradient, defined as

$$\widetilde{S} = S + \frac{\widetilde{\nu}}{\kappa^2 d^2} f_{\nu 2} \tag{4.50}$$

where

$$S = |\vec{\omega}| \tag{4.51}$$

is the absolute value of the vorticity and

$$f_{\nu 2} = 1 - \frac{\chi}{1 + \chi f_{\nu 1}} \tag{4.52}$$

ensures that $\widetilde{\nu}$ varies linearly down to the wall. In the destruction term,

$$f_w = g\Big[\frac{1 + c_{w3}^6}{g^6 + c_{w3}^6}\Big]^{1/6} \tag{4.53}$$

with

$$g = r + c_{w2}(r^6 - r) \tag{4.54}$$

controls the decay of $\widetilde{\nu}$ towards the boundary layer edge. The coefficient values are

$$c_{w2} = 0.3, \quad c_{w3} = 2\,. \tag{4.55}$$

Finally, the term

$$f_{t2} = c_{t3} \exp(-c_{t4}\chi^4) \tag{4.56}$$

appearing in production and destruction has been designed to suppress turbulence in laminar regions. Its coefficient values are

$$c_{t3} = 1.2 \quad \text{and} \quad c_{t4} = 0.5\,. \tag{4.57}$$

and the compressibility term is

$$\rho C_{\widetilde{\nu}} = -\frac{1}{\sigma}(\nu + \widetilde{\nu}) \frac{\partial \rho}{\partial x_k} \frac{\partial \widetilde{\nu}}{\partial x_k} \tag{4.58}$$

SA-neg turbulence model In general, the solution of $\widetilde{\nu}$ must always be positive, but in numerical simulations, negative values may occur due to the respective solution algorithm. The negative SA model (SA-neg) has been advised by Allmaras et al. [98] in order to cope

with the negative values of $\widetilde{\nu}$ without degrading the numerics. In regions with negative $\widetilde{\nu}$, the definition of the production term, the destruction term and the diffusion term is

$$\rho P_{\widetilde{\nu}} = c_{b1}(1 - c_{t3}) S \rho \widetilde{\nu} \,, \tag{4.59}$$

$$\rho \Phi_{\widetilde{\nu}} = -c_{w1} \rho \Big[\frac{\widetilde{\nu}}{d}\Big]^2 \,, \tag{4.60}$$

$$\rho D_{\widetilde{\nu}} = \frac{1}{\sigma}\Big(\frac{\partial}{\partial x_k}\big[\rho(\nu + f_n \widetilde{\nu})\frac{\partial \widetilde{\nu}}{\partial x_k}\big] \tag{4.61}$$

where

$$f_n = \frac{c_{n1} + \chi^3}{c_{n1} - \chi^3} \tag{4.62}$$

with $c_{n1} = 16$ modifying the diffusion coefficient.

k - ω turbulence model

This model employs transport equations for the specific kinetic turbulence energy k and the specific dissipation rate ω that can be cast into the following general form [99]:

$$\frac{\partial(\rho k)}{\partial t} + \frac{\partial(\rho k u_j)}{\partial x_j} = \rho P_k - \rho \epsilon + D_k \tag{4.63}$$

with the turbulence production term P_k

$$P_k = \tau_{ij}^R \frac{\partial u_i}{\partial x_j} \tag{4.64}$$

the dissipation term

$$\rho \epsilon = \beta^k \rho \omega k \tag{4.65}$$

and the diffusion term

$$\rho D_k = \frac{\partial}{\partial x_j}\left[(\mu + \sigma_k \mu_t)\frac{\partial k}{\partial x_j}\right] \tag{4.66}$$

The transport equation for the specific dissipation rate is [99]

$$\frac{\partial(\rho \omega)}{\partial t} + \frac{\partial(\rho \omega u_j)}{\partial x_j} = \rho P_\omega - \rho \Phi_\omega + \rho C_{D_\omega} + \rho D_\omega \tag{4.67}$$

with the production term

$$\rho P_\omega = \gamma_\omega S_{c_\omega} \rho P_k \tag{4.68}$$

the dissipation term

$$\rho\Phi_\omega = \beta_\omega \rho \omega^2 \tag{4.69}$$

the cross-diffusion term

$$\rho C_{D_\omega} = \sigma_d \frac{\rho}{\omega} \frac{\partial k}{\partial x_k} \frac{\partial \omega}{\partial x_k} \tag{4.70}$$

and the diffusion term

$$\rho D^\omega = \frac{\partial}{\partial x_j} \left[(\mu + \sigma_{\omega 1} \mu_t) \frac{\partial \omega}{\partial x_j} \right] \tag{4.71}$$

In these equations, β_k, β_ω, γ_ω, σ_k, σ_ω and σ_d are closure coefficients that vary between the different models. Furthermore, S_{c_ω} denotes a scaling factor that for most, but not all, models is given by ω/k.
In the original Wilcox 1988 model, the closure coefficients are given by Wilcox [99] as $\beta_k = 0.09$, $\beta_\omega = 0.075$, $\gamma_\omega = \frac{5}{9}$, $\sigma_k = 0.5$, $\sigma_\omega = 0.5$ and $\sigma_d = 0$ and eddy viscosity is defined by

$$\mu_t = \frac{\rho k}{\omega} \tag{4.72}$$

and scaling the ω-production term by

$$S_{c_\omega} = \frac{\omega}{k} \tag{4.73}$$

Menter Baseline model In order to overcome the free-stream sensitivity of the Wilcox 1988 model, Menter [100, 101] suggests to combine the $k-\omega$ model near walls with the standard $k-\epsilon$ model in the free stream. Transforming the corresponding ϵ-equation into a transport equation for ω leads to the appearance of the cross-diffusion term C_{D_ω}, which is responsible for suppressing the free-stream sensitivity. While the $k-\omega$ model provides better accuracy in near-wall regions, the $k-\epsilon$ model performs better in regions outside these near-wall regions. Menter [100, 101] achieves the combination of $k-\omega$ and $k-\epsilon$ transport equations by a smooth change of the closure-coefficients values according to

$$\phi = F_1 \phi_i + (1 - F_1)\phi_o \tag{4.74}$$

where $\phi = \beta_k, \beta_\omega, \gamma_\omega, \sigma_k, \sigma_\omega$ and σ_d and the indices i and o represent values near the wall (inner part, i) and in the free stream (outer part, o), respectively. The blending function is defined as

$$F_1 = \tanh(G_1^4) \tag{4.75}$$

where

$$G_1 = \min[\max(\Gamma_1, \Gamma_2), \Gamma_3] \tag{4.76}$$

with the arguments

$$\Gamma_1 = \frac{\sqrt{k}}{0.09\ \omega\ d} \quad \Gamma_2 = \frac{500\mu}{\rho\omega\ d^2} \quad \text{and} \quad \Gamma_3 = \frac{2\sigma_d \rho k}{\rho C_{D_\omega} d^2} \tag{4.77}$$

The bounding values of the closure coefficients are given by Wilcox [99] as $\beta_k = 0.09$, $\beta_\omega = 0.075$, $\gamma_\omega = \frac{5}{9}$, $\sigma_k = 0.5$, $\sigma_\omega = 0.5$ and $\sigma_d = 0$ for the near-wall coefficients and $\beta_k = 0.09$, $\beta_\omega = 0.075$, $\gamma_\omega = \frac{5}{9}$, $\sigma_k = 0.5$, $\sigma_\omega = 0.5$ and $\sigma_d = 0$ for free-stream coefficients.

Menter shear stress transport (SST) model Together with the Baseline model, Menter [100, 101] published the so-called Shear Stress Transport (SST) model. It is an extension of the BSL model, improving its sensitivity to positive pressure gradients (separation). It is achieved by limiting the eddy viscosity according to

$$\mu_t = \frac{\rho a_1 k}{\max(a_1\omega, \Omega F_2)} = \frac{\rho k}{\omega} \frac{1}{\max(a_1\omega, \Omega F_2)} \tag{4.78}$$

where $a_1 = 0.31$ and

$$F_2 = \tanh(G_2^2) \tag{4.79}$$

with

$$G_2 = \max(2\Gamma_1, \Gamma_2) \tag{4.80}$$

is another blending function that takes on a value of $F_2 = 1$ near walls and switches to a value of $F_2 = 0$ at the boundary layer edge, thus restricting the eddy-viscosity limitation (SST limitation) to boundary layers. The arguments Γ_1 and Γ_2 are identical to the ones used with the F1 function of the BSL model.

4.3.2 Scale-resolving turbulence approach

Scale-resolving approach in CFD is aimed at capturing intricate flow features across a wide range of scales. Unlike traditional Reynolds-Averaged Navier-Stokes (RANS) methods that rely on turbulence modeling to resolve turbulent fluctuations, scale-resolving approach endeavors to directly simulate a significant portion of the turbulent spectrum. By resolving smaller turbulent structures, the approach offers the potential to provide more accurate predictions, particularly in regions where flow dynamics are dominated by turbulence.

Large-Eddy Simulation (LES)

Smagorinsky [102] initially proposed Large-Eddy Simulation (LES) in 1963 for atmospheric flow prediction, with early applications focused on this domain. Its application to engineering-related flows began in 1970 by Deardoff [103] and in 1975 by Schumann [104]. Initially progressing slowly until the mid-1980s, primarily applied to simple flows like homogeneous turbulence and mixing layers, the rapid development of LES accelerated with increased computing power. Particularly after the 1990s, the LES community witnessed significant growth, expanding applications from simple to complex flows, including multi-phase flow, heat transfer, combustion, aeroacoustics, etc. [105]. This surge in LES development and applications is attributed to increased computing power and the realization that RANS methods inherently struggle with certain classes of complex turbulent flow problems.
LES computes large-scale turbulent flow motions directly, modelling only the smaller scale (sub-grid scale) motions. This results in a significant reduction in computational cost compared to DNS. LES surpasses the accuracy of RANS as it directly captures the large, detailed eddies responsible for most of the turbulent energy, momentum transfer, and mixing. Unlike RANS, LES finds modelling small scales easier due to their greater isotropy and homogeneity than large scales.
In LES, explicit filtering is applied to the instantaneous conservation equations, formulating 3D unsteady governing equations for large-scale motions. When using the finite volume method to solve the instantaneous governing equations numerically, implicit filtering occurs during the integration over control volumes. However, implicit filtering has a potential shortcoming, as truly mesh-independent results become challenging. With mesh refinement, smaller-scale motions are resolved, and continuous refinement eventually leads to DNS rather than LES. It introduces difficulty in distinguishing between numerical and modelling errors, hindering useful analysis of numerical schemes [105].

Detached-Eddy simulation (DES)

In spite of the potential advantages offered by LES, challenges persist in accurately capturing turbulent stresses near walls due to the significant computational resources needed, which approach those required for DNS. Another alternative that has gained popularity over the years involves hybrids of LES and RANS, such as Detached-Eddy Simulation (DES). The fundamental concept of DES was initially proposed by Spalart et al. [66]. This approach combines elements of RANS and LES by employing RANS to model near-wall and boundary layer regions while employing LES outside these areas. DES is named after

this concept. Spalart et al. [66] adapted the SA model to achieve an equivalent of DES. The sole adjustment lies in the dissipation term of the transport equation for $\widetilde{\nu}$

$$- c_w f_{w1} \frac{\widetilde{\nu}}{\widetilde{d}} . \tag{4.81}$$

In the original one-equation Spalart-Allmaras turbulence model [97], the terms d and $\widetilde{d}$, denoting the distance to the wall, were identical

$$\widetilde{d} = d = \text{distance of the nearest wall} . \tag{4.82}$$

However, in the DES formulation of the Spalart-Allmaras model, these terms differ, with $\widetilde{d}$ defined as

$$\widetilde{d} = C_{DES}\Delta \tag{4.83}$$

where C_{DES} is a constant and Δ represents the grid size metric. Practically, in the DES formulation of the one-equation SA model, the distance to the wall is expressed by comparing the actual distance to the wall with $C_{DES}\Delta$, which essentially evaluates the maximum cell length

$$\widetilde{d} = \min(d, C_{DES}\Delta) \quad \text{with } \Delta = \max(\Delta_x, \Delta_y, \Delta_z) . \tag{4.84}$$

When the cell length ($C_{DES}\Delta$) is smaller than the actual distance to the nearest wall (d), LES is activated. Conversely, RANS is triggered when the opposite condition holds. Therefore, the boundary between LES and RANS depends entirely on the geometry and computational mesh density. It is noteworthy that alternative metric relations are also feasible. The primary challenge facing such hybrid RANS/LES methods is the scale disparity between the LES and RANS regions, unlike wall-layer modelling techniques, where the scales of the outer layer dictate those of the inner layer, resulting in the presence of eddies as small as the filter size in the inner layer. Hybrid methods introduce their own time and length scales in the inner layer, determined by the unsteady RANS equations applied there, and these scales are generally much more significant than those of the outer-layer eddies [106].

A notable drawback of the original DES method arises when grids are locally refined in multiple directions in regions not designated for scale resolution, commonly seen in highly curved geometric areas or near converging solid surfaces. The DES transition criterion, as expressed in Eq. 4.84, directly compares the RANS length scale with the maximum grid cell dimension. This can lead to a significant decrease in eddy viscosity within the boundary

layer without a mechanism to convert modeled turbulence energy into resolved energy. In scenarios where the boundary layer's wall-parallel grid spacing exceeds boundary layer thickness (δ), Eq. 4.84 ensures DES operates in RANS mode throughout the boundary layer. However, it may inadvertently trigger LES mode in areas with ambiguous grid definitions, particularly where $\Delta \ll \delta$, potentially lacking the necessary refinement to support resolved turbulence. To remedy this issue, the initial enhancement leading to Delayed Detached Eddy Simulation (DDES), as introduced by P. R. Spalart et al. [107], addresses the issue of preventing premature transition from RANS to LES mode within attached boundary layers solely due to grid design. This is achieved by adjusting the DES length scale with a flow-dependent delaying function, ensuring persistence of RANS mode in attached boundary layer regions. DDES aims for accurate simulations in complex geometries, maintaining RANS mode throughout the boundary layer to avoid early LES transitions from sub-optimal grids. In DDES, the hybrid length scale $\tilde{d}_{\text{DDES}}$ is expressed as

$$\tilde{d}_{\text{DDES}} = d - f_d \max\left(0, d - C_{DES}\Delta\right) \tag{4.85}$$

where the delaying function f_d is defined by

$$f_d = 1 - \tanh([8r_d]^3) \tag{4.86}$$

with

$$r_d = \frac{\mu + \mu_t}{\rho\kappa^2 d^2 \sqrt{\frac{\partial u_i}{\partial x_j}\frac{\partial u_i}{\partial x_j}}} \,. \tag{4.87}$$

The variable r_d approximates unity within the boundary layer's sub-layer and logarithmic regions, decreasing towards zero near the boundary, causing f_d to remain low until encountering the defect layer, where it rises rapidly towards unity as r_d diminishes. Setting f_d to 0 yields RANS ($\tilde{d} = d$), while setting it to 1 gives original DES version ($\tilde{d} = \min(d, C_{DES})$). However, as highlighted by Spalart et al. [107], when DDES approach is employed as a wall model in LES, it offers no advantages over original DES model. Further work in this regard led to the development of IDDES approach which entails two branches, namely DDES and wall-modelled LES (WM-LES). DDES branch is responsible for DDES-like functionality in IDDES, activating only under inflow conditions lacking turbulent content. WM-LES branch is designed to activate solely under unsteady inflow conditions that introduce turbulent content and when the grid resolution is sufficient to resolve dominant boundary-layer eddies. It introduces a novel seamless hybrid RANS-LES model, integrating RANS and LES methodologies by introducing the following blended RANS-LES length-scale

$$l_{WMLES} = f_B(1 + f_e)l_{RANS} + (1 - f_B)l_{LES} \tag{4.88}$$

where, similarly to DDES, l_{RANS} and l_{LES} are the RANS and LES length scales, respectively. The empirical blending function f_e is defined as

$$f_e = \min\{2\exp(-9\alpha^2), 1.0\}, \quad \alpha = 0.25 - d_w/h_{max} \tag{4.89}$$

It varies from 0 to 1, providing rapid switching of the model from RANS mode ($f_B = 1.0$) to LES mode ($f_B = 0$) within the range of wall-distance $0.5h_{\max} < d_w < h_{\max}$. The elevating function f_e is aimed at to prevent the excessive reduction of RANS Reynolds stresses observed in the interaction between RANS and LES regions near their interface. This feature plays a crucial role in addressing log-layer mismatch.

Scale-Adaptive simulation (SAS)

Although all RANS models have the potential to be solved in an unsteady manner (URANS), conventional URANS models are known to lack spectral content, even when the grid and time step resolutions are adequate. This limitation has been attributed to high turbulent viscosities that reflect the averaging in the theoretical derivation of the RANS equations, which effectively removes all turbulence information from the velocity field. The SAS model can be considered as a URANS model with a scale-resolving capability, which can show LES-like behaviour. Unlike LES, it also remains well-defined if the mesh cells become coarser. This makes it attractive in the present application, where the aero-acoustic effects are mostly affected by larger turbulent scales, which, in turn, need to be predicted accurately.

The work by Menter et al. [38] suggests a modified turbulence model that adds a source term Q_{SAS} based on the local von Karman length scale L_{vK} into the dissipation rate transport equation to only resolve turbulence where significant fluctuations exist and can be resolved by the mesh. This scale-resolving technique with the standard k-ω SST model [100] as the base model has been used in the present study. The source term Q_{SAS} is added in the transport equation for the turbulence eddy frequency ω which is defined in Einstein's notations, as shown in Eq. 4.90.

$$Q_{SAS} = max\left[\rho\zeta_2 S^2\left(\frac{L^m}{L_{vK}}\right)^2 - F_{SAS}\frac{2\rho k}{\sigma_\phi}max\left(\frac{1}{k^2}\frac{\partial k}{\partial x_j}\frac{\partial k}{\partial x_j}, \frac{1}{\omega^2}\frac{\partial \omega}{\partial x_j}\frac{\partial \omega}{\partial x_j}\right), 0\right] \tag{4.90}$$

with $\zeta_2 = 1.755$, $\sigma_\phi = 2/3$ and $F_{SAS} = 1.25$ and

$$L_{vK} = \kappa \frac{U'}{U''}, \quad L^m = c_\mu^{-1/4} \frac{\sqrt{k}}{\omega}, \quad U'' = \sqrt{\frac{\partial^2 u_i}{\partial x_k^2} \frac{\partial^2 u_i}{\partial x_j^2}}, \quad U' = \sqrt{2 \cdot S_{ij} S_{ij}} \tag{4.91}$$

with $c_\mu = 0.09$ and $\kappa = 0.41$.

Artificial Forcing In principle, the SAS approach thrives under significant flow fluctuations. Wall functions tend to damp the fluctuations close to the wall, and this results in the inability of the model to produce enough fluctuations; eventually, the SAS model becomes dormant when wall functions are used, resulting in a URANS solution with fully modelled turbulence. Therefore, to increase the resolution capability of the SAS model in the shear layer, an investigation has been carried out to force fluctuations inside the cavity based on the modelled length and time scales and activate the SAS model strongly in the shear layer of the cavity. It is achieved in the SAS-F simulation through the use of additional terms (Eq. 4.92) to transfer modelled kinetic energy into resolved turbulent kinetic energy as discussed in the original paper by Menter et al. [38]. The terms $F_{mom,i}$ are added to the momentum equations, whereas F_k is subtracted from the turbulent kinetic energy equation. The fluctuating term $u_{f,i}$ in Eq. 4.92, which requires as input the local length scale L_t and time scale τ_t computed from the underlying RANS turbulence model, is based on the random flow generator (RFG) by Kraichnan [108].

$$F_{mom,i} = \frac{\rho u_{f,i}}{\Delta t} \quad \text{and} \quad F_k = -0.5 \frac{\rho u_{f,i}^2}{\Delta t} \tag{4.92}$$

where

$$u_{f,i} = \sqrt{\frac{2}{3}k} \sqrt{\frac{2}{N}} \sum_{n=1}^{N} \left[p_i^n \cdot cos(arg^n) + q_i^n \cdot sin(arg^n) \right] \tag{4.93}$$

$$p_i^n = \epsilon_{ijk} \eta_j^n d_k^n; \quad q_i^n = \epsilon_{ijk} \xi_j^n d_k^n \tag{4.94}$$

$$arg^n = 2\pi \left(\frac{d_i^n x_i}{L_t} + \frac{\omega^n t}{\tau_t} \right) \tag{4.95}$$

where $L_t = C_L \frac{\sqrt{k}}{C_\mu \omega}$ ($C_L = 0.5$) is the length scale of the turbulence, and $\tau_t = \frac{L_t}{\sqrt{k}}$ is the time scale.

$$\eta_i^n = N(0,1), \quad \xi_i^n = N(0,1), \quad d_i^n = N(0,0.5), \quad \omega^n = N(1,1) \tag{4.96}$$

$N(\phi, \psi)$ is a random variable following a normal distribution with a mean ϕ and standard deviation ψ. Moreover, finer-scale structures that the grid could not resolve are prevented with the help of a Nyquist limiter. As a result, only the energy that the underlying grid can resolve is transferred. Thus, dissipation is shifted from the integral scales in the RANS mode of the SAS model toward subgrid scales in the scale-resolving mode.

$$\frac{\tau_t}{\omega^n} \geq 2\ \Delta t; \quad \frac{L_t}{|d^n|} \geq 2\ \Delta h \tag{4.97}$$

where Δt is the time step size, and Δh is the maximum of grid spacing in the x_1, x_2, x_3 directions. The forcing can be applied to the whole domain (globally) or to a specific region (zonally). In the global prescription of forcing, the SAS model damps out the fluctuations in the steady regions. The zonal prescription of forcing does not require additional treatment at the interfaces. Furthermore, the forcing term is only significant in the first few timesteps of the simulation, and its contribution to the momentum equation drops to a negligible value with time as the field contains more resolved structures and an equilibrium between forcing and dissipation develops. As a result, the stability and robustness of the method are similar to the unforced approach.

4.3.3 Wall treatment

In engineering applications, one of the main concerns is to predict the flow phenomena adjacent to the wall since the phenomena of production and destruction of turbulent energy are complex near the wall region. The wall shear stress in the momentum equation involves strong velocity gradients, and the contribution of effective viscous flux is predominantly high in the near-wall region. The exact computation of the effective viscosity field is imperative to compute the correct wall shear stress. There are two different approaches to predicting near-wall flows. One approach is to refine the region using smaller cells and integrate the low Reynolds number turbulence model equations to the wall. In the FVM method, the integration over the control volume is performed for each cell close to the wall in case of low Reynolds turbulence model equations. However, the computational effort is immensely higher with this approach. Another approach is to employ high Reynolds number turbulence model equations and use the wall functions to connect the wall and the first cell adjacent to the wall. The wall functions provide algebraic relations based on the law of wall concept to set the values for the dependent variables in the near-wall cell. A hybrid wall function aims to provide a boundary condition at solid walls that enables flow solutions independent of the location of the first grid node above the wall. The two

classical wall boundary conditions in the TAU code are low-Re and high-Re type boundary conditions. The low-Re boundary conditions impose no slip at the wall and require a low Re grid with $y^+ < 1$. The hybrid-Re boundary condition is an improved high-Re boundary condition, prescribing the wall-shear stress and no-penetration at the wall. The RANS equations are solved only down to the first grid node above the wall and are matched with an adaptive wall function solution at the first grid node above the wall.
Due to the matching condition at each first node above the wall that the wall-parallel components of the RANS solution u_{RANS} and the wall-function u_{WF} are equal at wall distance y_δ and from universal wall law $u_{WF}(y) = u_\tau F(\frac{y u_\tau}{\nu})$, we obtain

$$F\left(\frac{y_\delta u_\tau}{\nu}\right) = \frac{u_{RANS}(y_\delta)}{u_\tau} \tag{4.98}$$

which can be solved for u_τ using Newton's method and then τ_w is computed from ρu_τ^2.
In the TAU software [40], the following wall function is employed for the $k-\omega$ SST model, which is used in this work for wall function based simulation methods.

$$F_{k\omega,a} = (1-\phi_{k\omega})F_{Sp,3} + \phi_{k\omega}F_{Rei,m}\ , \quad \phi_{k\omega} = tanh(arg)\ , \quad arg = \left(\frac{y^+}{50}\right)^2 \tag{4.99}$$

where $F_{Sp,3}$ and $F_{Rei,m}$ represent Spalart's wall law [97] and Reichardt's wall law [109], respectively, with $\phi_{k\omega}$ serving as a blending function that helps transition smoothly between the wall laws depending on the flow conditions.

Chapter 5

Simulation configurations

This chapter introduces two simulation configurations simulated in this study, namely the open-cavity and hybrid delta-wing configurations. Section 5.1 provides details on the open-cavity geometry and is followed by a description of the meshing strategy employed for different simulation approaches. Section 5.2 presents the geometric characteristics of the hybrid delta-wing planforms and their meshing strategy. The simulation setup, including the boundary and initial conditions, is outlined for both configurations in their respective sections.

5.1 Cavity Flow

In this section, the open-cavity configuration with doors is introduced. Following that, the meshing strategy utilized in the work is explained, accompanied by some supporting plots, such as turbulent spectra and spectral analysis of different meshes. The numerical simulations have been performed under the flow conditions of $Ma_\infty = 0.8$ and $Re_\infty = 12 \times 10^6$.

5.1.1 Geometrical description

A cuboid cavity with a length-to-depth ratio (L_c/D_c) of 5.7 and length-to-width ratio (L_c/W_c) of 4.16 is cut into a flat side of a test rig at a certain distance from its sharp leading edge and on the centre line (see Fig. 5.1). The doors connected to the rig plate are placed on either side of the cavity with a positive Z pointing into the cavity. The experimental survey conducted by Mayer et al. [39] had probes placed at equidistant locations along the cavity ceiling, named $L1$ to $L8$, with the flow direction from the sharp leading edge of the rig towards the cavity. The flat plate upstream of the cavity is long enough to obtain a fully developed turbulent boundary layer before reaching the cavity.

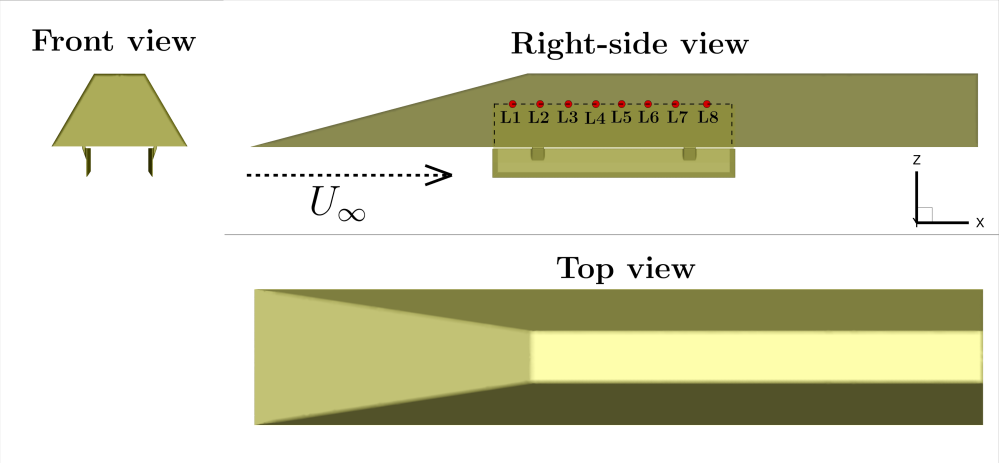

FIGURE 5.1: Weapon bay model with the position of probes [41]

5.1.2 Mesh

The numerical mesh used for all the turbulence models is of an unstructured type. The surface of the cavity walls, doors and the plate of the rig where the cavity is cut is composed of triangles and quadrilaterals. In order to encompass the boundary layer over the flat plate leading to the cavity, the surface elements follow up to 35 layers of prism and hexahedral elements in the case of wall-resolved simulation and up to 10 layers in the case of wall-modelled simulation with 0.012 L_c as the total thickness of the layers for the considered flow conditions (detailed mesh information is provided in Tab. 5.2). The sharp leading edge of the rig has been refined to avoid introducing mesh-dependent errors that could be convected and affect the flow over the cavity. The other regions of the sphere-shaped computational domain with a diameter as high as 50 L_c are unstructured elements with tetrahedral and pyramidal cells. The cavity ceiling near the front wall has lower values of y^+ compared to the aft part of the cavity, yet the number of prism layers has been kept the same. The model has been meshed in half and mirrored about the symmetry axis so that asymmetric grid effects are effectively avoided. The local regions in and around the cavity have been meshed based on the integral scale estimates obtained from the k-ω SST model.

Meshing approach in hybrid RANS-LES simulations

During the preliminary stages of the work, the goal was to generate a reference simulation database, which led to the testing of several meshes with the hybrid RANS-LES approach using the wall-integrated SA-IDDES model with overall uniform refinement in the cavity. The finest with a practical limit on the computing hours, led to several mesh nodes as high as 25×10^6. However, the wall-integrated meshes had limitations due to very skewed cells

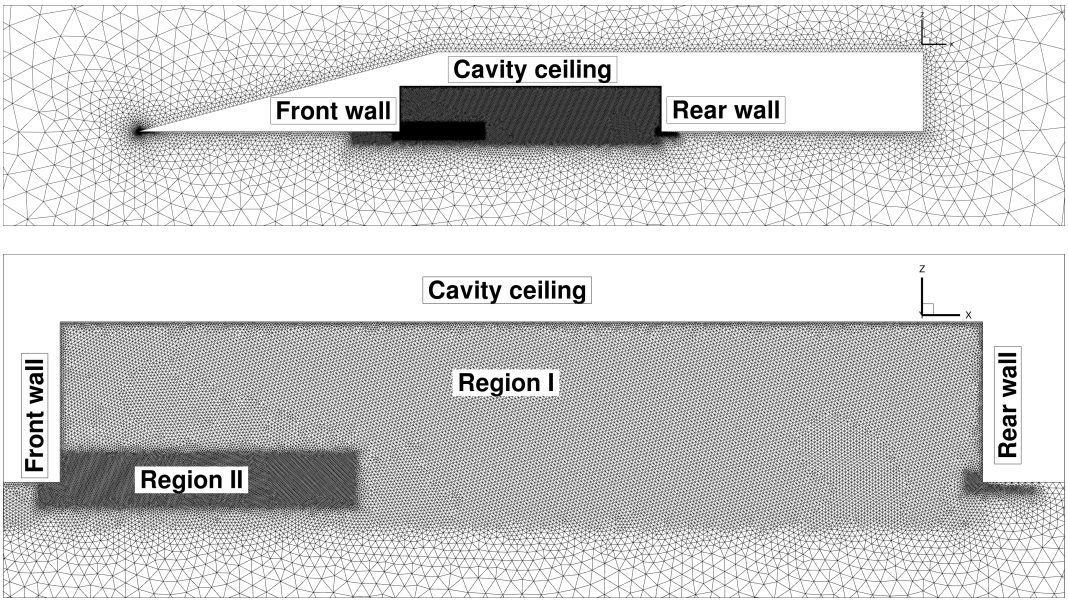

FIGURE 5.2: Mesh distribution in DES-WF [110]

near the gaps between cavity doors and walls. In general, there were severe convergence issues using matrix artificial dissipation schemes explained in the cavity results chapter 6. The mesh quality, specifically the decrease in cell orthogonality due to the utilization of coarser cells over cavity walls and in the gaps between the cavity door and walls, is preferred in the SA-IDDES model using a wall-modelled approach. In this approach, $2-3$ cells per integral length scale are utilized to resolve the shear layer. The resulting local mesh distribution is depicted in Fig. 5.2, where region I comprises cells with dimensions approximately $2.6 \times 10^{-3}\ L_c$, while region II's cells are half that size. The mesh resolution for DES-WF is determined by confirming the presence of a Kolmogorov inertial range [111], extending roughly over one order of magnitude. This condition has been verified in the shear layer, which can be seen in Fig. 5.3. The DES-WF mesh is composed of 5.4×10^6 grid nodes and 7.2×10^5 surface elements. Moreover, it has been observed that refining the entire shear layer does not provide further benefits for the prediction of resonance spectra.

Meshing approach in SAS simulations

The SAS approach explores three variants: SAS-WR, SAS-WF and SAS-F. SAS-WR implements the k-ω SST model with a wall-resolved technique, while SAS-WF utilizes a wall-modelled technique. SAS-F, on the other hand, leverages the forcing feature within SAS. In all the SAS variants, unlike DES-WF, regions I and II have the exact mesh resolution, and the scale-resolving capability of SAS does not explicitly depend

TABLE 5.1: Details of Mesh A, B and C for mesh refinement study in SAS-WR ($Ma_\infty = 0.8$ and $Re_\infty = 12 \times 10^6$)

	Mesh A	Mesh B	Mesh C
Number of mesh nodes	20.2×10^6	5.1×10^6	1.4×10^6
y^+ of the first element	1.0	1.0	1.0
Number of prism cells	35	35	35
Resolution in Regions I and II	$3.12 \times 10^{-3}L$	$6.24 \times 10^{-3}L$	$12.48 \times 10^{-3}L$

on the cell resolution but on the L_{vk} scale. In order to achieve sufficiently resolved turbulence in the cavity, the cell size has been chosen based on a mesh convergence study. Three meshes A, B and C of increasing cell sizes by a factor of 2.0 in each direction within the cavity have been chosen, which consist of 20.2×10^6, 5.1×10^6 and 1.4×10^6 nodes, respectively (see Tab. 5.1). The wall-normal resolution has been the same for all the meshes with y^+ values of the first cell less than 1.0. The SPL spectra are very sensitive to global mesh characteristics and resolution of the shear layer near the front edge and, therefore, are chosen for illustrating mesh convergence. The resulting spectra from SAS-WR on the three meshes are shown in Fig. 5.3. According to the results, mesh B has been chosen to perform the SAS-WR simulation. The SAS-WR mesh with prism cells contains around 5.1×10^6 grid nodes. In SAS-WF and SAS-F, the resolution in the cavity is the same as in SAS-WR with y^+ of the first element greater than 100, whereby the resulting mesh has the advantage of using only 50% of the prism cells compared to the SAS-WR mesh with 2.5×10^6 grid nodes. Tab. 5.2 summarizes the mesh parameters used for all the simulation method variants in the study for the cavity configuration.

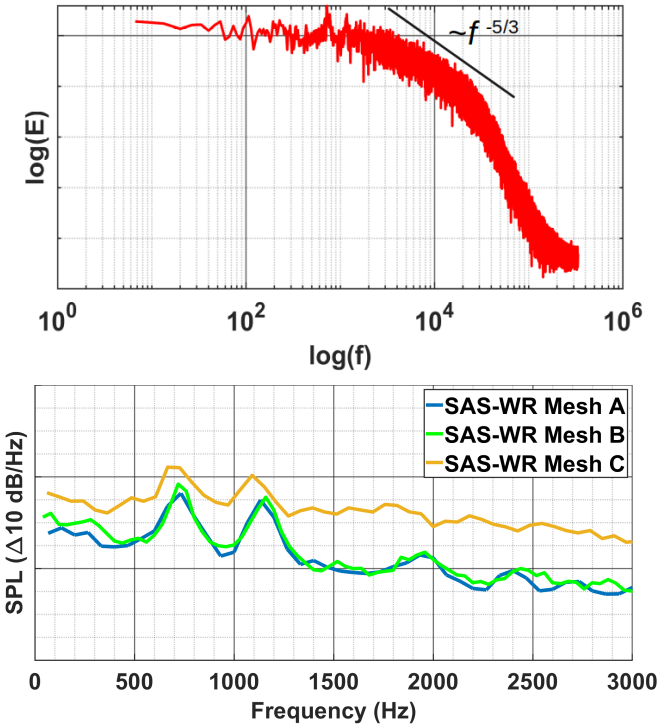

FIGURE 5.3: Mesh convergence study based on energy spectra observed in the shear layer ($Ma_\infty = 0.8$ and $Re_\infty = 12 \times 10^6$) [110]

TABLE 5.2: Details of the meshes used for the cavity simulation ($Ma_\infty = 0.8$ and $Re_\infty = 12 \times 10^6$)

	DES-WF	SAS-WR	SAS-WF	SAS-F
Number of mesh nodes	12.5×10^6	5.1×10^6	2.5×10^6	2.5×10^6
y^+ of the first element	> 100.0	< 1.0	> 100.0	> 100.0
Number of prism cells	10	35	10	10
Resolution in Region I	$3.23 \times 10^{-3} L_c$	$6.24 \times 10^{-3} L_c$	$6.24 \times 10^{-3} L_c$	$6.24 \times 10^{-3} L_c$
Resolution in Region II	$1.28 \times 10^{-3} L_c$	$6.24 \times 10^{-3} L_c$	$6.24 \times 10^{-3} L_c$	$6.24 \times 10^{-3} L_c$

5.1.3 Simulation setup

This subsection provides an overview of high-level control parameters utilized in the numerical computations. These parameters have demonstrated consistent accuracy following rigorous testing conducted throughout this study.

Numerical schemes

The simulations employed a second-order central scheme for spatial discretization with artificial dissipation schemes. Specifically, the convective mean-flow terms were treated with a skew-symmetric central scheme according to Kok [112]. In contrast, the convective terms of the turbulence equations were discretized with the central average of the analytic flux on each side of the face. A matrix artificial dissipation of 70% and a scalar artificial dissipation of 30% were set in the computations. The temporal discretization has been achieved through a dual-time stepping approach, which follows the approach of Jameson [113]. A second-order implicit backward method with the LUSGS algorithm is employed for discretizing the time-derivative to generate a sequence of (non-linear) steady-state problems, which make use of the singly diagonally implicit Runge-Kutta method (SDIRK) until a steady state in fictitious pseudo time is reached. The convective Courant-Friedrichs-Lewy number (CFL) has been kept around 1.0 for the DES simulations and $2.0 - 3.0$ for the SAS variants. The convergence criteria are based on Cauchy convergence control of the variables' volume-averaged turbulent kinetic energy, maximum eddy viscosity, total vorticity and maximum Mach number with tolerance values of 1×10^{-6} each. Further details regarding the DLR-TAU solver can be found in Galle et al. [114]. Moreover, in SAS-F simulation, the dimensions of the forcing zone have been chosen based on the shear-layer prediction from the URANS computations, as shown in Fig. 5.4, roughly extending 50% of the cavity length and 30% of the cavity depth. The highest levels of turbulent kinetic energy in URANS have been identified and enclosed by the forcing zone,

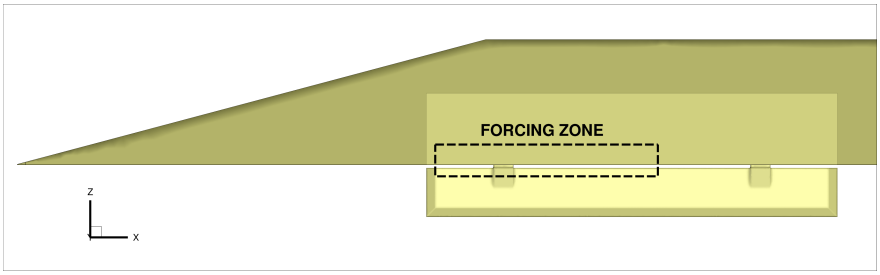

FIGURE 5.4: Forcing zone in SAS-F simulation [41]

as the contribution of the forcing term is directly proportional to the modeled turbulent kinetic energy as seen in Eq. 4.92.

Initial & Boundary conditions

In line with the measurements conducted at the transonic wind-tunnel facility in Göttingen (TWG) by Airbus Defense and Space (ADS), the flow conditions of $Ma_\infty = 0.8$ and $Re_\infty = 12 \times 10^6$ at $\alpha = 0°$ and $\beta = 0°/8°$ were chosen for the numerical analysis. The speed of sound is a function of T_∞ and has a simple relationship

$$a_\infty = \sqrt{\gamma R T_\infty} \tag{5.1}$$

and the dynamic viscosity is a function of T_∞, and ρ_∞ is a function of p_∞ and T_∞ through a thermodynamic equation of state. In order to match these non-dimensional numbers (Ma_∞ and Re_∞), the T_∞ is prescribed based on wind-tunnel data. Following this, the dynamic viscosity is computed from Sutherland's law [115] shown in Eq. 3.10, and p_∞ is computed through the ideal gas law

$$p_\infty = \rho_\infty R T_\infty \tag{5.2}$$

where R, the specific gas constant equals to $286.9 J/kgK$.
Ma_∞, Re_∞ and T_∞ were set as input conditions for the CFD calculations. The walls of the cavity were defined with no-slip velocity conditions. The farfield spherical surface is equipped with "farfield" boundary conditions, which are implemented in TAU, representing an inflow/outflow boundary located far from the analyzed configuration in external flow. The presence of the configuration hardly impacts the flow variables at the farfield boundary, where all gradients are assumed to be negligible, and consequently, no viscous effects are considered.

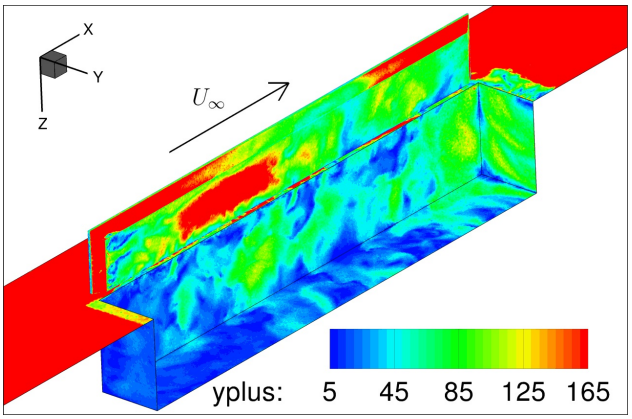

FIGURE 5.5: y^+ distance over the cavity walls in the DES-WF simulation at an instant of time ($Ma_\infty = 0.8$ and $Re_\infty = 12 \times 10^6$) [41]

5.1.4 Wall Treatment

In this study, wall functions based on the universal law of the wall are employed for the DES-WF, SAS-WF and SAS-F simulations, whereas the low-Re boundary condition is used for the SAS-WR simulation. Grid-independent wall functions aim to provide a boundary condition at solid walls that enable flow solutions independently of the location of the first grid node above the wall. As discussed in section 4.3.3, the RANS equations are solved only down to the first grid node above the wall and matched with an adaptive wall function solution. The matching condition (Eq. 5.3) makes sure that the wall-parallel components of the RANS solution and the wall function are equal at the wall distance y_δ, which is then solved for the friction velocity u_τ using Newton's method. The shear stress τ_ω is then prescribed at the wall node. Fig. 5.5 shows the instantaneous non-dimensional wall distance y^+ distribution in the case of the DES-WF simulation.

$$u_{RANS}(y_\delta) = u_{WF}(y_\delta) \tag{5.3}$$

5.2 Hybrid delta-wing planforms

In this section, the hybrid delta-wing planforms DW1 and DW2 are introduced. Following that, the meshing strategy utilized in the work is explained, accompanied by the presentation of mesh convergence plots based on aerodynamic coefficients.

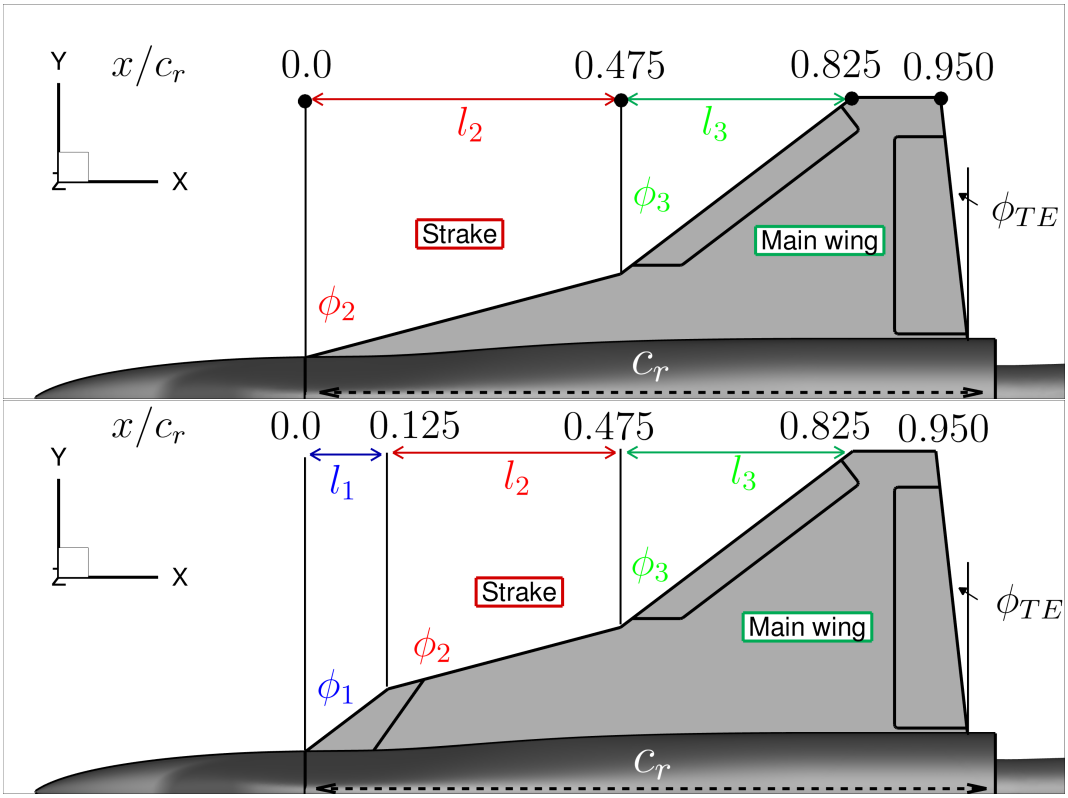

FIGURE 5.6: Geometric features of DW1 and DW2 planforms

5.2.1 Geometrical description: DW1 & DW2

Fig. 5.6 shows planform sketches of DW1 and DW2 configurations, which are 1:30-scaled versions composed of a generic fuselage and a generic flat-plate wing with a sharp leading edge. DW1 is characterized by a double-delta wing planform with two different leading-edge sections, whereas DW2 features a triple-delta wing planform with three different leading-edge sections [116]. The wing thickness of the planforms is around $0.014L$, and the wing configuration is equipped with different flat-plate wing planforms, including sharp leading edges and sets of corresponding control surfaces such as levcon, slat and flaps. The leading-edge sweep angle of the outer main wing section of both the planforms is $\phi_3 = 52.5°$. The strake section in DW1 exhibits one highly-swept strake with a leading-edge sweep angle of $\phi_2 = 75°$, whereas DW2 exhibits two different leading-edge sweep angles of $\phi_1 = 52.5°$ and $\phi_2 = 75°$. The nautical labelling is used: leeward starboard $(y > 0)$ and windward portside $(y < 0)$. The geometrical parameters of the planforms have been listed in Tab. 5.3

TABLE 5.3: Geometrical parameters of DW1 and DW2

	DW1	DW2
l_1/c_r	-	0.125
l_2/c_r	0.475	0.350
l_3/c_r	0.350	0.350
ϕ_1	-	52.5°
ϕ_2	75°	75°
ϕ_3	52.5°	52.5°

5.2.2 Mesh

Meshing strategy for DW1 is followed based on previous studies by Di Fabbio et al. [116] for DW2 configuration. The numerical mesh used for both the planforms is of unstructured type. The surface of the walls is composed of triangles. Tetrahedral grids used in boundary layers frequently exhibit high aspect ratios and pronounced non-orthogonality, which can complicate the computation of the gradient divergence, as noted by [117]. In contrast, prism grids are characterized by more excellent orthogonality and impose a lighter computational load on the solver. Therefore, to resolve the boundary layer over the flat-plate planforms, up to 35 layers of structured triangular prism elements are used for the surface elements, with the first cell having $y^+ \approx 1$. The height of the prismatic layer has been kept constant over the entire planform and not locally adjusted to the actual height of the local boundary layer. As a result, flow features like the shear layer and the resulting vortices extend in and out of the boundary between structured and unstructured mesh elements. The sharp leading edges have been refined to prevent the introduction of mesh-dependent errors that might be convected and affect the flow over the wings. The other regions of the sphere-shaped computational domain with a diameter as high as $50C_r$ are composed of unstructured elements with tetrahedral and pyramid cells. The model has been meshed in half and mirrored about the symmetry axis so that asymmetric grid effects are effectively avoided. Isotropic mesh refinement has been applied in the vortex regions. A mesh convergence study was performed, and the resulting mesh was used for the RANS simulation. In the case of SAS simulations, local regions within and around the configuration have been refined based on integral scale estimates obtained from the k-ω SST model. $2-3$ cells per integral length scale have been used to resolve the vortex and surrounding regions. Fig. 5.7 shows the resulting surface and volume mesh distribution for the SAS simulation, with cells clustered in the boundary layer and around the vortex region. The configurations feature viscous no-slip walls, and the domain has

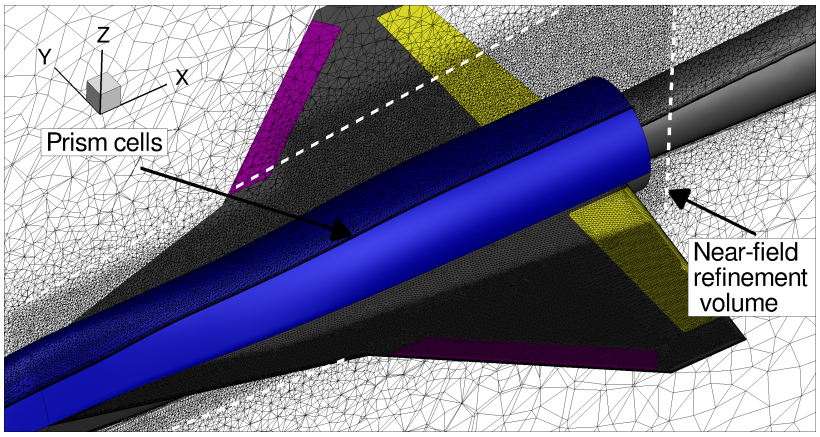

(a) Surface mesh distribution

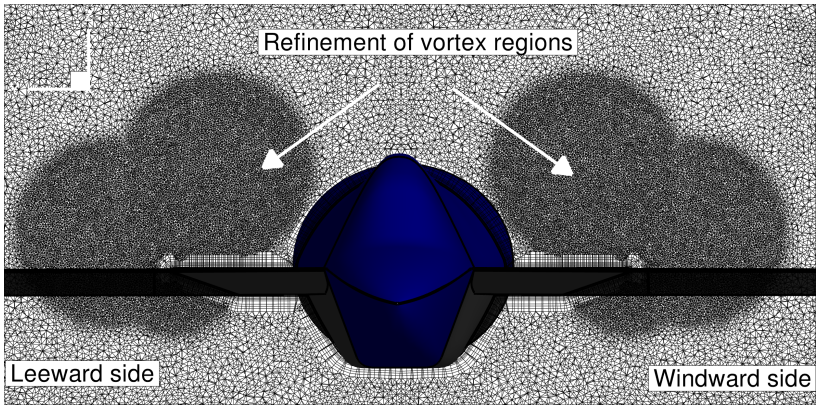

(b) Volume cells distribution at $x/C_r = 0.4$

FIGURE 5.7: DW1 mesh topology in SAS showing local refinement regions

farfield flow conditions of an undisturbed flow within the surrounding sphere. Five meshes (labelled A to E) were chosen for the study, featuring progressively finer resolution in each direction within the vortex regions, with a growth factor of 1.5. These meshes have sizes of 2.8×10^6, 4.8×10^6, 10.4×10^6, 27.3×10^6, and 82.2×10^6 nodes, respectively (see Tab. 5.4). The wall-normal resolution was consistent across all meshes, ensuring that the first cell's y^+ value remained below 1.0. The resulting aerodynamic coefficients obtained from these meshes are depicted in Fig. 5.8. It is seen that the meshes D and E converge to similar values of lift and moment coefficients. The oscillation frequency of the coefficients diminishes as mesh resolution increases. Based on these results, mesh D with 27.3×10^6 nodes were selected for the RANS simulation. In the SAS simulations, the vortex-core regions have been made sure that $2 - 3$ cells are placed to resolve integral length scales, resulting in a similar mesh as that of mesh D with around 30×10^6.

TABLE 5.4: Details of Mesh A to E for mesh refinement study ($Ma_\infty = 0.85$ and $Re_\infty = 12.53 \times 10^6$)

	Mesh A	Mesh B	Mesh C	Mesh D	Mesh E
Number of mesh nodes	2.8×10^6	4.8×10^6	10.4×10^6	27.3×10^6	82.2×10^6
y^+ of the first element	1.0	1.0	1.0	1.0	1.0
Number of prism cells	35	35	35	35	35
Resolution in vortex regions	$0.0006C_r$	$0.0042C_r$	$0.0025C_r$	$0.0018C_r$	$0.0012C_r$

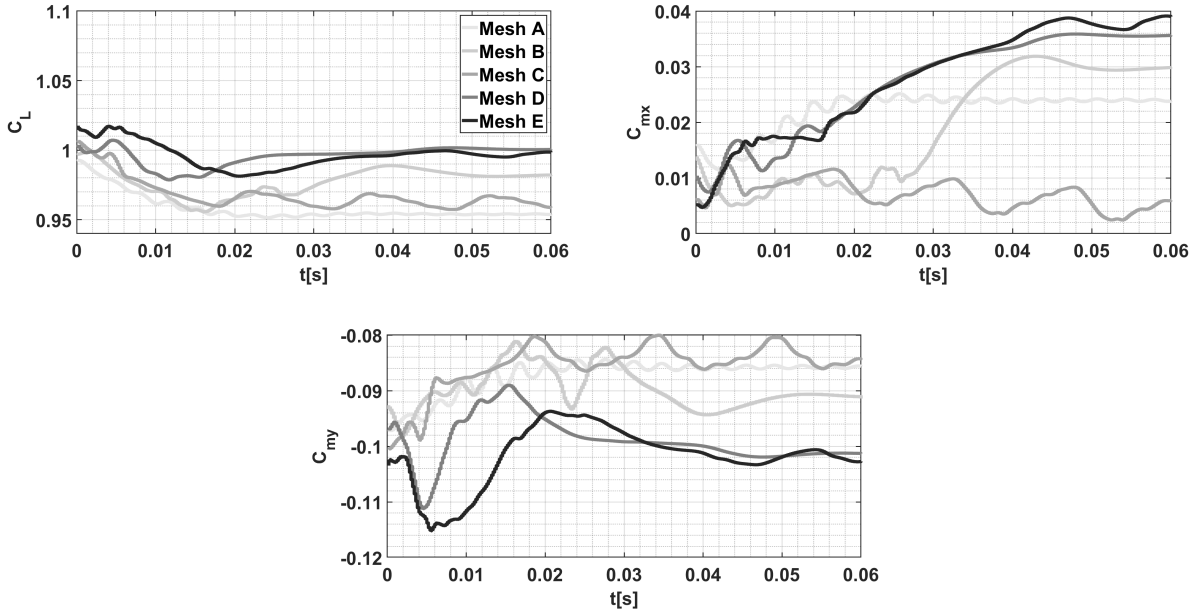

FIGURE 5.8: Mesh convergence study at $\alpha = 20^\circ$ and $\beta = 5^\circ$ in DW1 using URANS $k - \omega$ SST model ($Ma_\infty = 0.85$ and $Re_\infty = 12.53 \times 10^6$)

5.2.3 Simulation setup

This subsection explains the numerical settings and boundary conditions used in the delta-wing simulations.

Numerical schemes and boundary conditions

Similar to the cavity flow simulations, delta-wing simulations also employ a second-order central scheme for spatial discretization with matrix dissipation schemes. The temporal discretization has been achieved through a dual-time stepping approach, which uses a second-order implicit method. One order of reduction in density residuals has been achieved between the time steps in the computations. The initial and boundary conditions for delta-wing flows are set similar to the procedure explained in section 5.1.3. The surfaces of the delta-wing configurations are treated as no-slip walls.

Chapter 6

Results of cavity flow

This chapter is organized into the following sections: Section 6.1 emphasizes the acceptable tolerance range for the simulation results from analyzing the experimental data. Section 6.2 delves into examining the open-cavity configuration utilizing the SA-IDDES model. The investigations of the SAS approach are detailed in section 6.3, which explores various near-wall and turbulence treatments as part of an efficient turbulence-resolving approach for cavity flows. The results are then compared with the results of the SA-IDDES model. Having tested different simulation approaches on the configuration, section 6.4 focuses on simulating the cavity under asymmetric flow conditions with the SAS-WR model to examine the directional effects on resonant modes. The outcomes of these simulations are presented and discussed. The results presented in this chapter include the flow conditions of $Ma_\infty = 0.8$ and $Re_\infty = 12 \times 10^6$ and are published in articles [118, 110, 119].

6.1 FFT analysis of experimental data

Before conducting the simulations, data sampling effects to understand the impact of signal length on FFT and RMS statistics are sought. In order to estimate this impact, a fundamental analysis of the raw data is performed. A total of 20.0s of pressure measurement data is available for validating simulation results, which was divided into two groups: one with 160 samples of 0.125s each and the other with 40 samples of 0.5s each. Fig. 6.1 illustrates the RMS pressure for both sample groups. In the 0.125s case, RMS deviation is approximately 350 Pa near the front edge of the cavity ($x/L_c = 0$ to $x/L_c = 0.2$), increasing to around 500 Pa near $x/L_c = 0.9$. Conversely, in the 0.5s case, RMS deviation is around 100 Pa near $x/L_c = 0.2$, rising to 350 Pa near $x/L_c = 0.9$. The FFT analysis of the two sample groups reveals significant differences in amplitude levels. For the 0.125s sample duration, amplitude levels vary by approximately $8 - 9$ dB/Hz, while for the 0.5s duration, the variation reduces to around $4 - 5$ dB/Hz. This analysis highlights the importance

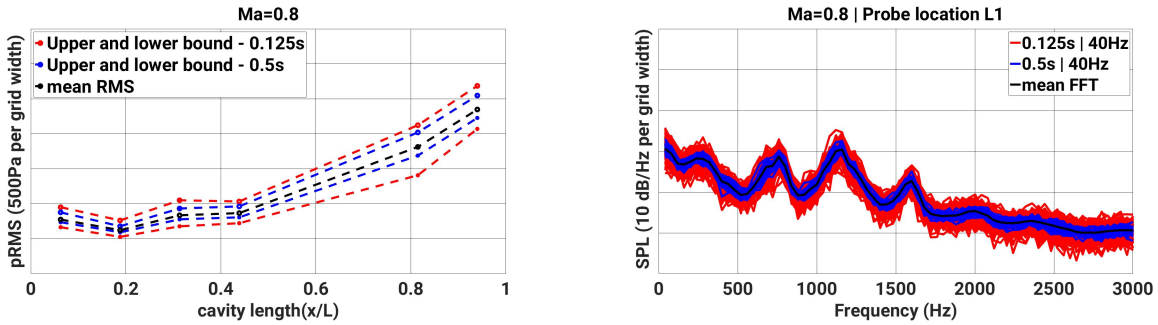

(a) RMS pressure over the cavity ceiling for sample groups 0.125s and 0.5s (b) Pressure spectra for sample groups 0.125s and 0.5s

FIGURE 6.1: Data sampling effects showing the effect of signal length on RMS pressure and pressure spectra in experimental data at $Ma_\infty = 0.8$ [118]

of selecting signal sample sizes for validating simulation data. It underscores how the choice of sample length directly impacts the accuracy of simulation results and offers insights into the realistic accuracy levels achievable in simulations by acknowledging the inherent uncertainty in experimental data. Allen et al. [33] conducted simulations on the M219 cavity with an L_c/D_c ratio of 5.0 at a freestream Mach number (Ma_∞) of 0.85, recommending a minimum sample length of 0.5s. Following the assessment of data sampling effects, and given the similarity between the open-cavity configuration used in this study and the M219 configuration, this recommendation of 0.5s sample duration is aimed in the simulations, except in DES-WR simulation.

6.2 Investigations using the hybrid RANS-LES approach

In RANS simulations, using artificial dissipation in the central scheme is essential for stabilizing the simulation. However, when dealing with scale-resolving simulations like hybrid RANS/LES, it becomes crucial to minimize artificial dissipation to avoid excessive damping of resolved turbulent structures. In addition to adopting low-dissipation settings, employing a low-dispersive reconstruction in the skew-symmetric convective fluxes, as described in [120], results in the LD2 (low-dissipation low-dispersion) scheme. This approach can further improve the accuracy of scale-resolving simulations. In using such a low-dissipation, low-dispersion scheme, a matrix artificial scheme was chosen for the SA-IDDES model employing a wall-integrated approach, referred to as DES-WR in this study, which has shown stability issues with potentially skewed cells near the door hinges causing the trouble. In order to overcome stability issues, scalar dissipation has been chosen in the wall-integrated SA-IDDES model. Subsequently, greater computational

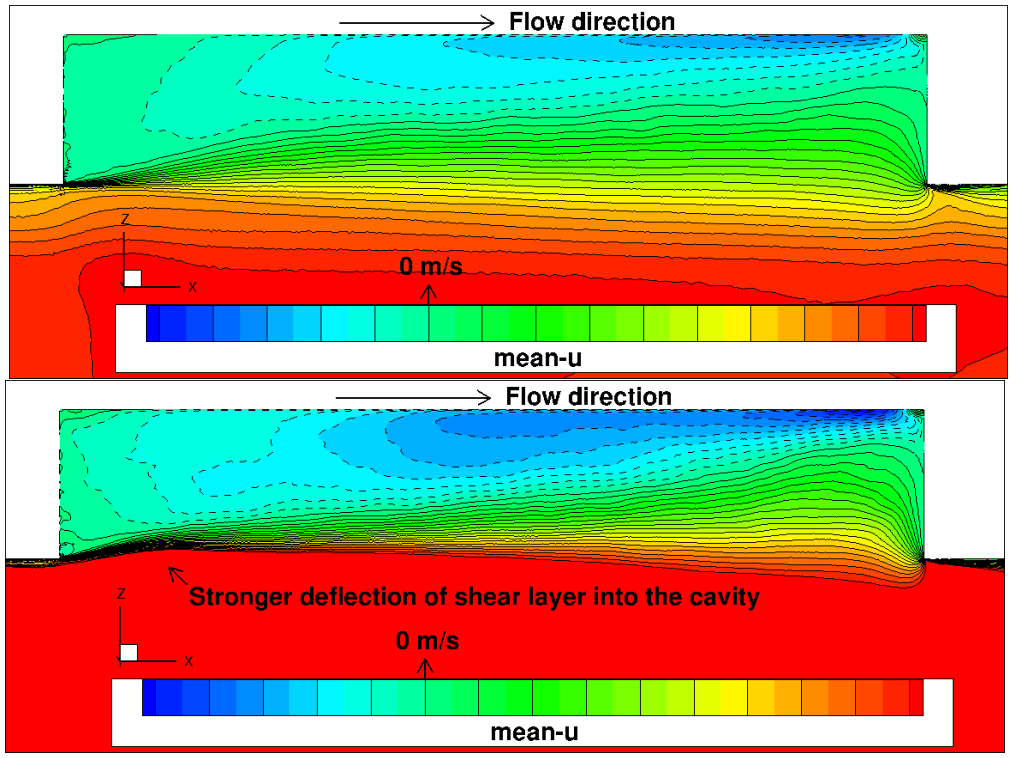

FIGURE 6.2: Time-averaged streamwise velocity contour at mid-plane y=0: $Ma_\infty = 0.8$ (top); $Ma_\infty = 1.2$ (bottom) averaged over $0.125s$ [119]

robustness was achieved with a scalar dissipation scheme and their results under Mach numbers $Ma_\infty = 0.8$ and $Ma_\infty = 1.2$ are shown in the article by Rajkumar et al. [119]. Fig. 6.2 shows the time-averaged streamwise velocity contours at midplane y=0 for $Ma_\infty = 0.8$ and $Ma_\infty = 1.2$. It can be seen that the shear layer develops from the front edge of the cavity wall and it impinges directly on the rear wall, which is an expected behavior from the open cavity configuration. Flow structures which impinge on the edge of the rear wall get either redirected inside the cavity or travel further downstream depending on the angle of flow impingement on the rear wall edge. The flow structures redirected inside the cavity form a large recirculation region. The negative contour levels have been marked with dotted lines for better visibility of upstream traveling components. The shear layer in $Ma_\infty = 1.2$ deflects by a little margin into the cavity near the front edge. In contrast, the shear layer in $Ma_\infty = 0.8$ shows no such visible deflection, which makes the recirculation region in the cavity of $Ma_\infty = 1.2$ more slender than in $Ma_\infty = 0.8$. Fig. 6.3 shows the plot of root mean square (RMS) of pressure along the centerline of the ceiling of the cavity compared with the measured data. The simulated RMS data fit the experimental data reasonably well with a slight underprediction of values near 80% of the cavity length. It is evident from the surface RMS pressure distribution on the right

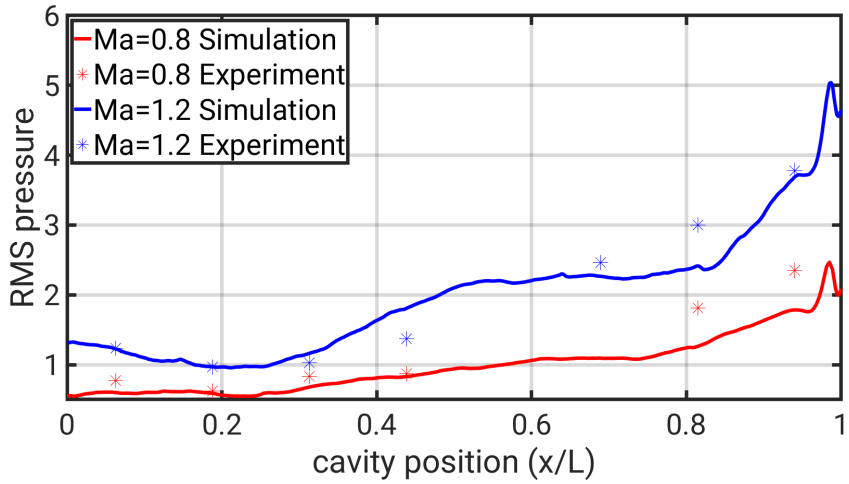

FIGURE 6.3: Comparison of the RMS pressure in $Ma_\infty = 0.8$ and $Ma_\infty = 1.2$ using DES-WR calculated with $0.125s$ of simulated time compared with experiment along the ceiling at $y = 0$ [119]

TABLE 6.1: Frequencies of Rossiter modes in theory, experiment and DES-WR at $Ma_\infty = 0.8$ [119]

	$Ma_\infty = 0.8$			$Ma_\infty = 1.2$		
Mode	Theory (Hz)	Exp.	DES-WR	Theory	Exp.	DES-WR
1	263	272	266	352	352	345
2	670	755	752	896	888	856
3	1076	1160	1144	1440	1464	1444
4	1484	1600	1622	1985	2640	2533

of Fig. 6.3 that the pressure fluctuations are substantially higher in the second half of the cavity than in the first half with maximum RMS values on the rear wall due to complex interactions of shedding vortices with it.

Power spectral density (PSD) measures energy contained in the pressure signal as a function of frequencies. Fig. 6.4 and 6.5 show the PSD spectra for some of the probe locations along the cavity ceiling for $Ma_\infty = 0.8$ and $Ma_\infty = 1.2$, respectively. Tab. 6.1 shows the frequencies of the modes computed from the modified Rossiter model (Eq. 2.2), measured data together with the simulation results. A Fast Fourier Transform (FFT) has been performed based on Welch's method to decompose the pressure fluctuations into their frequency components. In DES-WR simulations, $0.125s$ of physical time has been collected and processed for the FFT analysis using the Hamming window function with the maximum offset length of FFT windows corresponding to the integral time scale computed

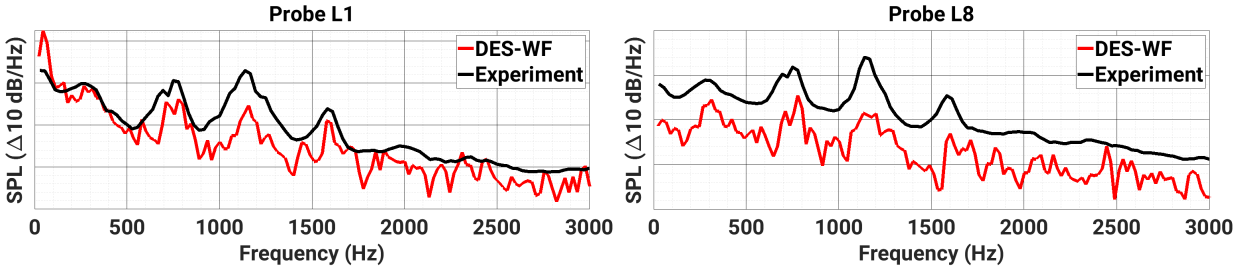

FIGURE 6.4: SPL at probes $L1$ and $L8$ in $Ma_\infty = 0.8$ using DES-WF processed with $0.125s$ of sample data in comparison with measurement data

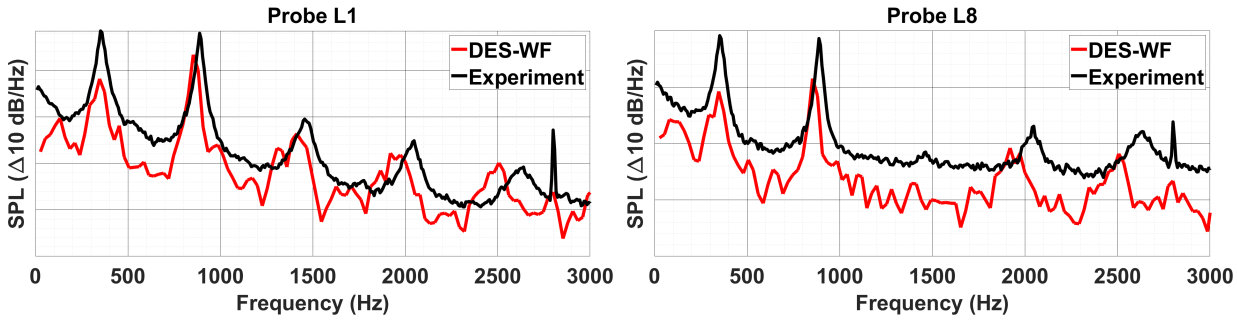

FIGURE 6.5: SPL at probes $L1$ and $L8$ in $Ma_\infty = 1.2$ using DES-WF processed with $0.125s$ of sample data in comparison with measurement data

through the autocorrelation function. For comparison with the experimental data, results of the numerical simulations have been plotted together in Fig. 6.4 and 6.5. The lowest frequency the simulated data can resolve is kept around $30Hz$. The numerical simulations agree with the modes and frequencies of the experimental results. At probe location $L1$, the mode 1 has been captured well, with higher modes showing slight underprediction. However, the frequencies have been predicted quite well in all the modes. At probe location $L8$, which has higher modal amplitudes than $L1$, all the modes have been captured well with moderate under-prediction in the spectral magnitudes. However, the relative magnitudes between the modes are correctly captured. In $Ma_\infty = 1.2$, the modal shapes are captured quite well in the probe locations. It is evident from Tab. 6.1 that the increase in Mach number has shifted the frequencies of the modes to higher frequencies, and the numerical simulation has effectively captured this behavior. In particular, the distinct modes appearing in the experimental data have been captured better than in $Ma_\infty = 0.8$ case. As the frequencies increase, the Rossiter modes computed in the simulations slightly shift to the left relative to the experimental data. The results are highly accurate since the $0.125s$ has an uncertainty range of $8 - 9db/Hz$ in data sampling investigations (see section 6.1).

6.2.1 Results of SA-IDDES model using wall function (DES-WF)

The wall-function technique helps mitigate skewed cells near door hinges and between doors and cavity walls, improving simulation stability with the matrix dissipation scheme and enhancing accuracy. The results obtained with these refined numerical settings are compared with other simulation approaches in this study, notably different variants of the SAS method. It also allows for a longer sample length of $0.5s$, following recommendations from prior open cavity-flow studies like Allen et al. [33]. Henceforth, we refer to the simulation based on SA-IDDES using a wall-function approach as 'DES-WF'. Moreover, the case of $Ma_\infty = 0.8$ has been considered to investigate the DES-WF approach and further approaches in the following sections.

Instantaneous and time-averaged features of flow field

The resolution of vortical structures is crucial to obtain the acoustic spectra reasonably. At an instant, vortical structures in the shear layer and inside the cavity are shown in Fig. 6.6(a) for $Ma_\infty = 0.8$. The ability to resolve those vortical structures is attributed to using the SA-IDDES turbulence model. Due to proprietary reasons, only the relative magnitude levels of contour values are presented, and the same is followed for all the results shown. It can be seen that the vortical structures have a high magnitude of vorticity on the doors of the cavity near the front wall. The evolution of a typical vortex structure in the shear layer with time is that it develops from the front edge of the cavity and combines with other turbulent structures as they are convected downstream and dissipate after impinging on the rear wall of the cavity. On the impingement of the vortex structure on the rear wall, a transverse traveling pressure wave is generated and travels upstream to reflect off on other cavity walls [121]. Highly turbulent behavior is apparent on the downstream corner of the cavity near the rear wall, with the redirected flow stream interacting with the oncoming shear flow components (see Fig. 6.6(b)). A RANS model would not be able to capture these behaviors in the cavity, which are the typical underlying physics of open-cavity flows.
Fig. 6.7(a) shows the RMS pressure distribution over the cavity walls and doors in $Ma_\infty = 0.8$. Since the flow condition is symmetric, only half of the model is shown. It can be observed that the pressure fluctuations increase gradually along the cavity length, with significantly higher levels observed in the rear part of the cavity where the shear layer impacts the cavity walls. A similar pattern is observed on the cavity doors. A line data has been extracted along the centerline of the ceiling of the cavity and they have been compared with the measured data (see Fig. 6.7(b)). Similar to the RMS pressure profile of $Ma_\infty = 0.8$ in DES-WR results shown in Fig. 6.3, the simulated RMS pressure fit the

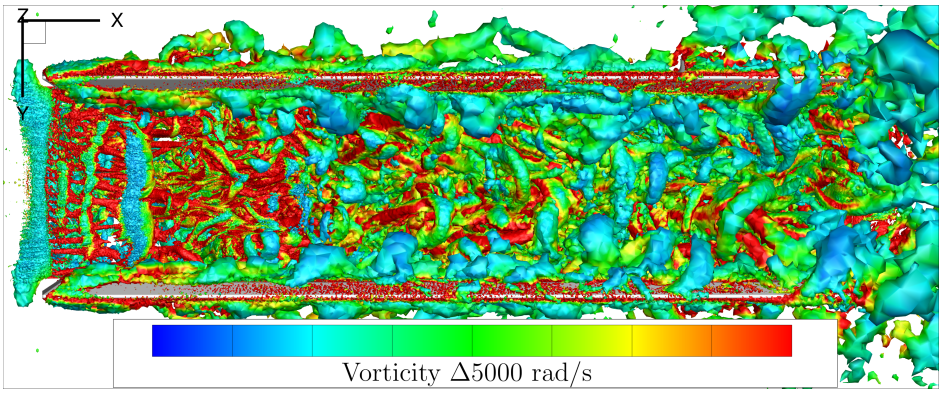

(a) Turbulent flow structures observed through Q-Criterion coloured by vorticity magnitude

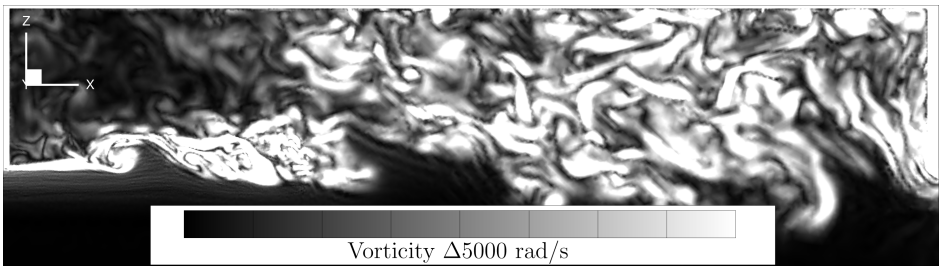

(b) Vorticity magnitude in plane $y = 0$ showing vortex shedding

FIGURE 6.6: Instantaneous features in $Ma_\infty = 0.8$ using DES-WF

experimental data reasonably well with a slight underprediction of values near 80% of the cavity length.

Fig. 6.8 shows the dynamics of the shear layer observed at the central plane $y = 0$ in $Ma_\infty = 0.8$. The extent and width of the shear layer have been observed through time-averaged du/dz (see Fig. 6.8(a)). It is observed that the shear layer extends up to 50% of the cavity length, which then loses its energy before it impinges on the rear wall. The width of the shear layer is about 50% of the cavity depth. The resolved fluctuations $\overline{u'w'}$ as seen in Fig. 6.8(b) start to develop at the lip of the cavity and grow into the cavity, showing increased levels of intensity in the second half of the cavity length. Along $y = 0$ and about the height of the cavity lip, some turbulent spectral analyses have been carried out, and one of them has been explained in Fig. 5.3.

Spectral analysis

In DES-WF, unsteady pressure data were collected in the probe locations $L1 - L8$ for a physical time of $0.5s$ corresponding to over 500 convective time units (CTU). A fast Fourier transform (FFT) has been performed on the collected data based on Welch's method

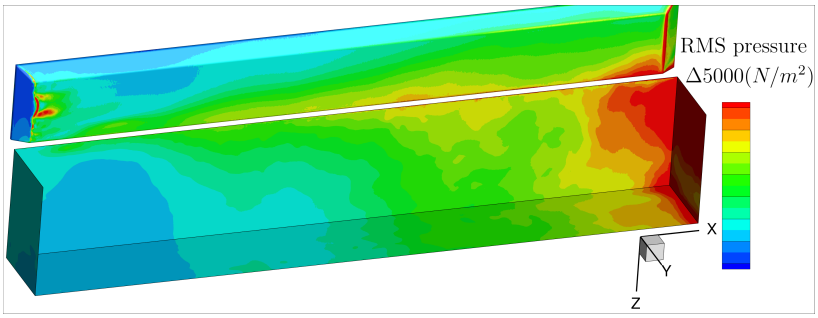

(a) RMS pressure surface distribution over the cavity walls

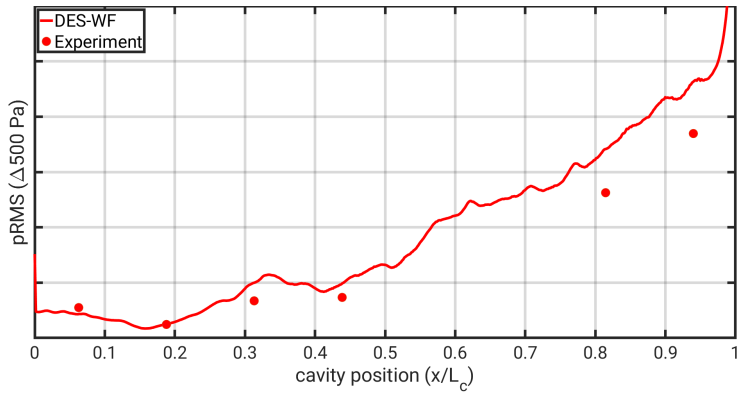

(b) RMS surface pressure validation along the cavity ceiling extracted at $y = 0$

FIGURE 6.7: Comparison of RMS pressure predicted by experiment and DES-WF in $Ma_\infty = 0.8$

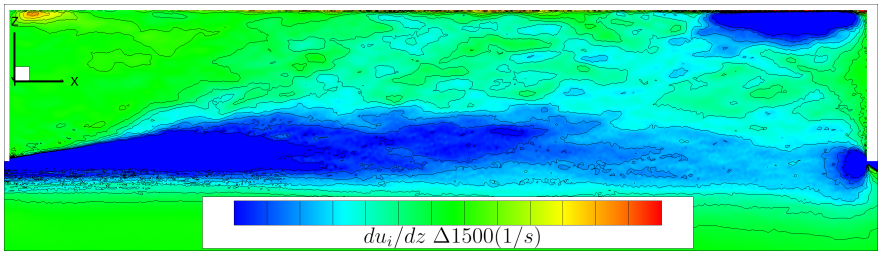

(a) Width of shear layer visualised by the streamwise wall-normal velocity gradient

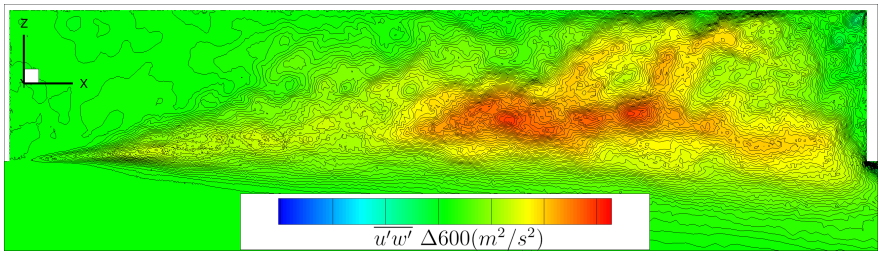

(b) Resolved fluctuations along the shear layer observed through the Reynolds stress $\overline{u'w'}$

FIGURE 6.8: Shear layer dynamics observed at $y = 0$ in $Ma_\infty = 0.8$ using DES-WF

TABLE 6.2: Resonant modes prediction by Rossiter model, experiment and DES-WF at $Ma_\infty = 0.8$

Mode	Theory	Exp.	DES-WF
1	263	272	278
2	670	755	722
3	1076	1160	1167
4	1484	1600	1611

to decompose the pressure data into its frequency components. The data have been processed for the FFT analysis using the Hamming window function with the maximum offset length of FFT windows corresponding to the integral time scale computed through the autocorrelation function. The lowest frequency the simulated data can resolve is around 40 Hz. The first four modal frequencies are listed in Tab. 6.2 for theoretically computed modes from the modified Rossiter model (Eq. 2.2), measurement and DES-WF simulation for $Ma_\infty = 0.8$. It is observed that frequency prediction from DES-WF agrees well with both the theoretical and measured frequencies, with a slight difference in mode 2 frequency.

The spectral comparison between measurement and simulation data at probe locations $L1$ to $L8$ is depicted in Fig. 6.9. The comparison at $L5$ is omitted due to insufficient

experimental data at that specific location. Overall, the spectral prediction aligns quite well, although there are instances of mode 2 being over-predicted at probe locations in the first half of the cavity.
In addition to the probe locations $L1 - L8$ on the cavity ceiling, unsteady pressure data have also been collected in plane $y = 0$ of the cavity at locations with a spatial resolution of $0.02L_c$ in the streamwise direction and $0.04D_c$ in the transverse direction. FFT analysis has been performed on all the data locations over the centre plane, and on each of the locations, the amplitude of the first four resonance modes was identified and interpolated to visualise the shape of the modes shown in Fig. 6.10. Rossiter mode 1 has a node in the centre of the cavity, anti-nodes on both ends, and the front part is significantly overlayed by the shear layer, which suppresses the mode with its broadband frequency ranging between $150 - 450$ Hz. The higher-order Rossiter modes 2, 3 and 4 correspond to the standing waves resulting from the organized vortical structures between the front and rear walls of the cavity. It is also observed that the shear layer overlays the lip of the cavity in all the modes. This result is consistent with the experimental findings by Wagner et al. [20], which explains the relationship between the acoustic tones and flow structure in transonic open cavity flow.

6.3 Investigations using the SAS approach

This subsection presents the performance of the different SAS variants, namely SAS-WR, SAS-WF and SAS-F. SAS-WR implements the k-ω SST model with a wall-resolved technique, while SAS-WF utilizes a wall-modelled technique. SAS-F, on the other hand, leverages the forcing feature within SAS. Additionally, some of the flow details of the cavity, such as the turbulent kinetic energy, vorticity magnitude and Reynolds stress, will be presented, as well as the resolution capability of the turbulent structures of the different simulation methods.

6.3.1 Prediction of SPL

Fig. 6.11 shows the FFT data of the experiment, DES-WF, SAS-WR, SAS-WF and SAS-F simulations for the probe locations L2 and L8. $20.0s$ of experimental sample data have been divided into 40 samples each containing 0.5 s. Each sample has been processed, and its average FFT result is shown in Fig. 6.11 in black colour, with which the simulation results are compared for validation. The Rossiter frequencies are captured extremely well by the DES-WF, SAS-WR, and SAS-F simulations, while SAS-WF shows a trend in

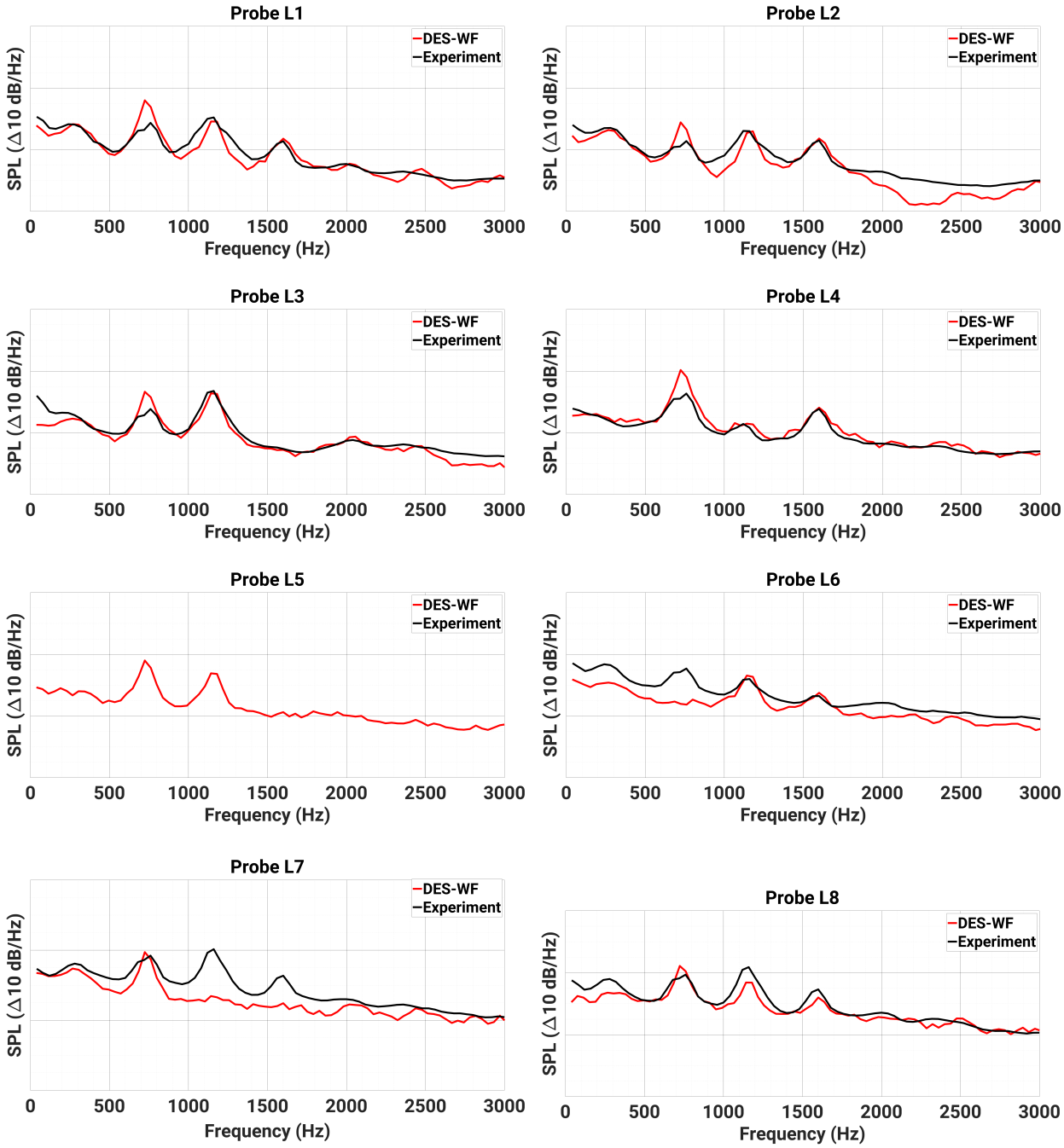

FIGURE 6.9: Comparison of cavity spectra at probe locations $L1 - L8$ in $Ma_\infty = 0.8$ using DES-WF with experiment

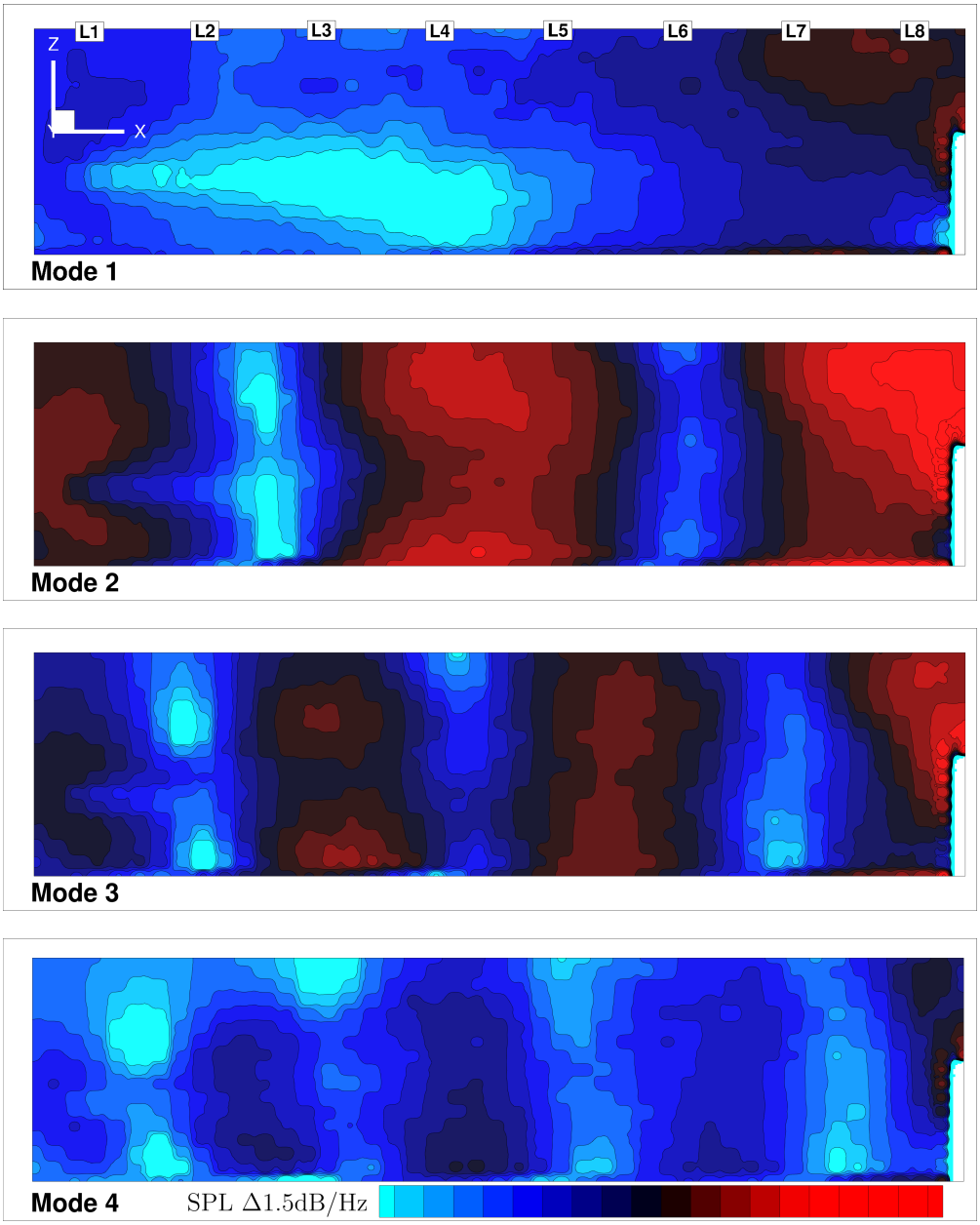

FIGURE 6.10: SPL of the Rossiter modes in plane $y = 0$ in $Ma_\infty = 0.8$ using DES-WF with left-to-right flow and probe locations marked on the ceiling (lack of data shown as white at the end of the cavity) [110]

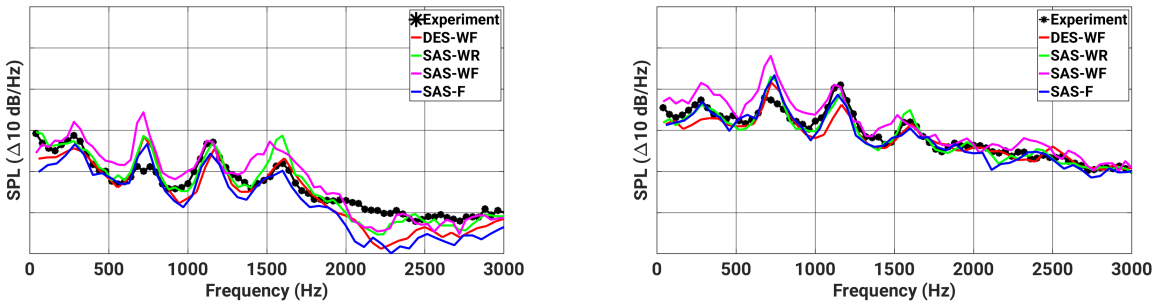

(a) Probe location L2

(b) Probe location L8

FIGURE 6.11: Comparion of SPL at probe location $L2$ and $L8$ in $Ma_\infty = 0.8$ using DES-WF, SAS-WR, SAS-WF and SAS-F with measurement data [110]

mispredicting the higher modal frequencies. Regarding magnitude, at the probe location L2, the mode 1 is predicted well by the DES-WF, SAS-WR and SAS-F simulations. Mode 2 is over-predicted significantly by the SAS-WF simulation, whereas mode 3 has been captured well by all the simulations. In general, the SAS-WF simulation mispredicts the modal amplitudes but shows the tendency to capture the frequencies and the DES-WF and SAS-WR simulations. Modes 2, 3 and 4 are captured adequately well by SAS-WR, SAS-WF and SAS-F simulations.

To summarize the spectral results, it is observed that the overall behavior of the simulations is excellent in terms of frequency prediction. However, the magnitudes between the simulations show noticeable differences. In particular, the SAS-WR and SAS-F simulations fit the magnitude levels and the DES-WF simulations. The SAS-WF simulation shows some promising trends in predicting the spectral distribution with scope for improvement in its magnitude prediction capability, which has been achieved by applying the artificial forcing method (i.e., SAS-F).

6.3.2 Prediction of RMS Pressure

Fig. 6.12 shows the plot of the RMS pressure along the centerline of the cavity ceiling compared with the measured data. The predicted RMS pressure fits the experimental data extremely well in the DES-WF and SAS-F simulations. In the SAS-WR simulation, the predicted values fit the experimental data within the first third of the cavity length, overpredict in the middle region and capture reasonably well towards the rear portion. In the SAS-WF simulation, the RMS profile follows the trend of the DES-WF simulation quite well but significantly overpredicts the values towards the regions of higher pressure RMS. The overpredicting behavior of SAS-WF is also perceivable from the distribution of the

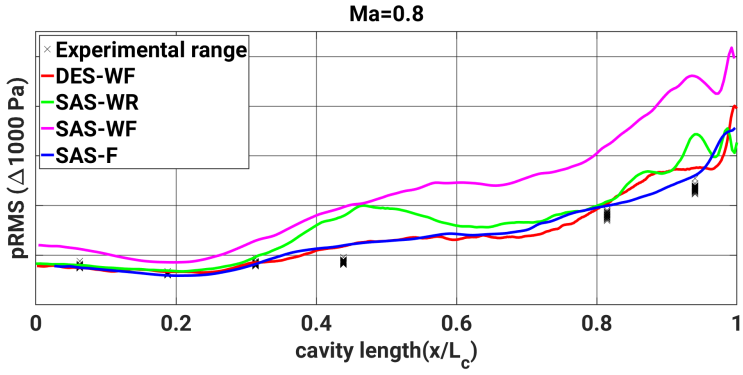

FIGURE 6.12: Comparison of the RMS pressure in $Ma_\infty = 0.8$ using DES-WF, SAS-WR, SAS-WF and SAS-F with measurement data [110]

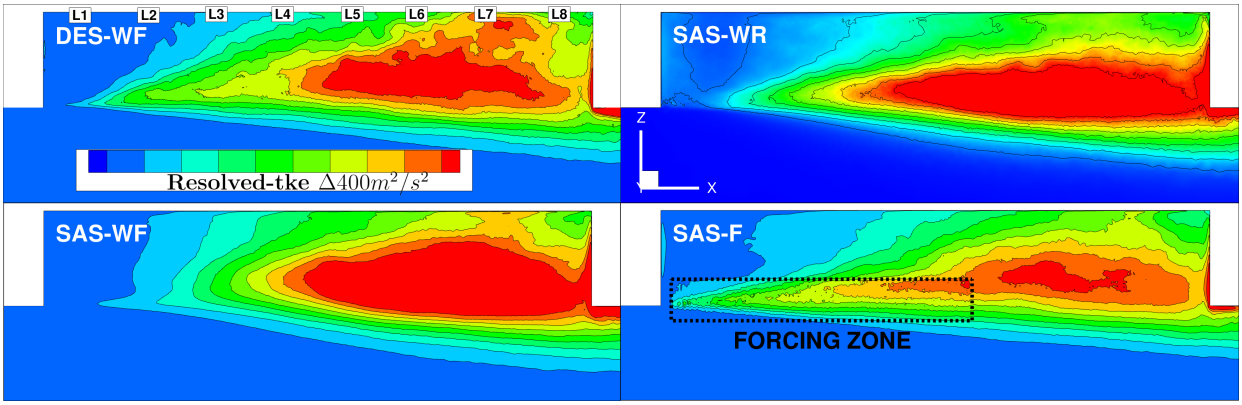

FIGURE 6.13: Comparison of resolved turbulent kinetic energy in $Ma_\infty = 0.8$ using DES-WF, SAS-WR, SAS-WF and SAS-F [110]

resolved turbulent kinetic energy, as shown in Fig. 6.13. The reason for the over-prediction in the SAS-WF simulation is related to the delayed production of resolved structures in the shear layer. The activation of the Q_{SAS} term has been delayed, and, thereby, the shear-layer breakup prediction shows a different behavior than the DES-WF simulation. This delayed prediction of the shear layer has a consequent effect of higher fluctuation intensity over the midsection of the cavity. The shear-layer breakup is considerably delayed compared to both the DES-WF and SAS-WR simulations, and clearly, this has increased the scale of the fluctuations by a significant margin in the second half of the cavity. In the SAS-F simulation, the forced fluctuations near the lip of the cavity have led to a better prediction capability of the resolved turbulence, and consequently, a better prediction of the RMS pressure is achieved.

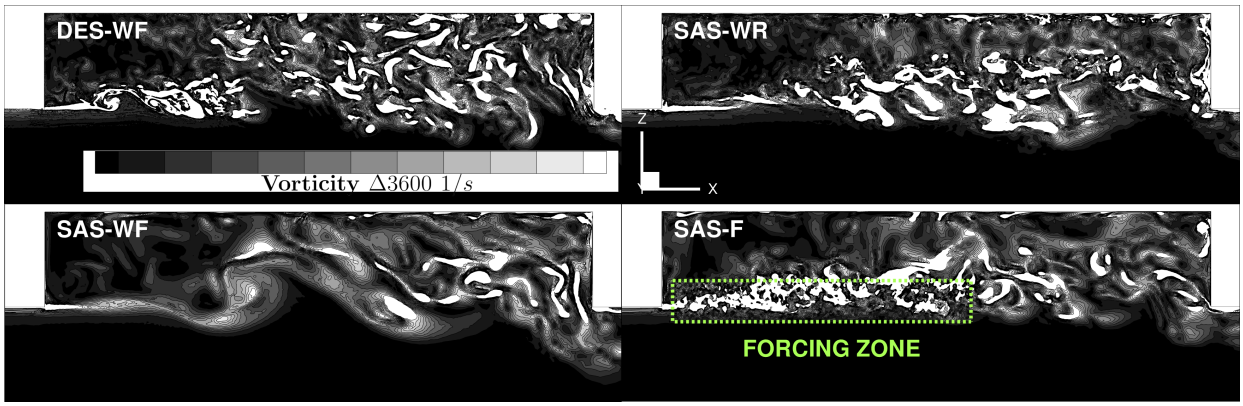

FIGURE 6.14: Instantaneous vorticity magnitude in $Ma_\infty = 0.8$ using DES-WF, SAS-WR, SAS-WF and SAS-F [110]

6.3.3 Prediction of the turbulent Flow Field

Fig. 6.14 shows the characteristics of open cavity flows captured by all the simulations. Vortices evolve in the shear layer and combine with other turbulent structures as they are convected downstream. Then, they break into smaller structures after impinging on the rear wall of the cavity. In SAS-F, the shear layer breaks down sooner, leading to a vortex-shedding process due to the applied artificial forcing technique, an improvement compared to the SAS-WF simulation. The flow structures shed from the front edge and grow in size without abrupt changes outside the forcing zone as they move toward the rear edge. Fig. 6.14 also shows the turbulence-resolving capability inside the cavity from the DES-WF, SAS-WR, SAS-WF and SAS-F simulations. One can see the acceptable flow field resolution from the DES-WF simulation, which is used as a reference to investigate the capability of the other turbulence models. The SAS variants clearly do not show all of the resolved scales seen in the DES-WF simulation since the scale-resolving ability of the SAS model only becomes active when there are enough fluctuations. Therefore, the structures are resolved in the shear layer and near the rear wall, where the shear layer impinges and flows upstream. The fine-scale structures are less pronounced in the SAS-WF simulation than in the SAS-WR simulation. The wall functions upstream of the wall do not produce resolved structures, leading to visible differences. By enforcing fluctuations in the SAS-F simulation, one can see a better prediction of the vorticity field in the shear layer, which is closer to the DES-WF results.

The effect of the forcing term on the resolved turbulence in the SAS approach is also visualized in Fig. 6.15. The profile of the resolved Reynolds stress from the DES-WF simulation appears as a triangular region starting from the lip with the base of the cone at the rear wall. The SAS-WR and SAS-WF simulations show the triangle's apex delayed

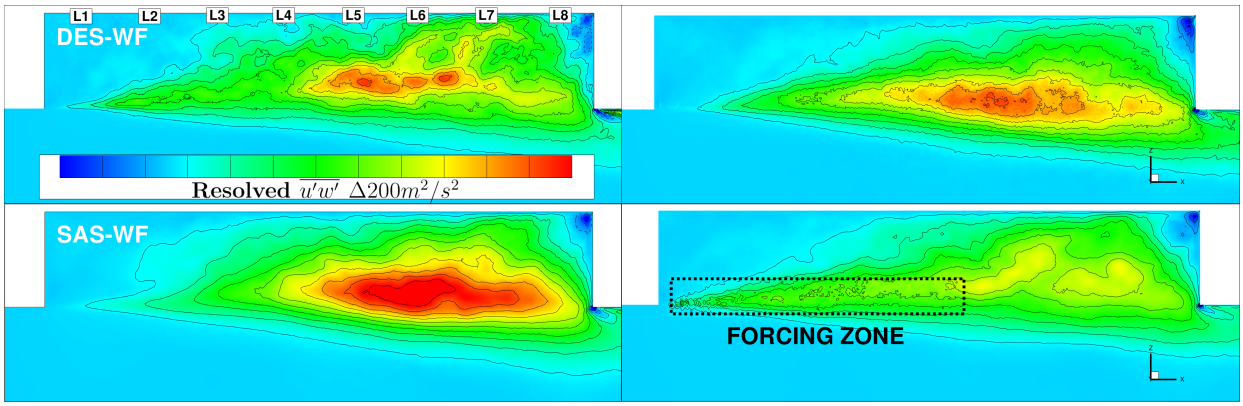

FIGURE 6.15: Distribution of the Reynolds stress $\overline{u'w'}$ in $Ma_\infty = 0.8$ using DES-WF, SAS-WR, SAS-WF and SAS-F [110]

and extending less upstream than in the DES-WF simulation. Activation of the forced fluctuation results in converting the model into resolved turbulent kinetic energy, and, eventually, this aids in predicting the resolved fluctuations near the lip of the cavity as well as the DES-WF simulation. Moreover, as a consequence of this process, one can see the profiles of the Reynolds stress components downstream of the forcing zone closer to those of the DES-WF simulation.

6.3.4 Investigation of Q_{SAS} and boundary-layer thicknesses

The contribution of Q_{SAS} has been studied to investigate the differences between the SAS variants further. The only difference between the SAS-WR and SAS-WF (or SAS-F) meshes is the number of prism layers close to the wall. The SAS-WR mesh has 35 prism layers with a y^+ value less than 1.0 for the first element, whereas the SAS-WF mesh has ten prism layers with a y^+ value greater than 100. It is noteworthy to investigate the source term of the SAS model, Q_{SAS}, present in the different SAS variants. The Q_{SAS} represents a critical element of triggering the model to allow the generation of resolved turbulence in SAS simulations. As seen in Fig. 6.16, Q_{SAS} is generated strongly over a larger region in the SAS-WR simulation, whereas, in the SAS-WF simulation, the region of Q_{SAS} presence is limited. The most significant difference appears near the upstream wall of the cavity. The usage of wall functions has rendered the SAS model to operate in URANS mode near the upstream wall of the cavity, which has led to the differences in the resolved structures inside the cavity. By contrast, the SAS-F model operates in resolving mode close to the front edge of the cavity due to forcing-induced structures, which leads to a better prediction of the shear-layer growth and its breakdown. Since the boundary-layer flow upstream of the cavity is crucial in cavity flows, it has been analyzed at a distance $0.1L_c$ upstream of

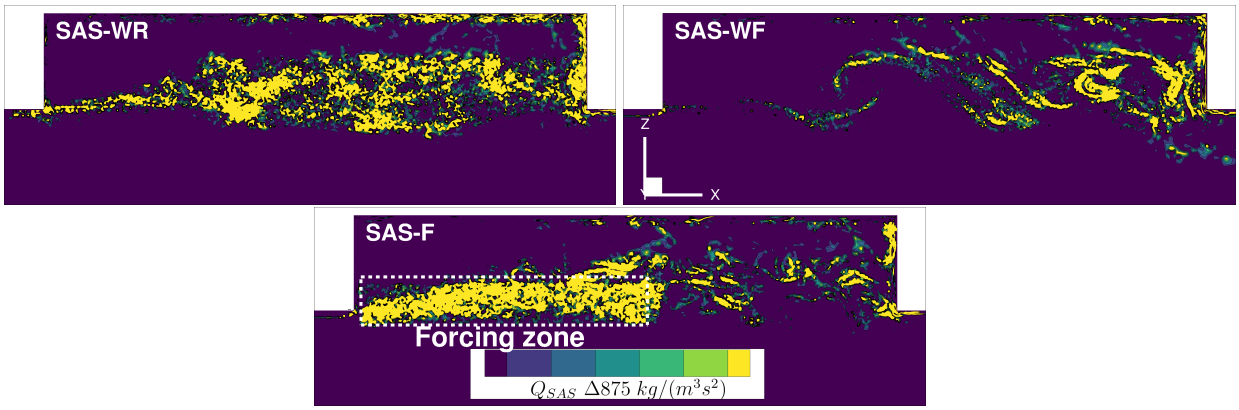

FIGURE 6.16: Source term Q_{SAS} in $Ma_\infty = 0.8$ using SAS-WR, SAS-WF and SAS-F [110]

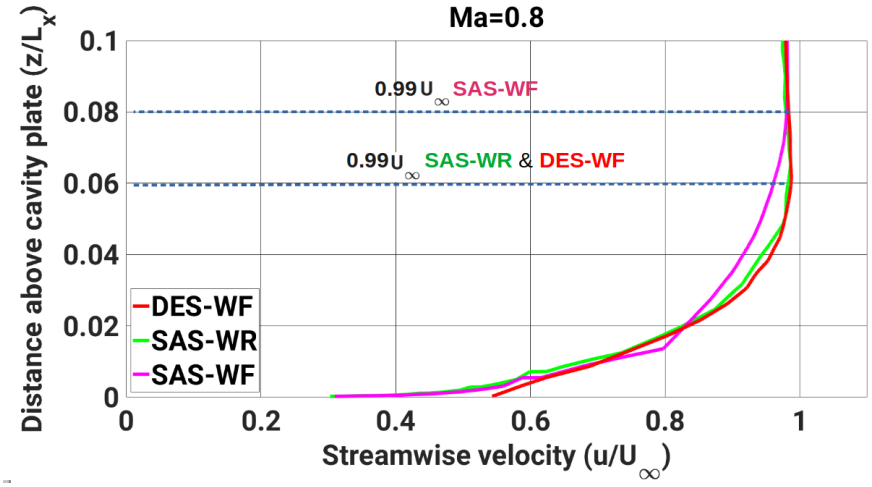

FIGURE 6.17: Asymptotic near-wall profile (99% U_∞) at a distance $0.1L_c$ upstream of the cavity at plane $y = 0$ in $Ma_\infty = 0.8$ using DES-WF, SAS-WR and SAS-WF [110]

the cavity, and the shape factor (i.e., the ratio of displacement to momentum thickness) has been determined as 1.24 in the case of DES-WF simulation, with the local Reynolds number, $Re_x = 2.8 \times 10^6$. The 99% thickness for the DES-WF reference case has been found to be 0.06 L_x, which coincides with the SAS-WR prediction, with L_x representing the distance of the local point from the leading edge of the cavity rig. Relative to the DES-WF case, there is an overprediction of $5 - 10\%$ in the displacement and momentum thicknesses in the SAS-WR simulation. The SAS-WF and SAS-F simulations predicted 20% more in the thicknesses, showing deviations of the shape factor as low as 3%. In Fig. 6.17, the asymptotic near-wall flow profile at $0.1L_c$ distance upstream of the cavity has been shown. It is noticed that as a result of RANS behavior close to the wall without resolved structures, the thickness of the boundary layer based on the 99% U_∞ measure in

TABLE 6.3: Computational requirements relative to DES-WR [110] for $Ma_\infty = 0.8$

	DES-WF	**SAS-WR**	**SAS-WF**	**SAS-F**
Number of outer iterations per time step	200	200	200	200
Physical time step size	1.5×10^{-6}	7×10^{-6}	7×10^{-6}	7×10^{-6}
Drop in ρ residual within one time step	$\sim$O (10^2)	$\sim$O (10^2)	$\sim$O (10^2)	$\sim$O (10^2)
Comp. cost reduction relative to DES-WR	50%	90%	95%	95%

SAS-WF simulation is larger than the thickness predicted by the DES-WF and SAS-WR simulations. The boundary layer developed upstream of the cavity has an essential effect on the growth of the shear layer. Most, if not all, of the eddy viscosity contained in the boundary layer is transferred to the shear layer, making it more stable than in the DES-WF and SAS-WR simulations. As seen in the SAS-WR simulation, this thicker shear layer with higher turbulent energy content cannot break down sooner. The process of shear layer breakdown is thereby delayed, as the shear layer contains most of the energy-carrying eddies, and they do not dissipate enough energy. It leads to overprediction of energy levels inside the cavity, as seen in Fig. 6.12.

6.3.5 Computational Time Requirements

Tab. 6.3 shows the time step size and computational cost reduction relative to the wall-integrated SA-IDDES results (DES-WR). The number of outer iterations per time step has been set to 200, which ensures a reduction in the density residual by two orders of magnitude within a time step. It has been observed that time step size plays a major role in the improvement of computational efficiency within the SAS variants, which allows for a larger time step size due to the underlying RANS nature of the SAS model. The DES-WR and DES-WF simulations are stringent regarding the time step size, and a higher CFL number leads to the misprediction of spectral results.

6.4 Impact of Asymmetric Flow Conditions

A case of the sideslip study with $\beta = 8°$ was simulated in order to study the effect of asymmetric flow conditions on the presence of resonant modes. This subsection will show the modulation effect of the sideslip angles on the measured spectral modes, including the reliability of the SAS method under different flow conditions and the investigation of lateral wall effects on the cavity flow features. The flow under sideslip conditions

naturally involves more turbulent fluctuations than symmetric flow conditions, which aid in activating the SAS mode. Therefore, the SAS-WR approach is a sufficient method for the considered case. Since the forcing zone approach does not require additional interface treatment, one could also use the SAS-F method for sideslip conditions without special requirements for the case. It should be noted that the mesh created for the baseline case of $\beta = 0^\circ$, which was optimized for flow aligned with the cavity walls, is also used for the sideslip case. At $\beta = 8^\circ$, the change in flow direction may result in misalignment between the flow features (such as vortices, shear layers, and recirculation zones) and the mesh. This misalignment can affect the accuracy in capturing key flow characteristics, especially in regions with high gradients, such as near the cavity lips and along the shear layer. Additionally, the change in flow angle may cause cells to become skewed relative to the incoming flow, particularly near the leading edge of the cavity. While mesh adaptation techniques could be employed to mitigate these issues, the focus of this section is also to test the generality of the original mesh under varying flow conditions. Therefore, the mesh remains unchanged from that used for the straight flow case.

Fig. 6.18 shows the FFT spectrum of four probe locations along the cavity ceiling. The general shape of the spectra occurring in all the probe locations has been predicted to be in good agreement with the experimental data. The relative magnitudes between the modes have also been predicted well. Mode 2 has been slightly under-predicted by the simulation for all the probe locations. As the sideslip angle increases, the frequencies at which the resonant modes occur decrease, and the modal amplitudes increase, which is well captured by the simulation results. It has been shown in Section 6.3 that using wall functions leads to stronger vortices in the shear layer and subsequent overprediction of spectral amplitudes, although the spectral frequencies fit the experimental data well. It suggests that the resonant frequencies are correlated to the interaction time scale between the aerodynamic disturbances from the shear layer and upstream-traveling acoustic waves. This interaction time scale is a direct consequence of the cavity length, as seen in the Rossiter model for frequency estimation (Eq. 2.1). As the sideslip angle increases, the interaction time scale between them also increases due to the skewed shear-layer flow inside the cavity, and the frequencies at which the peaks occur decrease.

In addition to the flow structures shed from the front edge of the cavity, there are additional structures from the edge of the windward-side door added to the shear layer marked by the dashed circle in Fig. 6.19(a). The structures merge, and they enlarge in size while being convected in the shear layer before impinging on the end of the leeward-side door and the rear wall of the cavity. On impingement, the flow is redirected spanwise, flows upstream and interacts with the oncoming shear layer. The spanwise recirculation can be seen with

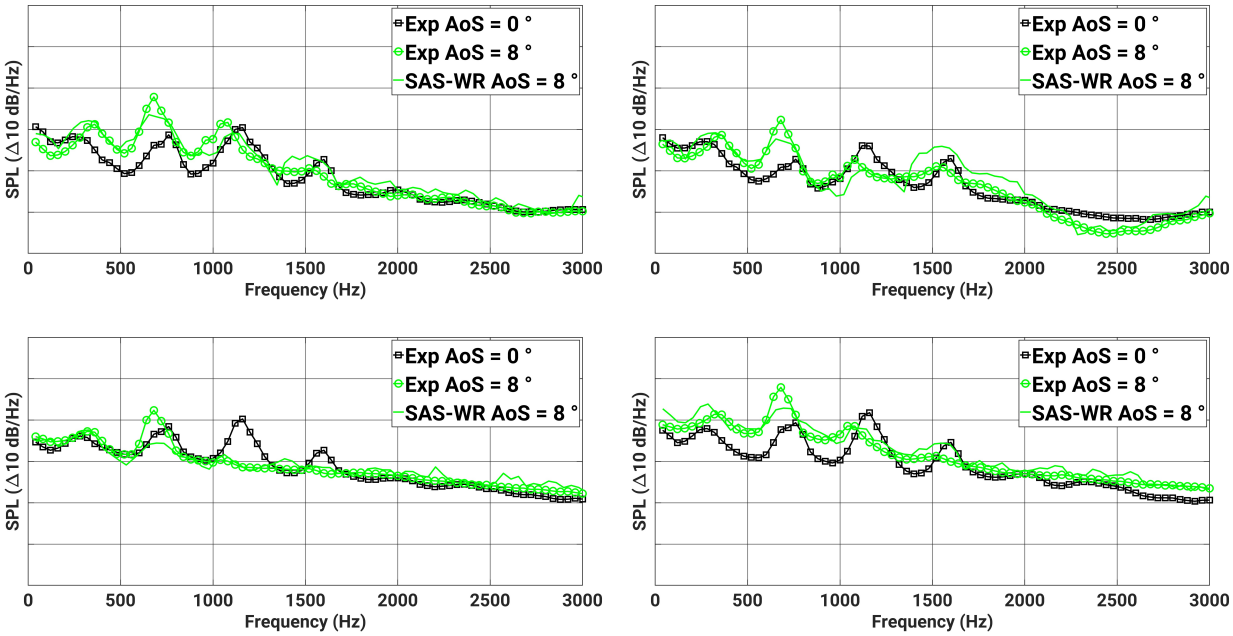

FIGURE 6.18: Measurement data and SPL predictions by SAS-WR at L1, L2, L7 and L8 (from top left to right bottom) at $Ma_\infty = 0.8$ with $AoS = 0°$ and $AoS = 8°$[110]

the negative u-velocity marked with dotted lines in Fig. 6.19(b). The activation of the resolving mode in the model is presented in Fig. 6.19(c), which shows the distribution of the SAS source term Q_{SAS}. In the regions of higher values, the eddy viscosity is reduced, and subsequently, the turbulence is resolved down to the underlying cell size.

The amplitudes of the first four resonance modes were determined, and their isosurfaces are shown in Fig. 6.20 to identify the nature of the modes. It is observed that there is a dominant longitudinal propagation of waves inside the cavity. In addition, there is a contribution from spanwise propagating waves in the higher modes. Basically, mode 1 is governed by the bulk flow processes in the cavity, namely the shear layer and the recirculation process. It is to be noted that the shear layer is skewed due to the presence of the windward door. The resonance between these two large-scale mechanisms correlates to mode 1 in the cavity. The contribution of skewed components of the shear layer decreases as the mode number increases. Higher modes 2, 3 and 4 comprise gradually less skewed shear-layer components that encounter the leeward wall, leading to spanwise standing waves. Furthermore, in the streamwise direction, more nodes with shorter wavelengths exist with an increasing mode number, or the wavenumber of the modes becomes smaller with an increasing mode number. To summarize, mode 1 encompasses the large-scale skewed dynamics of the shear layer. In contrast, the higher modes correlate

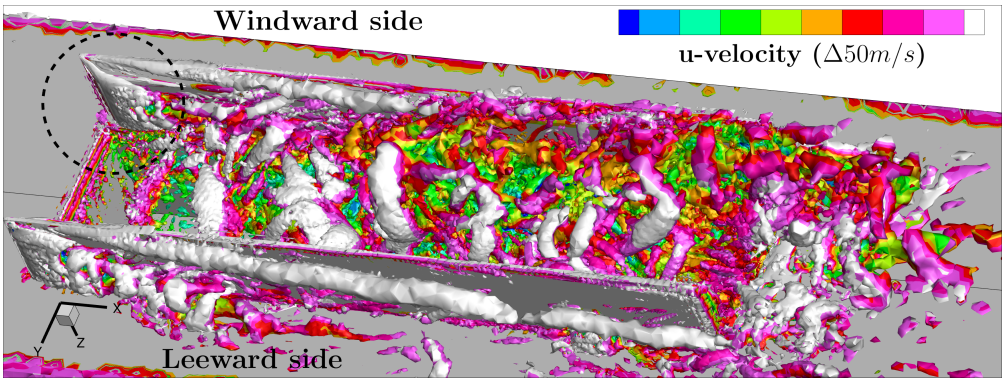

(a) Flow structures observed through Q-criterion coloured by streamwise velocity

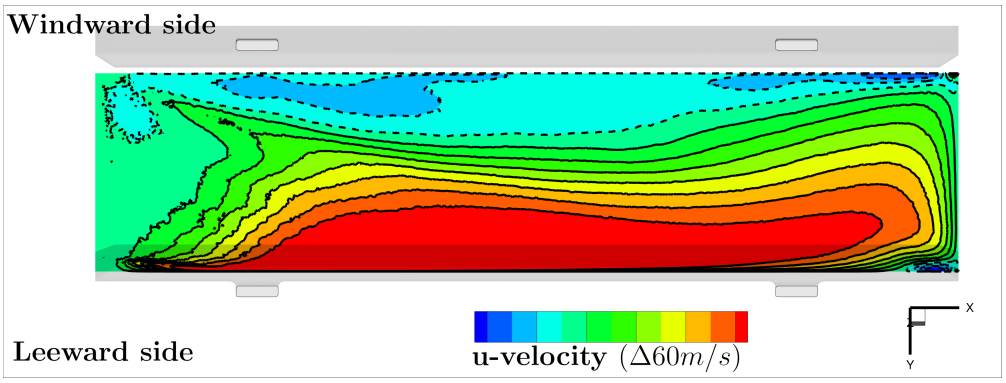

(b) Mean streamwise velocity in plane $Z = 0.1\ D_c$

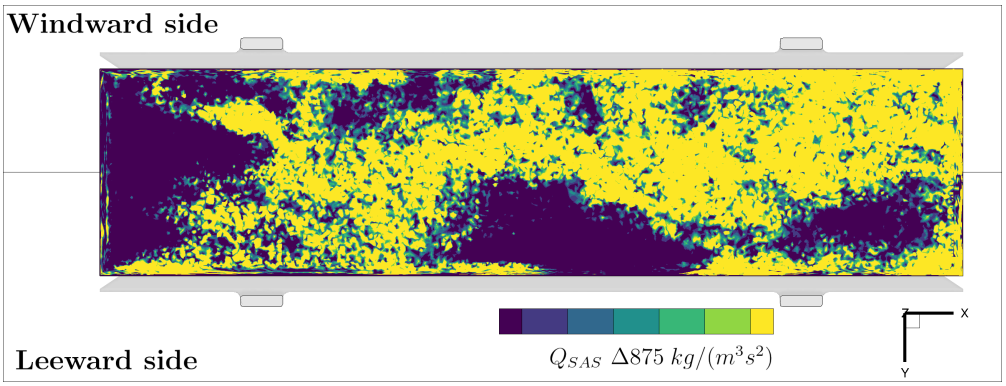

(c) Contribution of Q_{SAS} in plane $Z = 0.1\ D_c$

FIGURE 6.19: Flow visualization at $Ma_\infty = 0.8$ with $AoS = 8°$ using SAS-WR [110]

to the shedding flow structures from the unskewed parts of the shear layer and have a contribution from spanwise components initiated by the flow interaction on the leeward side. This contribution results in an increase in modal amplitudes for asymmetric flow conditions.

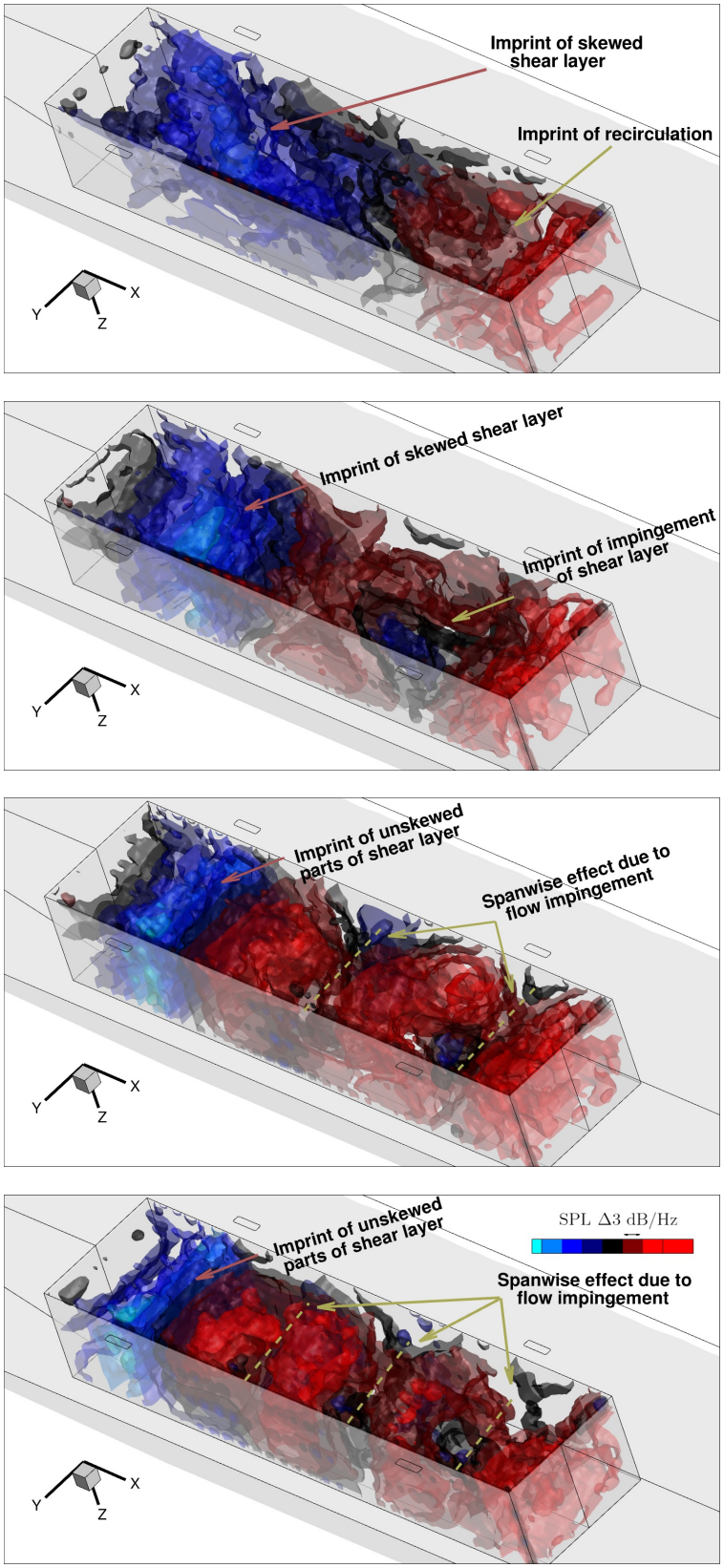

FIGURE 6.20: Visualization of modes at $Ma_\infty = 0.8$ with $AoS = 8°$ using SAS-WR observed through iso-surfaces of modes [110]

Chapter 7

Results of leading-edge vortex on delta wings

The flow conditions are characterized by $Ma_\infty = 0.85$ and $Re_\infty = 12.53 \times 10^6$, along with a side slip angle of $\beta = 5°$. The reader is directed to the work by Di Fabbio et al. [81], which examines the simulation of the DW2 planform using various turbulence models, comparing their performance across different chord-wise locations and local surface pressure distributions. The study highlights the effectiveness of models like $k - \omega$ SST and SAS in predicting aerodynamic coefficients compared to RANS models such as SA-negRC. Building upon the insights gained from the modelling endeavors in the study, this chapter explores the underlying physical dynamics within the flow fields, particularly emphasizing vortex and shock behaviour and their transient characteristics, responsible for the observed local surface pressure. The chapter is organized in that section 7.1 discusses the efficacy of simulation methods in terms of aerodynamic coefficients of both the planforms, followed by preliminary visualizations of the flow field in section 7.2. Subsequently, section 7.3 delves into physical phenomena such as shock-vortex interaction, vortex-vortex interaction, and shock-buffet observed in the delta-wing planforms DW1 and DW2. Section 7.4 analyses the flow fields based on the entrophy transport equation, which is then followed by detailed investigation of shock buffet at $\alpha = 20°$ in section 7.5.

7.1 Performance of simulation methods

The computations have been performed for various incidence angles, as shown in Fig. 7.1. The lift coefficients are well-predicted for both planforms. However, the simulation for the DW2 planform does not predict the drop in lift by 18% between $\alpha = 20°$ and $\alpha = 24°$. Due to the asymmetric flow and vortex breakdown at high incidence angles, the

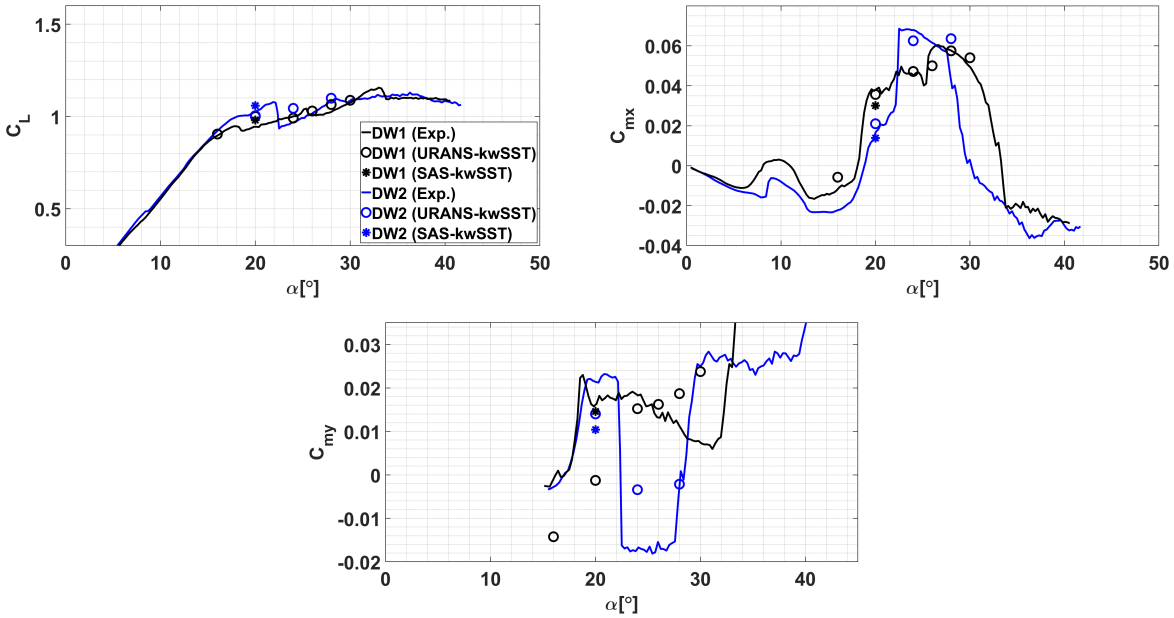

FIGURE 7.1: Aerodynamic coefficients of DW1 and DW2 - Experiment and simulation models, namely the $k-\omega$ SST and SAS model at $Ma_\infty = 0.85$ and $Re = 12.53 \times 10^6$ with $AoS = 5°$

moment coefficients exhibit more significant variations than the lift coefficient, making it challenging to discuss them to validate the simulation results.

The rolling moment plot demonstrates the accuracy of the simulation results for both planforms, which is in good agreement with the measurement data. Notably, the prediction for the DW1 planform is highly accurate. The simulation captures an increase of approximately 1.3 times the coefficient in DW2. The simulation results capture the general trend of the pitching moment, although the absolute values slightly differ from the experimental data.

At $\alpha = 20°$, both planforms show significant differences in the aerodynamic characteristics due to shock and vortex breakdown. Therefore, this specific case has been analysed in detail with SAS. It is important to note that, in general, SAS results at these incidence angles exhibit better accuracy compared to the $k-\omega$ SST model for both planforms.

7.2 Visualization of the vortex system

The vortex system in the planforms has been discerned using the Q-Criterion, which serves as the second invariant of $\frac{\partial u_i}{\partial x_j}$. It identifies vortices by prioritizing the vorticity magnitude

over the strain-rate magnitude [122]. Mathematically, it is expressed as

$$Q = \frac{1}{2}\left(\|\Omega\|^2 - \|S\|^2\right) > 0\,. \tag{7.1}$$

Here, Ω represents the vorticity tensor, derived as the anti-symmetric part of $\frac{\partial u_i}{\partial x_j}$, and the strain-rate tensor S_{ij} represents the symmetric part

$$\Omega_{ij} = \frac{1}{2}\left(\frac{\partial u_i}{\partial x_j} - \frac{\partial u_j}{\partial x_i}\right) \tag{7.2}$$

$$S_{ij} = \frac{1}{2}\left(\frac{\partial u_i}{\partial x_j} + \frac{\partial u_j}{\partial x_i}\right)\,. \tag{7.3}$$

Fig. 7.2 offers a detailed insight into the flow fields of DW1 and DW2, presenting transparent slices showcasing Q at varying angles of attack: 16° and 20°. At $\alpha = 16°$ in DW1, the inboard vortex (IBV) originates on both sides of the wing from the highly-swept leading-edge section and progresses downstream. The IBV's trajectory straightens and diverges from the leading edge as the wing transitions to the medium-swept section. Concurrently, the shear layer separates from the medium-swept leading edge, forming an additional leading-edge vortex known as the midboard vortex (MBV). Both the IBV and MBV interact downstream, moving towards the trailing edge. In DW2, IBVs on either side develop from the levcon and highly-swept leading edge. Generally, on the windward side, the fusion of the outboard vortex (OBV) with the MBV results in the MBV's dissolution, while on the leeward side, MBVs and OBVs interact and strengthen. At $\alpha = 20°$ in DW1, both windward and leeward IBVs enlarge compared to their counterparts at $\alpha = 16°$. On the windward side, the MBV exhibits significant spanwise motion, eventually rolling over the IBV, whereas on the leeward side, the MBV interacts with the IBV, supporting its existence. Notably, the windward IBV experiences breakdown, indicated by black dotted lines. In DW2, the IBV expands considerably upstream compared to DW1 due to shocks generated by the kink in its triple-delta wing planform. As a result of the IBV's burst, the subsequent MBV is diverted, preventing it from rolling over the IBV as observed in DW1. Generally, on the windward side, the MBV surpasses the IBV without interaction, while on the leeward side, the MBV interacts with the IBV, forming a stronger vortex system. The interaction between MBVs and outboard vortices OBVs is more noticeable at low-incidence angles. Conversely, the interaction between MBVs and inboard vortices (IBVs) becomes more pronounced at high-incidence angles.

Fig. 7.3 showcases the vortex system at higher angles of attack, specifically 24° and 28°. At $\alpha = 24°$ in DW1, the windward IBV experiences upstream breakdown compared to the

20° case, with no presence of MBV and OBV observed, while the leeward MBV rises and expands in diameter. The OBV merges and interacts downstream with the IBV. No vortex is generated in DW2 on the windward side. Generally, a distinct unwrapping pattern becomes evident in the vortices, accompanied by increased vortex-core diameter as the incidence angle rises. Moreover, vortices produced over the main wing (MBV and OBVs) show diminishing presence in these high-incidence cases. Additionally, the flow field reveals the formation of two prominent fuselage vortices, particularly at 20°, 24°, and 28°.

Distribution of mean-C_p Development of vortex system in DW1 and DW2 discussed in section 7.2 create suction pressure on their planforms, which helps in inducing additional lift and moments. The mean-C_p coefficient at different incidence angles is presented in Fig. 7.4. At $\alpha = 16°$, the suction footprint of both DW1 and DW2 look similar, with the additional suction pressure region present over levcon in DW2. The formation of IBV is fundamentally different between the planforms, which as a result, DW2 could show a lesser suction effect than DW1. At $\alpha = 20°$, on the windward side, the suction footprints significantly differ between DW1 and DW2 due to their difference in the vortex breakdown characteristics, the cause of which will be discussed in section 7.3. DW1 shows a longer suction profile compared to DW2. The suction effect due to the levcon surface is higher on either side of the wings in $\alpha = 20°$ compared to $\alpha = 16°$. Moreover, on the leeward side, the merged IBV and MBV create a higher suction pressure in $\alpha = 20°$ compared to $\alpha = 16°$ in DW1 and DW2 due to increase in vortex diameter as seen in Fig. 7.2. At $\alpha = 24°$ and $\alpha = 28°$, DW1 displays a shortened suction footprint on the windward side compared to lower incidence ranges due to the upstream presence of shock (see section 7.3), whereas DW2 shows no suction pressure distribution on the windward side due to no production of vortices as seen in Fig. 7.3. Reader is directed to the study conducted by Di Fabbio et al. [81] for a comprehensive comparison of surface mean-C_p values predicted by various turbulence models, including the $k - \omega$ SST and SAS models, against pressure-sensitive paint (PSP) measurement data.

Formation of secondary vortices Strength of IBV affects the generation of secondary vortices, which are formed outboard and underneath the IBV. At $\alpha = 16°$, the IBV of DW1 exhibits twice the mach number compared to DW2 as presented in Fig. 7.5, which shows 10 equidistant chord-wise slices. However, the levcon part of DW2 shows higher axial velocity, which then drops considerably when the shear layer from the strake region feeds and eventually forms an unstable IBV. The $\alpha = 16°$ case shows, in general, a "well-organized" IBV generation in DW1 compared to DW2. The IBV leads to a secondary vortex

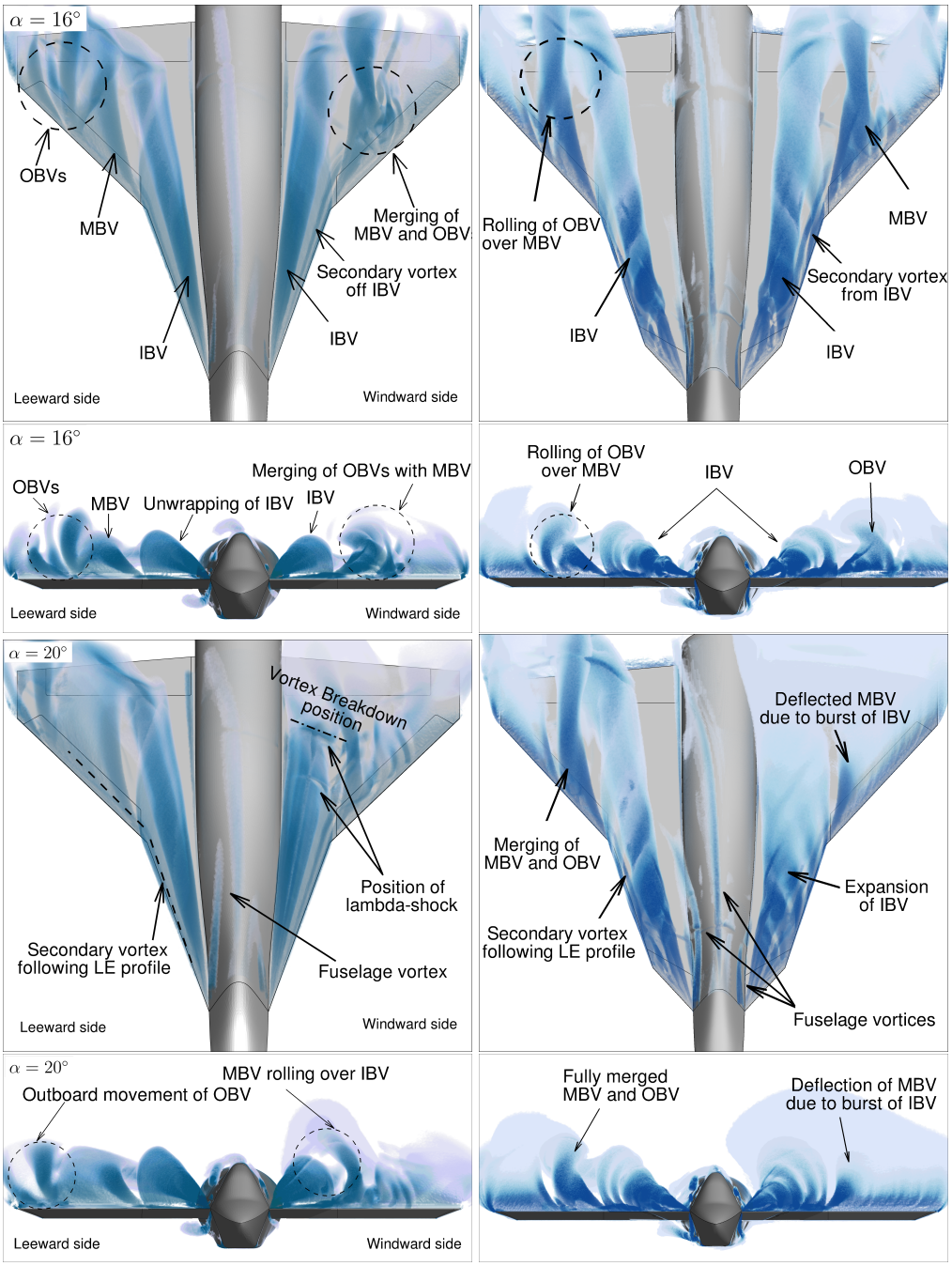

FIGURE 7.2: Vortex system at $\alpha = 16^\circ$ and 20° observed through volume visualization of Q in DW1 (left) and DW2 (right) at $Ma_\infty = 0.85$ and $Re = 12.53 \times 10^6$ with $AoS = 5^\circ$ using $k - \omega$ SST model

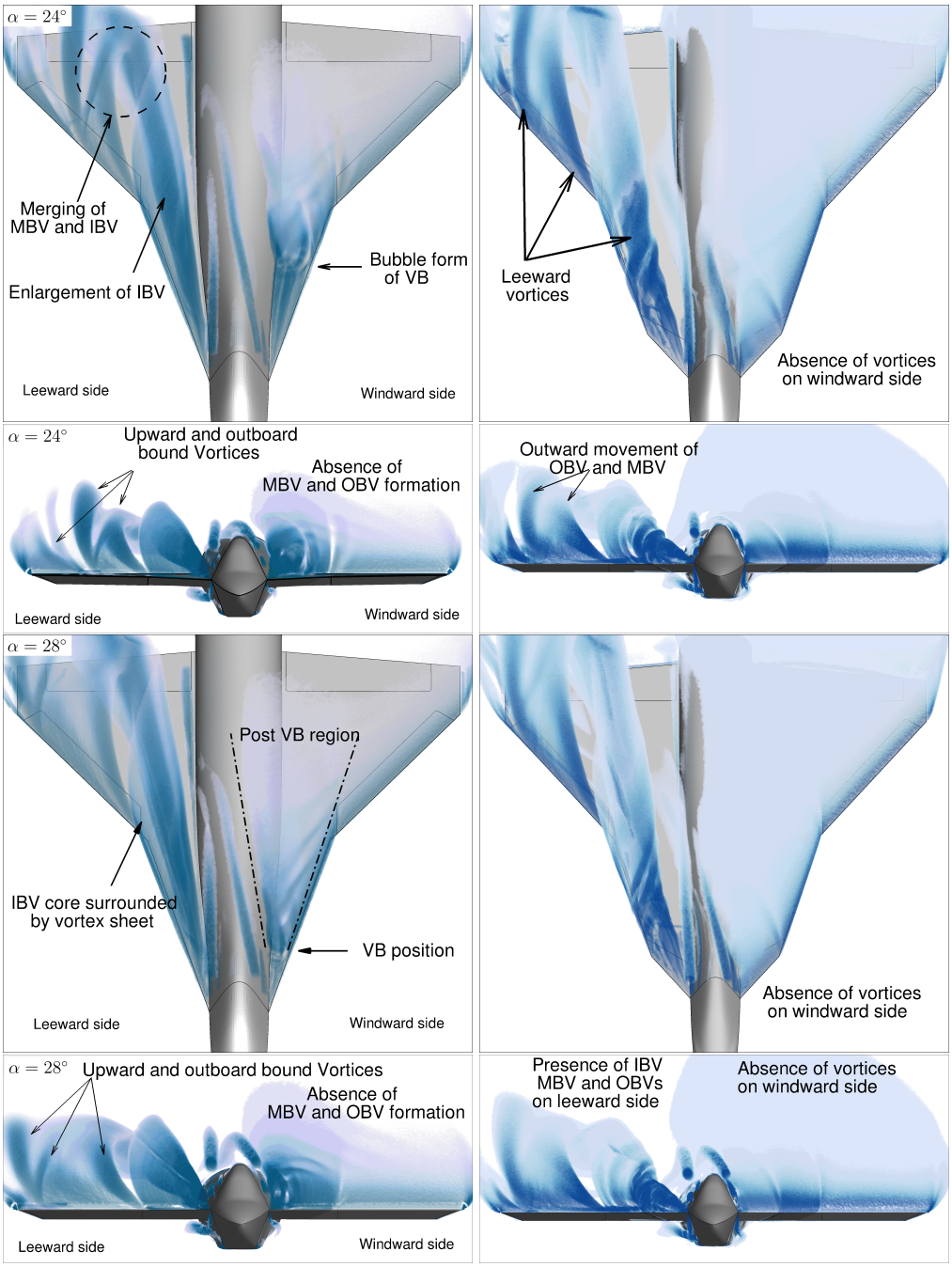

FIGURE 7.3: Vortex system at $\alpha = 24°$ and $28°$ observed through volume visualization of Q in DW1 (left) and DW2 (right) at $Ma_\infty = 0.85$ and $Re_\infty = 12.53 \times 10^6$ with $AoS = 5°$ using $k - \omega$ SST model

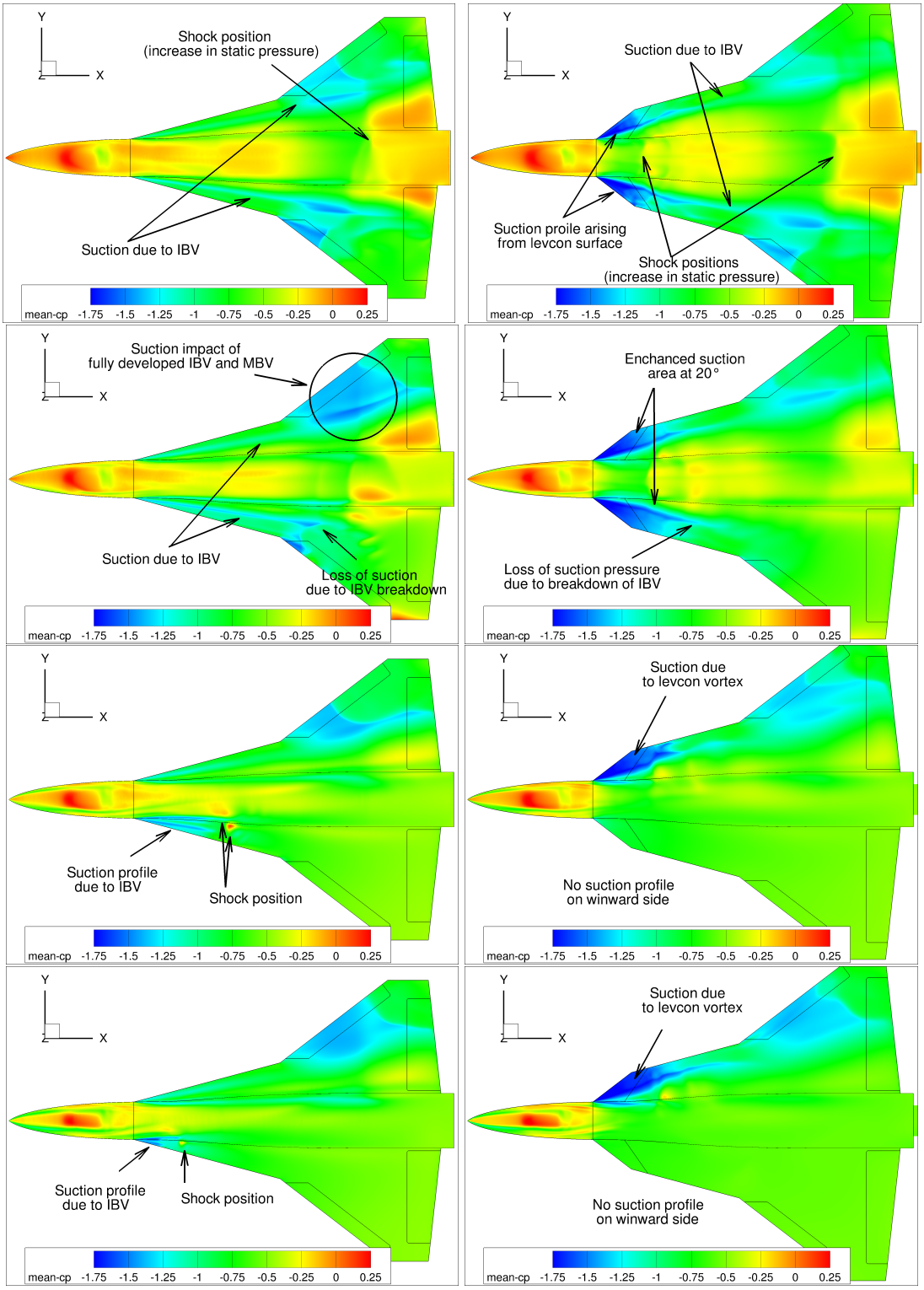

FIGURE 7.4: Mean-Cp at $\alpha = 16°, 20°, 24°$ and $28°$ from top to bottom in DW1 (left) and DW2 (right) at $Ma_\infty = 0.85$ and $Re_\infty = 12.53 \times 10^6$ with $AoS = 5°$ using $k - \omega$ SST model

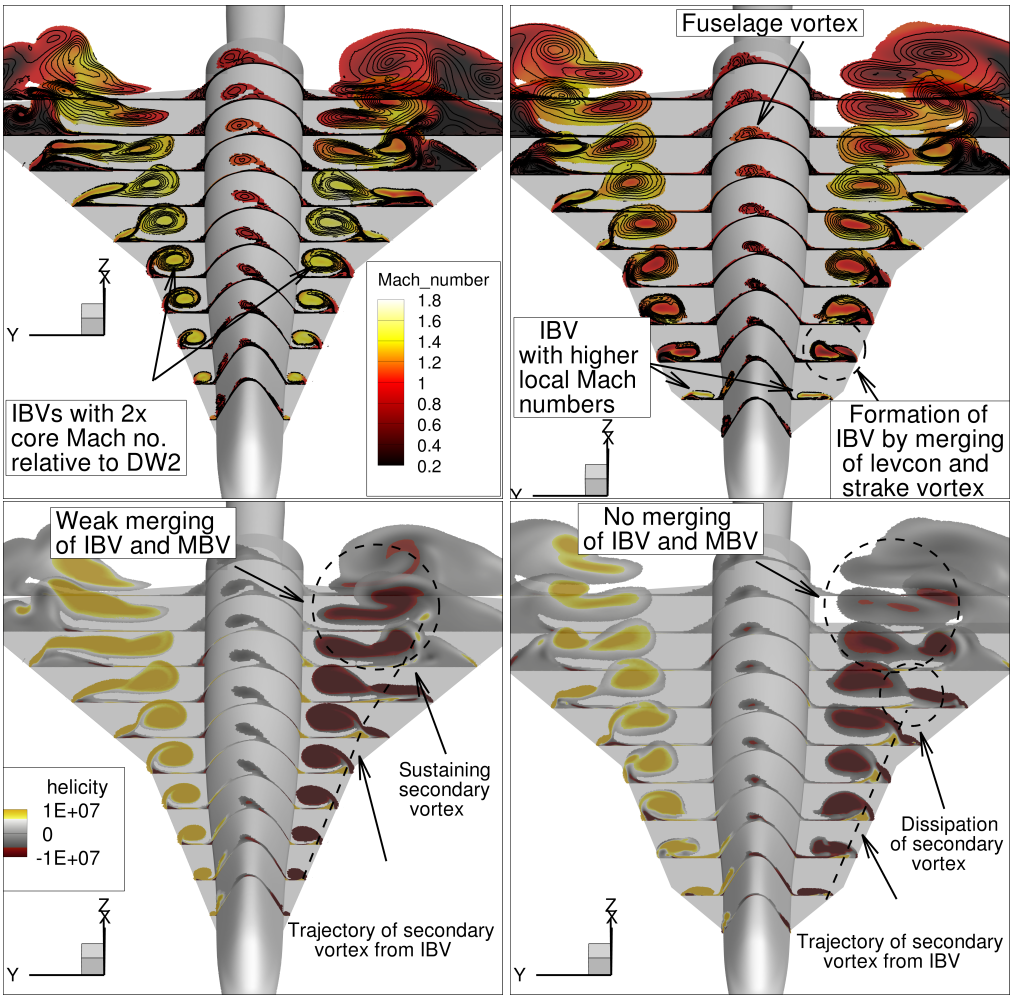

FIGURE 7.5: Mach number and helicity at $\alpha = 16^\circ$ in DW1 (left) and DW2 (right) at $Ma_\infty = 0.85$ and $Re_\infty = 12.53 \times 10^6$ with $AoS = 5^\circ$ using $k - \omega$ SST model

outboard on both sides of the wings. The trajectory of the secondary vortex is marked by a dotted line in Fig. 7.5. The secondary vortex sustains longer in DW1 than DW2 due to stronger IBV in DW1, where it dissipates after the primary vortex is stopped to be fed by the leading-edge shear layer. In general, the continued feeding of the shear layer to the IBV and the proximity of IBV and MBV sustain the secondary vortex. Meanwhile, weak IBV and the far proximity of the vortices could not sustain the secondary vortex and dissipate quickly, as seen in DW2.

7.3 Investigation of shock-vortex interaction

As the freestream conditions are transonic, local supersonic regions are produced over the wing, which affects the vortex system. The occurrence of shocks at different incidence angles in DW1 and DW2 are presented in Fig. 7.6. In DW1, at $\alpha = 16°$, normal shocks are present in the rear section of the wing. The shock is seen to be interacting with the vortex system, which does not show any breakdown. In the case of DW2, two normal shocks are produced due to planforms, one in the front portion of the wing caused by the kink in the planform and the other in the rear portion of the wing. In the shock near the front portion, the shock protrudes in the front are marked in white dotted circles due to the higher local vorticity and axial velocity in the vortex core. Despite the interaction with the shock, the vortex systems in DW2 could also show a sustained presence over the wing without any breakdown pattern. At $\alpha = 20°$, both the planforms show a fundamental change in the cause of their respective vortex system. DW1 shows a transient case of IBV interacting with the shock, causing its buffet and eventual breakdown of IBV, which will be discussed in section 7.5. In DW2, the stationary kink-induced shock at the front part of the wing causes the breakdown of windward-IBV. At $\alpha = 24°$, DW1 shows shocks are present more upstream relative to $\alpha = 20°$. Meanwhile, in DW2, there is no shock on the windward side due to the local subsonic regime, and shock is present only on the leeward side. At $\alpha = 28°$, the shock system is more or less similar to the $\alpha = 24°$ case with a slight upstream location of the shocks and VB's position.

Variations in Shock strength For incompressible flows, at very low incidence angles, the vortex-vortex interaction is weak, and an increase of the incidence angle makes the interaction stronger before it becomes unstable at very high angles of attack [67]. As the angle of attack increases, the vortex starts to break down because of the stronger adverse pressure behind its core. As the angle of attack keeps getting higher, the point where this breakdown happens moves further towards the front of the wing as shown in Fig. 7.2. In transonic flow conditions, the flow field shows sudden changes due to the presence of the shock. Moreover, the interactions of the two vortices depend not only

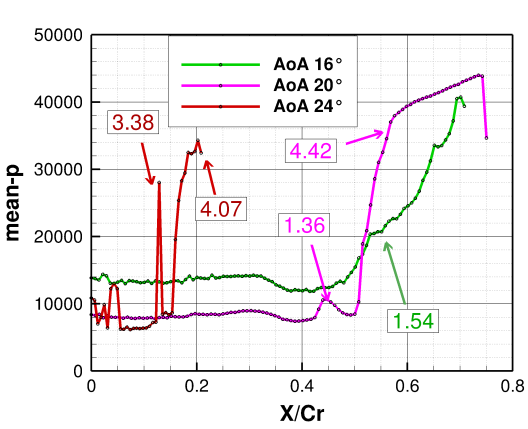

FIGURE 7.7: Pressure ratio through IBV core for $\alpha = 16°, 20°$ and $24°$ in DW1 at $Ma_\infty = 0.85$ and $Re_\infty = 12.53 \times 10^6$ with $AoS = 5°$ using $k - \omega$ SST model

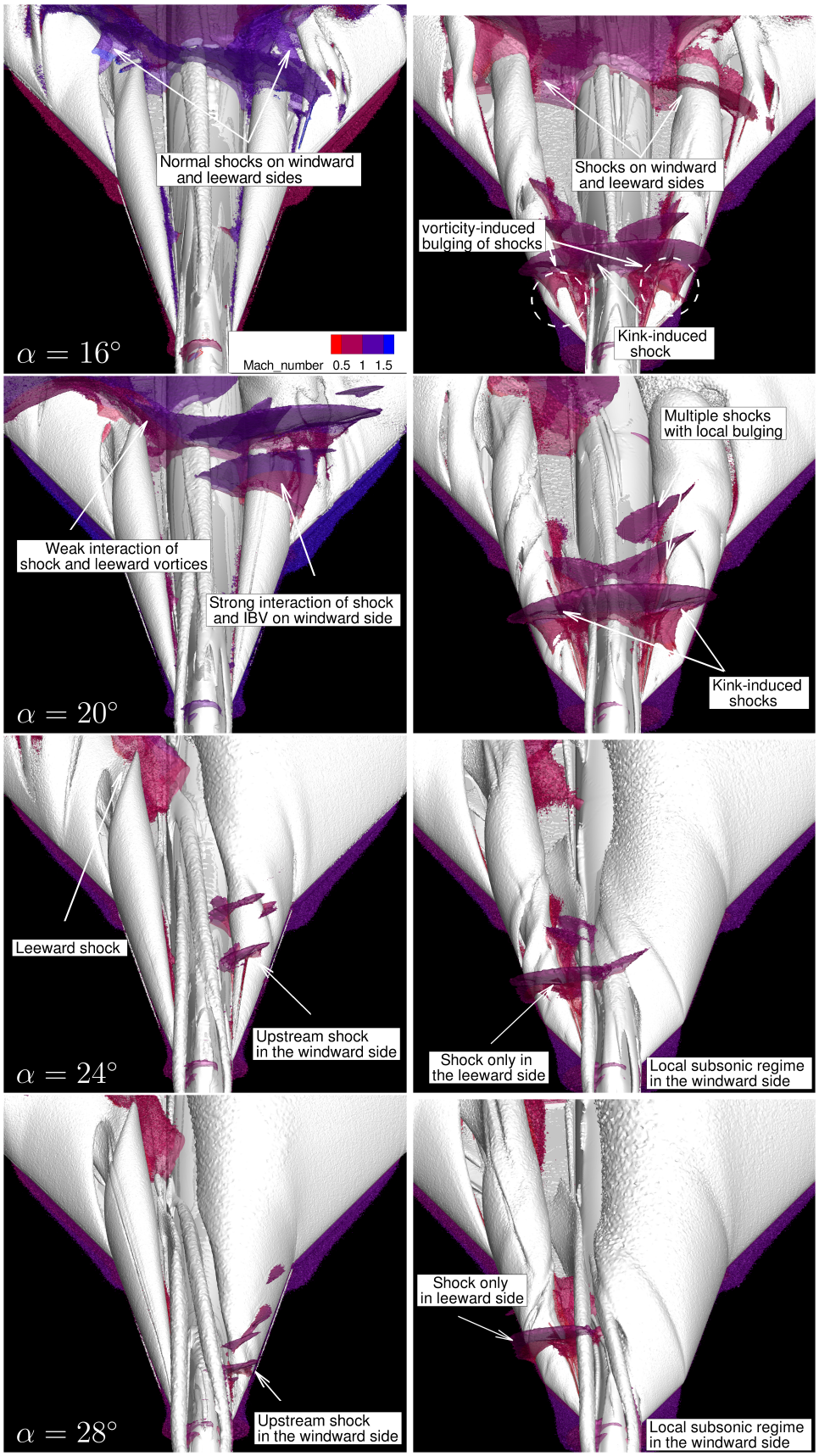

FIGURE 7.6: Vortex-shock interaction at $\alpha = 16°, 20°, 24°$ and $28°$ from top to bottom observed by iso-surfaces $\partial\rho/\partial x$ and $Q - Criterion$ and coloured by Ma in DW1 (left) and DW2 (right) at $Ma_\infty = 0.85$ and $Re_\infty = 12.53 \times 10^6$ with $AoS = 5°$ using $k - \omega$ SST model

on the state of the vortices but also on the position and orientation of the shocks in the transonic case. At an angle of $\alpha = 20^\circ$ and $\alpha = 24^\circ$, the vortex-breakdown point shifts further upstream compared to the $\alpha = 16^\circ$ case. Fig. 7.7 shows the pressure ratio through the vortex-core for the angle of incidences 16°, 20° and 24°, where the values in text box represent pressure ratio through the shock. The study has considered the shock strength based on the pressure ratio, and it is observed that as the Mach number increases, the pressure ratio jumps across the shock waves increase.

Criteria for vortex breakdown In an extensive examination conducted by Deléry [57], the study illustrates the relevance of various parameters in the context of vortex breakdown caused by the interaction of shockwaves and vortices. These parameters include the swirl and axial velocities of the vortex core. Deléry [57] suggests that the swirl ratio or the Rossby number could indicate the vortex's intensity and, consequently, its susceptibility to shock-induced breakdown. The Rossby number, a dimensionless parameter, is the axial to circumferential momentum ratio within a vortex. This investigation employs both the maximum axial velocity at the vortex core, denoted as U_{axial}, and the simplified maximum in-plane y-velocity, denoted as U_{Ymax}, of the vortex. The relation defines the Rossby number:

$$Ro = \frac{U_{axial}}{U_{Ymax}} \tag{7.4}$$

When a vortex encounters a normal shock, the swirl velocity remains relatively constant while the axial velocity decreases, decreasing the Rossby number [123]. It corresponds to an increase in vortex intensity, consequently raising the susceptibility of the vortex to breakdown. Researchers, such as Spall et al. [124], and Robinson et al. [125], have explored using the Rossby number as a criterion for breakdown. They have applied this criterion to computational data from flow around slender delta wings and found that the critical Rossby number falls between 0.9 and 1.4 in most cases. A stable vortex core is typically observed for Rossby numbers above 1.4. The Rossby number was computed to address this specific criterion. Fig. 7.8 shows the distribution of Rossby numbers for the IBV in DW1 and DW2. On the leeward side, where the shock has a comparatively weak influence on axial velocity, the Rossby number remains at elevated levels, indicating a stable range. Consequently, the vortex displays a relatively low susceptibility to disturbances. In contrast, the shock system significantly affects axial velocity on the windward side, resulting in a pronounced reduction of the Rossby number. It, in turn, amplifies the susceptibility of the vortex to breakdown.

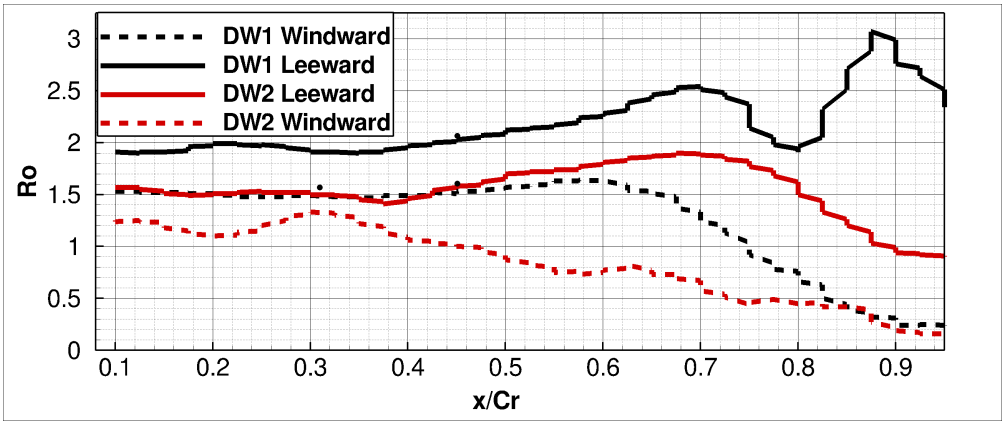

FIGURE 7.8: Rossby number of IBV in DW1 and DW2 at $\alpha = 20^\circ$ at $Ma_\infty = 0.85$ and $Re_\infty = 12.53 \times 10^6$ with $AoS = 5^\circ$ using $k-\omega$ SST model

7.4 Enstrophy transport equation

Eq. 7.5 represents the vorticity transport equation for the RANS averaged velocities, illustrating the evolution of vorticity within a fluid flow. This equation is derived from the modelled momentum equation and features effective viscosities. It showcases various contributing factors influencing the vorticity field and consequent alterations in the velocity field.

$$\frac{\partial \omega_i}{\partial t} + u_k \frac{\partial \omega_i}{\partial x_k} = \omega_k \frac{\partial u_i}{\partial x_k} - \epsilon_{ijk} \frac{1}{\rho^2} \frac{\partial \rho}{\partial x_j} \frac{\partial \tau_{kl}}{\partial x_l} + \frac{\epsilon_{ijk}}{\rho} \frac{\partial^2 \tau_{kl}}{\partial x_j x_l} - \omega_i \frac{\partial u_k}{\partial x_k} + \frac{\epsilon_{ijk}}{\rho^2} \frac{\partial \rho}{\partial x_j} \frac{\partial p}{\partial x_k} \tag{7.5}$$

In order to analyze the impact of different mechanisms on the strength of the vorticity field and its influence on velocity changes, the enstrophy equation is derived from the vorticity transport equation. The enstrophy equation, derived by multiplying both sides of the vorticity transport equation by vorticity ω_i, is expressed as follows [126]:

$$\frac{\partial \Omega}{\partial t} + u_k \frac{\partial \Omega}{\partial x_k} = \underbrace{\omega_i \omega_k \frac{\partial u_i}{\partial x_k}}_{\text{T1}} \underbrace{- \epsilon_{ijk} \omega_i \frac{1}{\rho^2} \frac{\partial \rho}{\partial x_j} \frac{\partial \tau_{kl}}{\partial x_l}}_{\text{T2}} + \underbrace{\frac{\epsilon_{ijk} \omega_i}{\rho} \frac{\partial^2 \tau_{kl}}{\partial x_j \partial x_l}}_{\text{T3}} \underbrace{- 2 \frac{\partial u_k}{\partial x_k} \Omega}_{\text{T4}} + \underbrace{\epsilon_{ijk} \frac{\omega_i}{\rho^2} \frac{\partial \rho}{\partial x_j} \frac{\partial p}{\partial x_k}}_{\text{T5}}. \tag{7.6}$$

Eq. 7.6 describes the enstrophy transport equation for the RANS averaged velocities. The temporal derivative term on the left-hand side represents the local rate of change of enstrophy concerning time. In contrast, the spatial derivative term represents the advection of enstrophy by the velocity field. The terms on the right-hand side represent the changes of enstrophy due to production from vortex stretching due to flow gradients (T1). T2 represents the cross product of two vectors, the vorticity and the viscosity torque. T3

represents the joint influence of molecular diffusion and dissipation. T4 contributes to enstrophy dissipation by accounting for the impact of dilatation. Meanwhile, T5 represents the baroclinic torque resulting from the misalignment between pressure and density gradients.

Fig. 7.9 illustrates enstrophy and its various contributing components in DW1 at $\alpha = 16°$ and $\alpha = 20°$ at equidistant chord-wise slices. Among the transport terms shown on the right-hand side of Eq. 7.6, T2 and T3 contribute the least and thus are not shown. The T1 contour values are displayed alongside the streamlines, depicting the regions with the most negative T1 values. It indicates that at angles of $\alpha = 16°$ and $\alpha = 20°$, the secondary vortices and MBV effectively dissipate enstrophy through vortex stretching on the windward side.

However, there is a difference between the two incidence cases on the leeward side. $\alpha = 20°$ features significant destruction due to the intersection of MBV and IBV, whereas $\alpha = 16°$ shows no such effect. At $\alpha = 16°$, the magnitude of T4 observed in the IBV is similar on both sides of the wing. However, the interaction between MBV and OBV on the windward side shows high negative values marked by a dotted circle. It indicates that MBV and OBV reduce vorticity strength through a dilatation process.

At $\alpha = 20°$ on the windward side, a shock causes the breakdown of the vortex, shown by the most negative values in T4 marked by a dotted circle. Baroclinic effects are observed on the MBV on the windward side for both incidence angles.

7.5 Detailed investigations of DW1 and DW2 at $\alpha = 20°$

The position of vortex breakdown displays oscillations, underscoring the transient nature of aerodynamic behaviours in transonic conditions. Fig. 7.10 shows the Q-criterion contours at different chord locations in DW1 and DW2. It reveals the location of the breakdown position at $\alpha = 20°$. On the windward side, the flow rolls up at the start of the leading edges. The breakdown of the vortex is far more downstream in DW1 than in DW2. The vortices roll up and merge downstream on the leeward side of the wing. Due to the broader spanwise width in W1, the vortex has more distance to flow spanwise than in W2. In W2, the fuselage controls the spanwise flow, making the vortex more concentrated. Whereas in W1, the vortex behavior is chaotic. It could lead to less swirl strength of the vortex, making it more susceptible to vortex breakdown. In W2, shock occurrence is delayed due to the stronger vortex development.

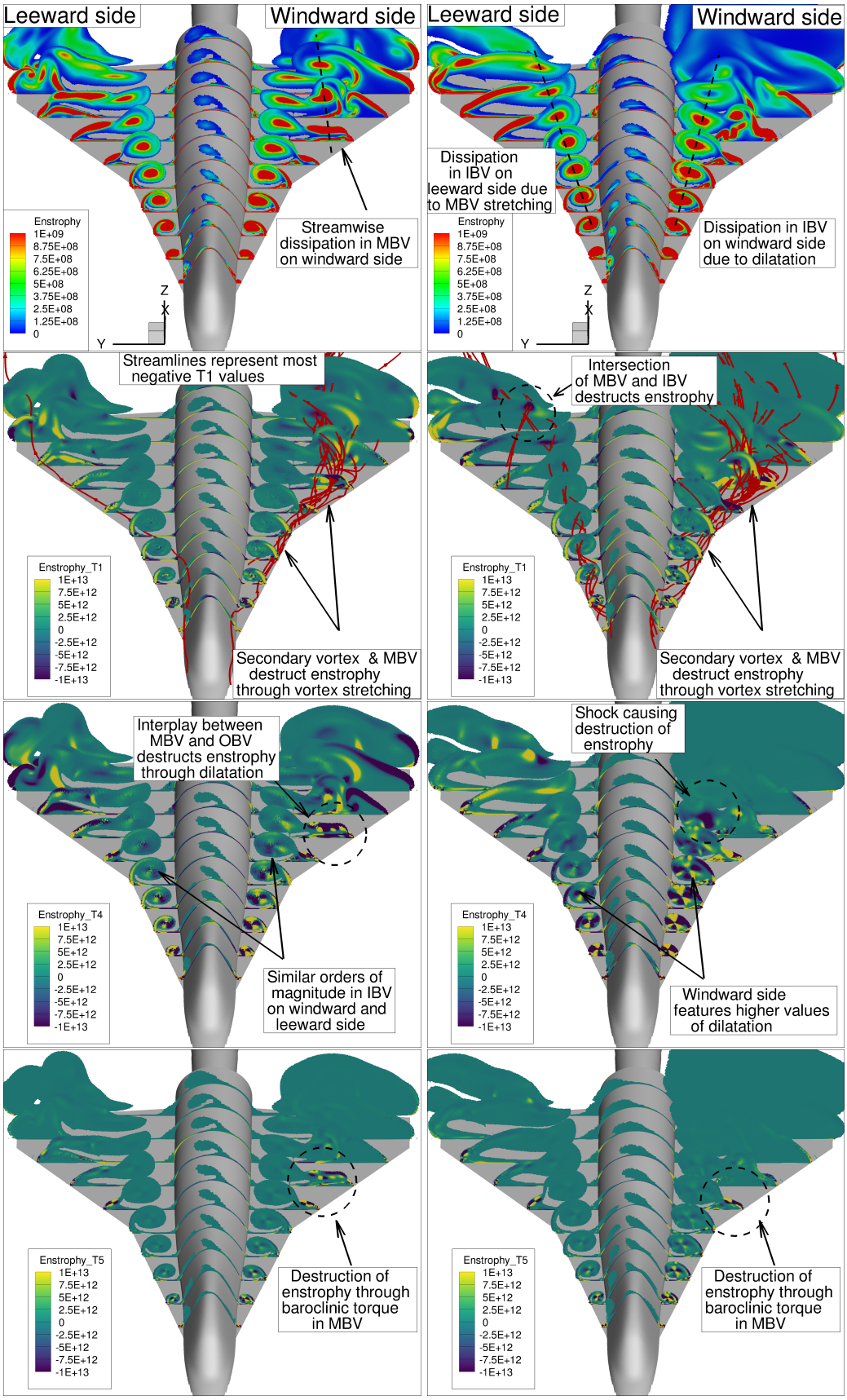

FIGURE 7.9: Enstrophy transport terms for $\alpha = 16°$ (left) and $\alpha = 20°$ (right) in DW1 at $Ma_\infty = 0.85$ and $Re_\infty = 12.53 \times 10^6$ with $AoS = 5°$ using $k - \omega$ SST model

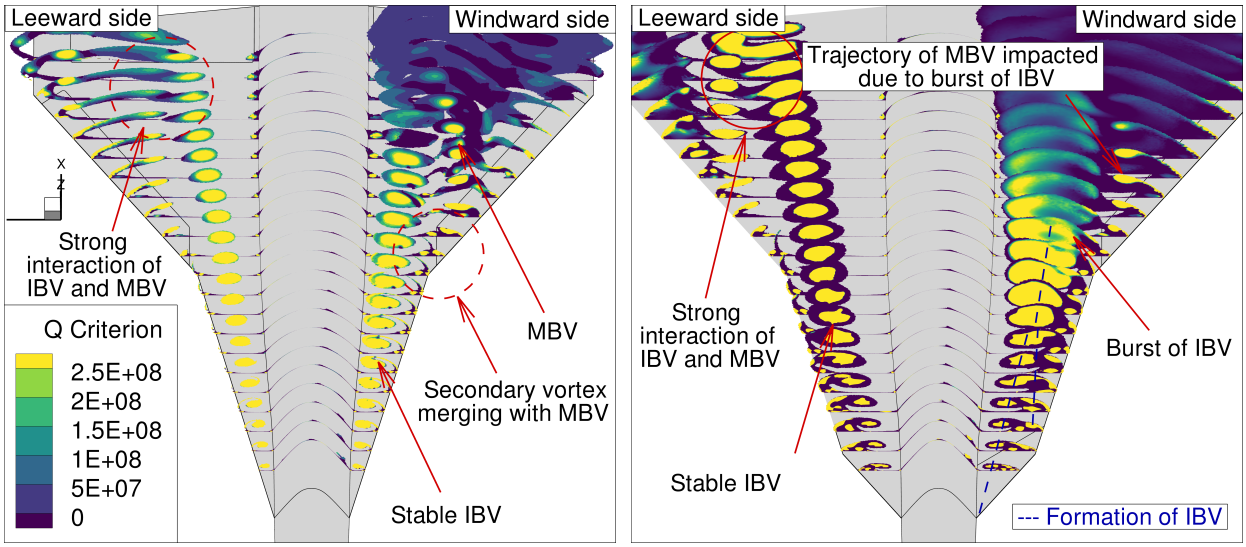

FIGURE 7.10: Vortex topology at $\alpha = 20°$ in DW1 (left) and DW2 (right) $Ma_\infty = 0.85$ and $Re_\infty = 12.53 \times 10^6$ with $AoS = 5°$ using $k - \omega$ SST model

The trajectories of IBV and MBV on the planforms, shown in Fig. 7.11 have been identified with the maximum x-vorticity. In DW2, the IBV develops close to the fuselage on the windward side, whereas MBV starts from the third-leading edge. On the leeward side, the IBV develops close to the fuselage and continues until the IBV merges with the MBV. The IBV on the windward side of DW2 undergoes deformation due to the shock, which significantly deteriorates the vortex strength. Downstream of the deformation, the unstable vortex could still be fed by the shear layer from the second leading edge. In DW1, such deformation is not present and continues to grow stronger with the downstream convection of the vortex. The vortex breakdown is characterized by a sudden drop in the vortex-core axis before the merging could happen on the windward side of DW1. On the leeward side, the merging of IBV and MBV happens on both the planforms, although the spiraling of IBV over MBV is more evident in DW2 than DW1.

Mach number and pressure coefficient have been plotted in the vortex cores in Fig. 7.12 for $\alpha = 20°$. DW1 features a steady Ma of 1.5 in the vortex core, whereas DW2, after showing the highest values in Ma of 3.0 over levcon, drops to 1.0 downstream. A similar trend is observed in the leeward sides, where a steady Ma of 1.5 is observed in DW1 and 1.0 in DW2 after the initial highest values of 2.5 over the levcon. The vortex breakdown positions are accompanied by a decrease in Ma and an increase in pressure coefficient, which is observed in the windward IBVs.

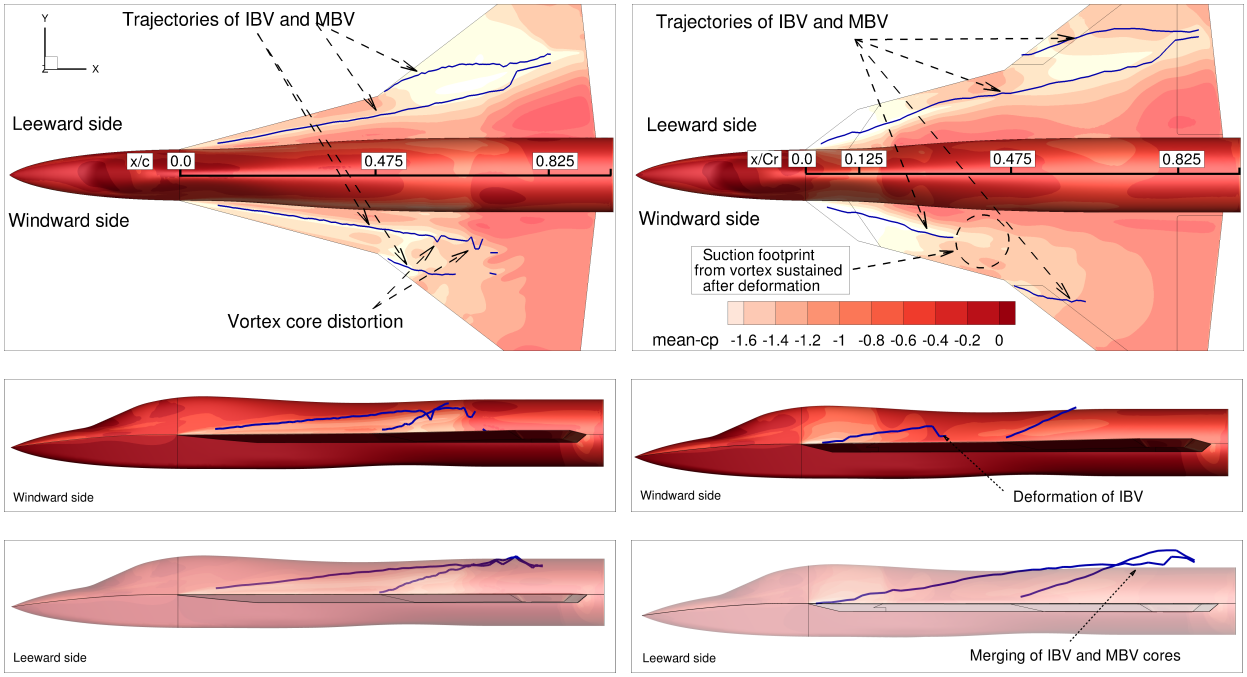

FIGURE 7.11: Trajectories of MBV and IBV at $\alpha = 20^\circ$ in DW1 (left) and DW2 (right) $Ma_\infty = 0.85$ and $Re_\infty = 12.53 \times 10^6$ with $AoS = 5^\circ$ using $k - \omega$ SST model

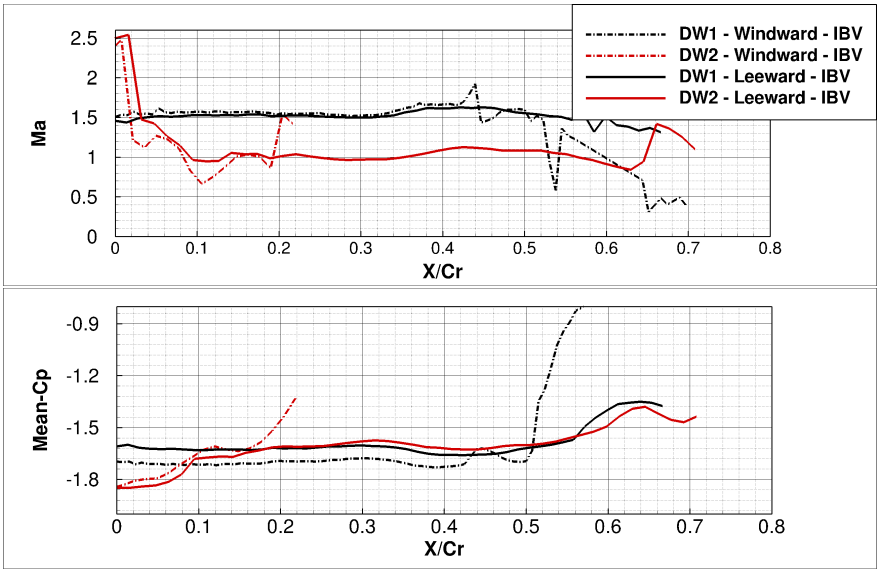

FIGURE 7.12: Vortex-core properties at $\alpha = 20$ in DW1 and DW2 $Ma_\infty = 0.85$ and $Re_\infty = 12.53 \times 10^6$ with $AoS = 5^\circ$ using $k - \omega$ SST model

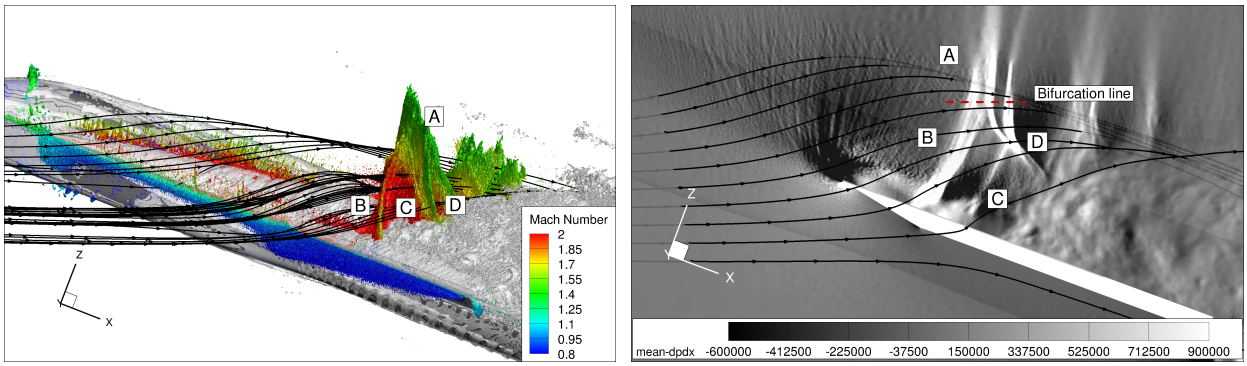

(a) 3D visualization of the lambda-shock: Iso-surfaces of $Q - criterion$ and $\partial\rho/dx$ colored by Ma

(b) Visualization of the Lambda-shock by $\partial\rho/dx$ on a slice plane normal to span

FIGURE 7.13: Time-averaged lambda-shock in DW1 at $\alpha = 20°$ $Ma_\infty = 0.85$ and $Re_\infty = 12.53 \times 10^6$ with $AoS = 5°$ using $k - \omega$ SST model

Shock bifurcation and buffeting Fig. 7.13 presents a visual representation of the lambda-shock phenomenon observed over DW1 at $\alpha = 20°$. After reaching supersonic conditions over the wing, a normal shock A is created above a certain distance from the vortex region. However, close to the wing's surface, where the IBV interacts with the normal shock, the shock bulges upstream and manifests as an oblique shock B within the bulged portion of the shockwave. A similar bulging of a normal shock near the vortex core was observed in reference [127], which numerically investigates the interaction of a longitudinal vortex with a shock wave. Unlike normal shocks, oblique shock B does not bring the supersonic flow state back to a subsonic state immediately. Instead, it alters the flow's direction while retaining its supersonic state. The shock D finally brings the flow back to a subsonic state. There is a weak shock C in the supersonic regime between shocks B and D. Fig. 7.13(b) represents the observed lambda-shock at an inclined plane parallel to the local flow velocity. The visualization plane has been chosen accordingly to observe the lambda shock, which interacts with the vortex core of the IBV.

The non-dimensional frequency ($St = fC_r/U_\infty$) of the shock and vortex breakdown oscillation is approximately 0.14. Fig. 7.14 illustrates the oscillation of the pitching moment due to the buffet for over 25 cycles due to the presence of a shock-buffet over the wing. During the buffet, the bulged portion of the shock (oblique part) oscillates between the chord positions $x/L = 0.4$ and 0.5. The buffet phenomenon may occur from the oscillation of vortex breakdown itself, whose non-dimensional frequency is observed to be around $St = 0.1$ by Menke et al. [61] or when the shock interacts with the surface, deflecting the boundary layer and altering the flow downstream of the shock. This alteration prompts the shock to readjust by moving upstream.

Selected flow states of the oscillation are shown in Fig. 7.15 to illustrate the evolution of the lambda-shock, with the corresponding instances marked in Fig. 7.14. One can observe a multitude of shocks over the wing. At state 1, a normal shock is created, recovering the flow to a subsonic state. At state 2, as the normal shock moves downstream, it weakens, with higher downstream velocity than state 1. At state 3, this normal shock undergoes bifurcation, indicating the creation of an oblique shock. Also, at this state, the shock-affected boundary layer starts to shed vortices downstream close to the wing's surface. At state 4, one can observe the presence of multiple weak shocks in the supersonic region. Until state 6, the shedding of shock-induced boundary layer vortices leads to the high-frequency oscillation of the lambda-shock, whose lifetime is longer than the low-frequency buffet of the normal shock prior to the formation of the lambda-shock in state 1. It needs to be noted that the shock-induced boundary layer vortices appear from state 3 onwards, indicating that the lambda shock causes them. Additionally, the transient aspect of the VB indicates that the lambda-shock could adapt to the VB's dynamics, leading to its buffeting. We note that the shock triggers the breakdown of IBV, yet the shifting position of the VB induces an adjustment in the shock, causing a buffeting mechanism.

In DW2, shock buffeting does not occur, and the shock induced by the kink causes the breakdown of the IBV further upstream, as observed in section 7.2. However, as the IBV undergoes breakdown, the airflow over the strake contributes to sustaining the IBV undergoing breakdown for slightly longer (see Fig. 7.16(a)). Notably, the lambda shock near the apex of the wing in DW2 remains stationary, as visualized in Fig. 7.16(b).

It appears that the position of vortex breakdown is determined by the balance between vorticity strength and shock strength [127]. Fig. 7.17 shows the x-vorticity and y-vorticity in the plane of the vortex core for both planforms. In both planforms, vortex breakdown is characterized by a vortex-core expansion. The shock in DW2 distorts the vortex axis, triggering vortex breakdown due to this distortion. As expected, the shock effect on y-vorticity is more substantial than on x-vorticity, causing significant changes in the pre-and post-shock regions.

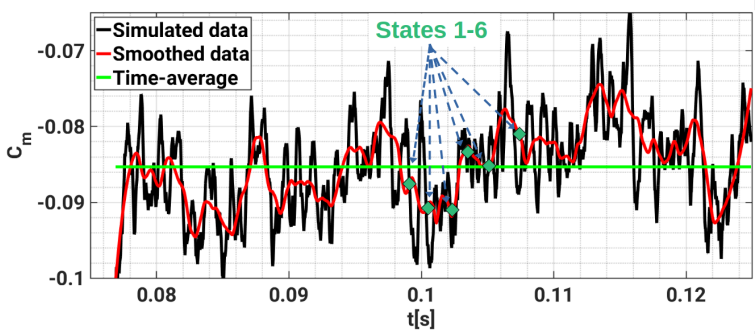

FIGURE 7.14: Quasi-periodic oscillation of C_{my} in DW1 at $Ma_\infty = 0.85$ and $Re_\infty = 12.53 \times 10^6$ with $AoS = 5°$ using SAS model

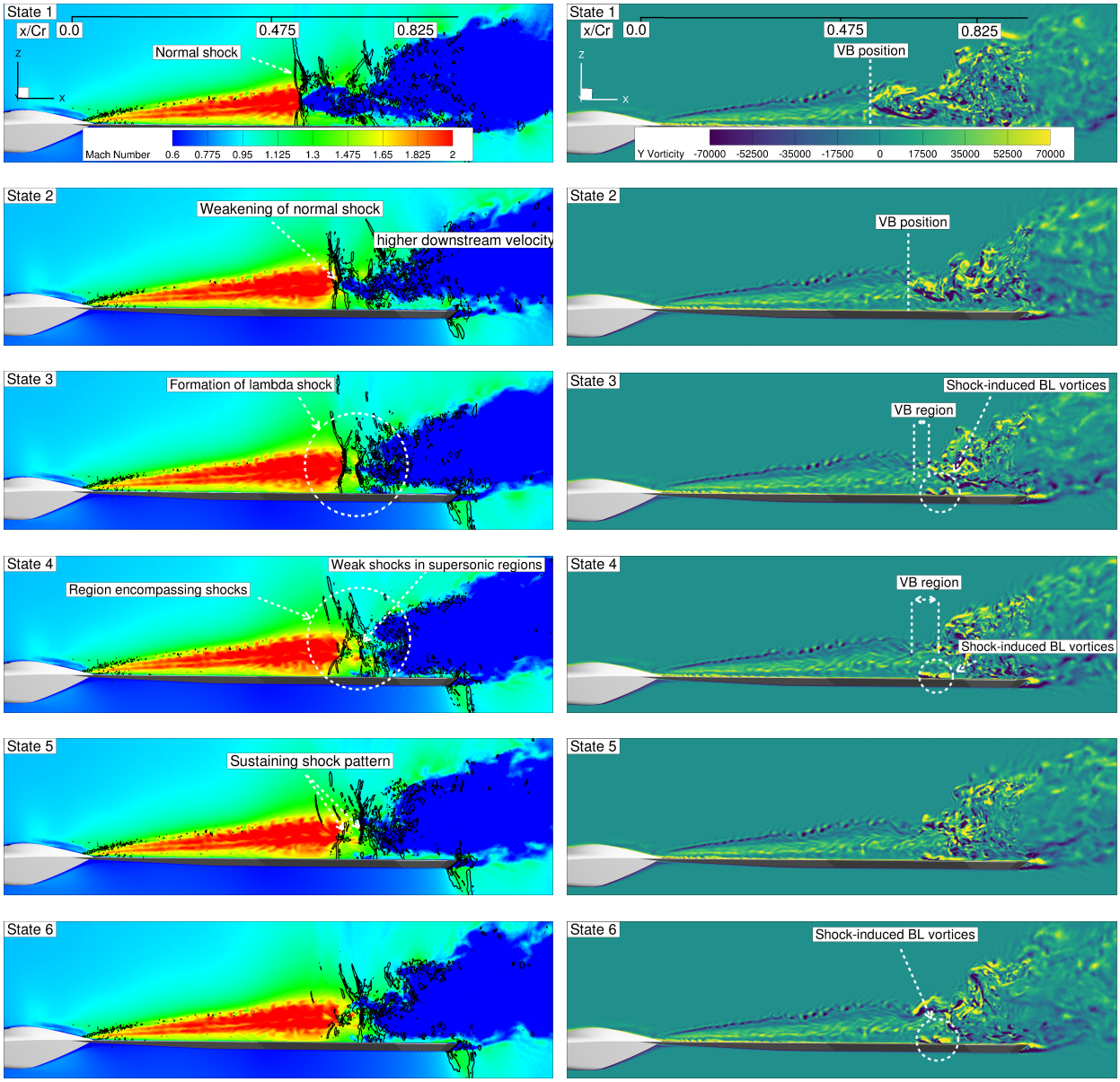

FIGURE 7.15: Evolution of lambda-shock observed through quasi-periodic states of shock buffet in DW1 $Ma_\infty = 0.85$ and $Re_\infty = 12.53 \times 10^6$ with $AoS = 5°$ using SAS model

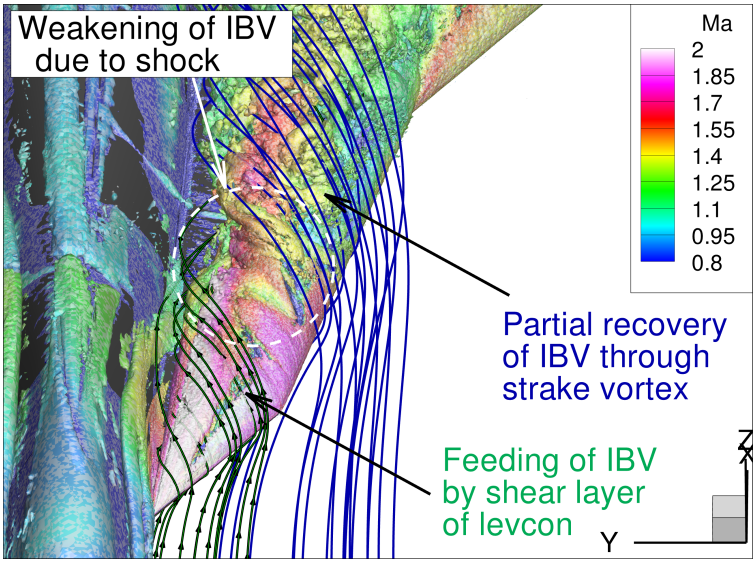

(a) Weakening and recovery of IBV

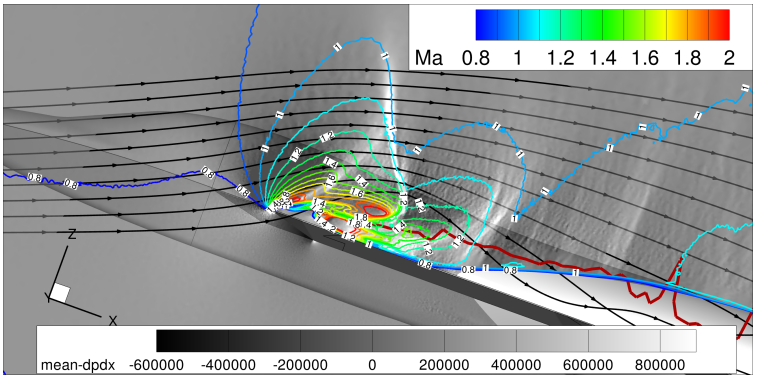

(b) Position of lambda-shock

FIGURE 7.16: Influence of lambda-shock at $\alpha = 20°$ in DW2 at $Ma_\infty = 0.85$ and $Re_\infty = 12.53 \times 10^6$ with $AoS = 5°$ using $k - \omega$ SST model

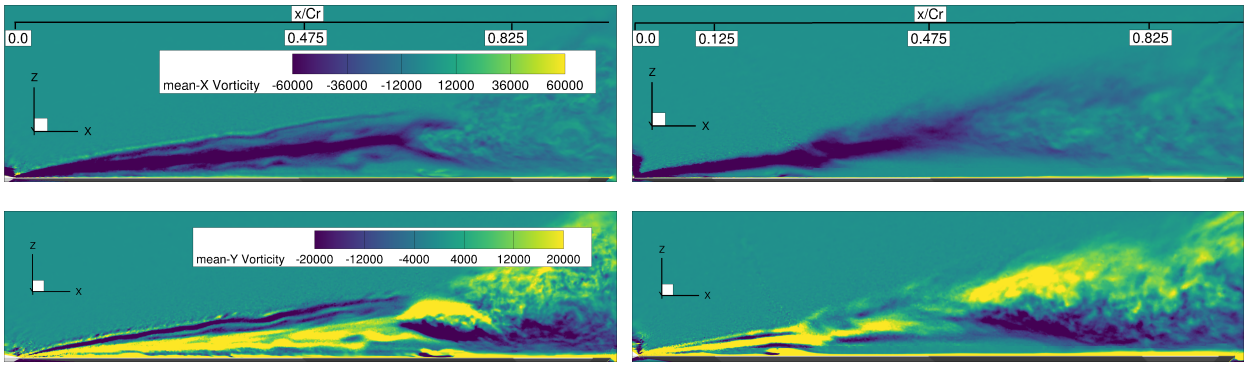

FIGURE 7.17: Mean x and y vorticity at $\alpha = 20°$ in DW1 (left) and DW2 (right) at $Ma_\infty = 0.85$ and $Re_\infty = 12.53 \times 10^6$ with $AoS = 5°$ using $k - \omega$ SST model

Chapter 8

Summary and Outlook

8.1 Cavity flows

The effect of choosing different window lengths to quantify the uncertainty in the resonating cavity flows is studied in the experimental data. This quantification is considered necessary to validate the simulation cases (see section. 6.1). Upon quantifying the uncertainty, the open-cavity configuration with sidewise doors has been studied numerically with various simulation methodologies and turbulence models. These include the SA-IDDES model with the integrated wall (DES-WR), SA-IDDDES model employing wall functions (DES-WF), and SAS with wall-resolved (SAS-WR), using wall functions (SAS-WF), and applying forcing (SAS-F) under transonic flow conditions at $Ma_\infty = 0.8$ and $Re_\infty = 12 \times 10^6$.

Initially, the objective was to find a reference solution to judge the performance of the SAS model. Therefore, as a preliminary study, DES-WR was employed for the cavity flows, where $0.125s$ of sample length was used to perform FFT analysis. It showed that the model can predict the modes quite well, although costly and noisy (see section 6.2). It was observed that the DES-WR encountered stability problems due to potentially skewed cells near door hinges. In order to fix these stability issues, scalar dissipation, which is generally more dissipative, was employed.

Another strategy is the adoption of the wall-function technique in DES-WF as illustrated in section 6.2.1, which aids in alleviating issues arising from skewed cells near door hinges and between doors and cavity walls, thereby enhancing simulation stability when using the matrix dissipation scheme. Additionally, the wall-function technique enables a longer sample length of $0.5s$, which is generally suggested in the transonic cavity flows, such as in the study by Allen et al. [33]. Therefore, the current study uses the results of DES-WF as a reference and compares results obtained with these refined numerical settings to those

from various simulation approaches, notably different variants of the SAS method. DES-WF reduced the computational cost by almost 50% compared to DES-WR. The visualisation of the cavity modes helped identify the correlation of the Rossiter modes with the flow processes in detail. The streamwise dominant modes were observed under straight flow conditions. Mode 1 correlates to the oscillation of the shear layer, whereas higher modes correlate to the coherent flow structures of the cavity. It is also observed generally that under higher spatial and time-step sizes, the magnitudes of the modes are over-predicted, while the frequency prediction remains accurate.

Investigations into SAS models were successful as they could predict the cavity spectra with 95% computational efficiency compared to the wall-resolved DES model, as explained in section 6.3. A mesh convergence study was conducted to find an appropriate mesh for the SAS-WR model. The boundary layer profile upstream of the cavity has been compared with the DES-WF results, and simulation data have been collected along the probe locations. Due to high unsteady fluctuations in the shear layer, the structures were resolved through the source term Q_{SAS} and this led to good prediction of the spectral magnitudes. When WF is combined with the SAS model, the modal magnitudes are over-predicted due to very strong vortical structures inside the cavity. Wall function had made the flow quasi-steady in the near-wall regions upstream of the cavity, which resulted in larger eddies with higher eddy viscosity levels that were too strong to break down flowing into the cavity.

To overcome the issue with SAS-WF, a forcing feature has been used instead to force fluctuations to convert modelled turbulent kinetic energy to resolved turbulent kinetic energy. It resulted in better prediction of the modal magnitudes as good as the SAS-WR and DES-WF models. In addition, the shear layer, vorticity levels, and Reynolds stresses predicted were good and in agreement with the DES-WF results.

Furthermore, the mechanism behind the Rossiter modes under sideslip conditions and their modulations has been discussed in section 6.4. It has been shown using isosurfaces of the modes that a significantly higher interference of waves occurs in a highly three-dimensional manner between the walls of the cavity. Mode 1 results from the skewed shear-layer dynamics, and higher modes contain less skewed shear-layer contents along with spanwise reflecting waves. In addition to the streamwise waves, a significant wave interference occurs in the spanwise direction due to the flow impingement on the leeward door. It is beyond the scope of this work to show the performance of SAS-F for sideslip conditions. However, it would be worth investigating its performance under skewed flow behaviour concerning the front edge of the cavity. Moreover, additional flow cases with asymmetric flow conditions would reveal more significant 3D effects in the cavity.

Overall, it has been proven that all three SAS variants can capture the Rossiter frequencies well, except for a marginal overprediction of spectral magnitudes by the SAS-WF simulation. The reason for the overprediction behaviour in the SAS-WF simulation has been investigated with the boundary layer profile and the resolved fluctuations inside the cavity. The commonalities and differences between SAS and SAS-WF simulations were investigated and outlined using the Q_{SAS} and vorticity fields. The overprediction has been investigated and identified as caused by the lack of resolved turbulence inside the cavity. The artificial forcing technique has been employed to overcome the problem of the URANS regions in the SAS-WF simulation. Regarding computational requirements, the DES-WF and SAS-WR simulations are estimated to be around 50% and 90% cheaper than DES-WR, respectively. In contrast, the SAS-WF and SAS-F simulations are almost twice as fast as the SAS-WR simulation.
It is important to highlight that SAS-F necessitates meticulous numerical configuration, as it involves making engineering judgments regarding the dimensions of the forcing zone. In this research, half the cavity length was employed as the length of the forcing zone. Furthermore, initial experimentation involving variations in the dimensions of the forcing zone showed no notable deviation concerning cavity spectra. However, these variations could affect the RMS pressure distribution of the cavity walls where the forcing zone ends spanwise.

8.2 Leading-edge vortex on delta wings

Regarding leading-edge vortices on delta wings, article presents a comprehensive numerical study of double- and triple-delta wing planforms under transonic flow conditions in leading-edge vortical flows. The flow characteristics include a Mach number (Ma_∞) of 0.85 and a Reynolds number (Re_∞) of 12.53×10^6, accompanied by a sideslip angle (β) of 5°. The turbulence models, namely the $k-\omega$ SST and SAS model accurately predict the lift, with the pitching moment being more sensitive to the location of vortex breakdown. It underscores the challenges in precisely capturing vortex breakdown in transonic flow conditions (see section 7.1).
The vortex topology of the planforms under different angles of attack has been observed in section 7.2. Typically, the MBV tends to roll over the IBV without any significant interaction on the windward side. However, on the leeward side, a noticeable interaction between the MBV and the IBV forms a more robust vortex system. At low angles of incidence ($\alpha = 16°$ and 20°), the interaction between MBVs and outboard vortices (OBVs)

is more pronounced. Conversely, at high angles of incidence ($\alpha = 24^\circ$ and 28°), the interaction between MBVs and IBVs becomes more evident, as seen in Fig. 7.2 and 7.3. Typically, a noticeable unwrapping pattern emerges within the vortices, coupled with an enlargement of the vortex core diameter as the angle of incidence increases. Furthermore, vortices generated over the main wing (MBV and OBVs) exhibit reduced prominence in high-incidence cases.

On the double-delta wing, at a low incidence angle of 16°, the IBV and MBV develop and sustain the shock without breaking down due to very strong concentrated vortex development. At higher incidence angles of 20°, strong interaction between the IBV and MBV on the windward side and the shock leads to subsequent breakdown. At this incidence angle, the triple-delta wing features a shock, causing IBV to break down more upstream due to its less stable character.

The enstrophy analysis (see section 7.4) of DW1 at $\alpha = 16^\circ$ and $\alpha = 20^\circ$ reveals distinct characteristics in vortex dynamics. At $\alpha = 16^\circ$, the interaction between the secondary vortices and MBV dissipates enstrophy through vortex stretching on the windward side, with minimal impact on the leeward side. Conversely, at $\alpha = 20^\circ$, significant destruction occurs on the leeward side due to the intersection of MBV and IBV. The dilatation process, mainly observed through the dilation term of the enstrophy transport equation, highlights the reduction of vorticity strength in the MBV and OBV on the windward side. Additionally, at $\alpha = 20^\circ$, the shock induces vortex breakdown primarily in the MBV on the windward side, and baroclinic effects are observed in the MBV on the windward side for both incidence angles.

Furthermore, a fundamental difference arises between the double-delta and triple-delta wings in their response to vortex breakdown and shock buffet at $\alpha = 20^\circ$, which is illustrated in section 7.5. The analysis highlights that the double-delta wing undergoes shock-induced vortex breakdown, and the transient nature of this breakdown prompts adjustments in the shock position, resulting in a shock buffet. Conversely, the breakdown in the triple-delta wing is associated with a stationary shock induced by the kink in the planform. The SAS model reveals a quasi-periodic oscillation of the pitching moment, offering a detailed visualisation of the lambda-shock evolution. This observation unveils the causal relationship between shock buffet and vortex breakdown. Examining the dilatation term in the enstrophy transport equation clarifies that the lambda-shock drives vortex breakdown in the double-delta wing. These findings underscore the intricate interplay between shock-induced effects and vortex dynamics, shedding light on the complex aerodynamic behaviour of the planforms. It is observed that the orientation of the lambda-shock in triple-delta wing planforms is determined by the sweep angle ϕ_1 of the

levcon surface (see Fig. 5.6). This angle directly influences the strength of the shock over the wing apex, consequently affecting the inboard boundary vortex (IBV) and subsequent vortices. A parametric study focusing on swirl strength and ϕ_1 as an initial step could help reduce IBV susceptibility to breakdown.

Chapter 9

Publications

This chapter provides a comprehensive list of articles and contributions published during the course of this work.

9.1 Journals

- **K. Rajkumar**, E. Tangermann, M. Klein, S. Ketterl and A. Winkler. "Time-efficient Simulations of Fighter Aircraft Weapon Bay." *CEAS Aeronautical Journal*, January 2023.
- **K. Rajkumar**, E. Tangermann and M. Klein. "Efficient Scale-Resolving Simulations of Open Cavity Flows for Straight and Sideslip Conditions." *Fluids*, Vol. 8, August 2023.
- **K. Rajkumar**, T. Di Fabbio, E. Tangermann and M. Klein. "Physical Aspects of Vortex-Shock Dynamics in Delta-Wing Configurations." *Physics of fluids, 2024*.
- T. Di Fabbio, **K. Rajkumar**, E. Tangermann and M. Klein. "Towards the Understanding of Vortex Breakdown for Improved RANS Turbulence Modeling." *Aerospace Science and Technology*, 2024.

9.2 Book Chapter

- **K. Rajkumar**, E. Tangermann and M. Klein. "DES of Weapon Bay in Fighter Aircraft Under High-Subsonic and Supersonic Conditions." In: *Notes on Numerical Fluid Mechanics and Multidisciplinary Design*, Vol. 151, 2021.

9.3 Conferences

- **K. Rajkumar**, E. Tangermann, M. Klein, S. Ketterl and A. Winkler. "Time-efficient Simulations of Fighter Aircraft Weapon Bay." Presented at *Aerospace Europe Conference*, Poland, 2021.
- **K. Rajkumar**, E. Tangermann and M. Klein. "Towards High Fidelity Weapon Bay Simulations at Affordable Computational Cost." Presented at *AIAA Aviation Forum*, Chicago, 2022.
- **K. Rajkumar**, E. Tangermann, J. Radtke and M. Klein. "Open Cavity Simulations Under Sideslip Conditions." Presented at *Congress of the International Council of the Aeronautical Sciences*, Stockholm, 2022.

Chapter 10

Appendices

Spectral analysis Power spectral density (PSD) is a measure of energy contained in the pressure signal as a function of frequencies. In statistical signal processing, spectral density estimation involves the process of deducing the spectral density, also referred to as power spectral density, of a stochastic signal. This is accomplished by analyzing a sequence of temporal signal samples. Fundamentally, the spectral density encapsulates the frequency composition of the signal. The objective of estimating it is to identify potential periodic patterns within the data, observed as heightened peaks corresponding to these specific frequencies. In this study, the PSD is employed for analyzing the frequency characteristics of a signal at a specific point, derived from the fluctuating pressure ($p' = p - \overline{p}$). If T is a total length of signal in s, then $T_{fft} = T/5$ is chosen as a FFT window length. Then, $1/T_{fft}$ is the frequency resolution and minimum frequency that the FFT can resolve and $1/(2 \times \Delta T)$ is the maximum frequency that the FFT can resolve. It is often useful to express the power spectral density in dB relative to $P_{ref} = 2 \times 10^{-5}$. Fig. 10.1 shows FFT of $Ma_\infty = 1.2$ predicted by SAS-WR compared with the experiment data.

$$SPL(f) = 10log_{10}(\frac{PSD(f)}{P_{ref}^2}) \tag{10.1}$$

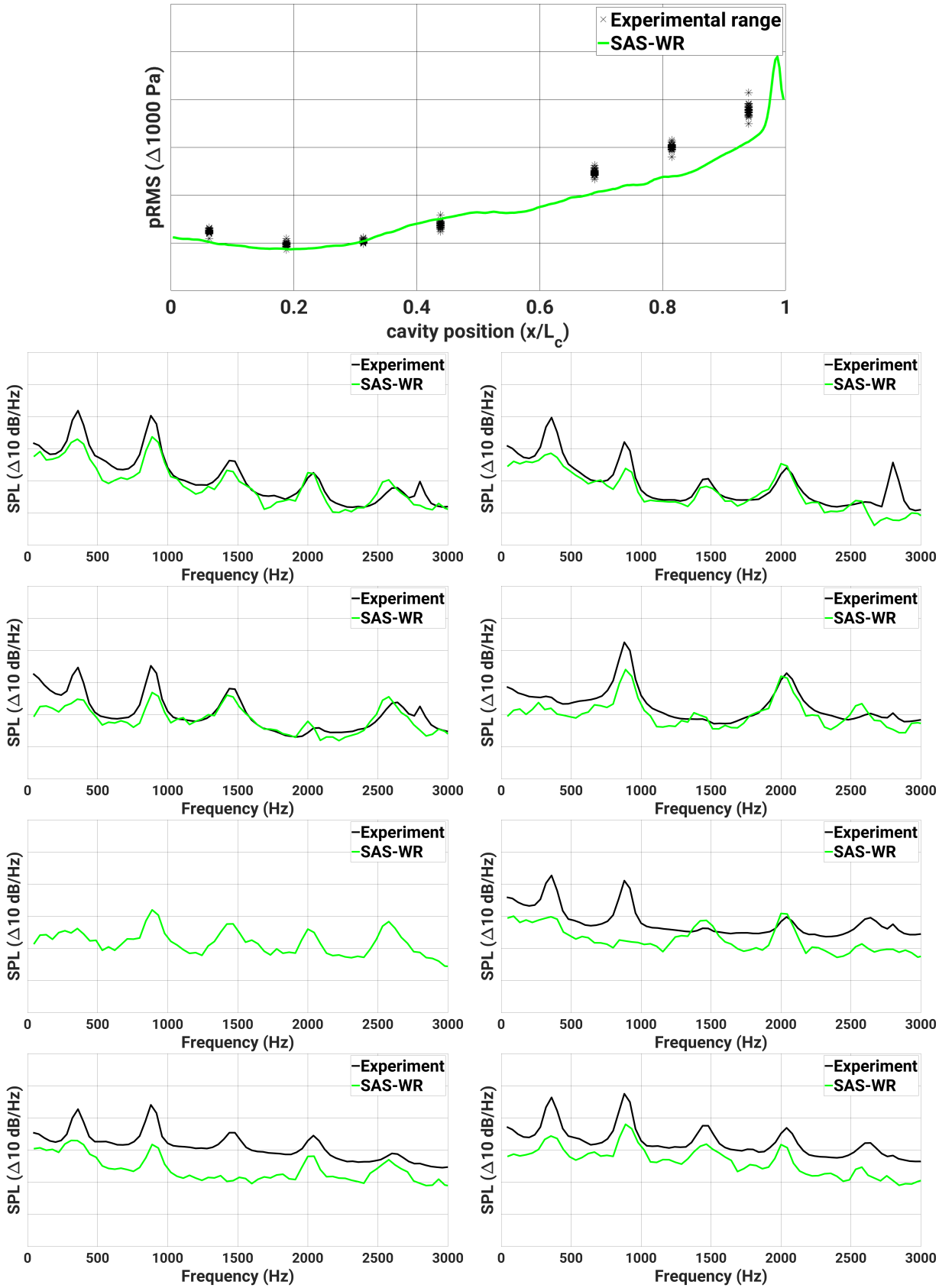

FIGURE 10.1: Prediction of RMS pressure and cavity modes by SAS-WR in $Ma_\infty = 1.2$

Bibliography

[1] N. Sinha, S. Arunajatesan, J. Shipman, and J. Seiner. "High fidelity simulation and measurements of aircraft weapons bay dynamics". *7th AIAA/CEAS Aeroacoustics Conference and Exhibit* (2001). DOI: 10.2514/6.2001-2125.

[2] M. Lee and M. Ho. "Lift force of delta wings". *Applied Mechanics Reviews* 43 (9 1990), pp. 209–221.

[3] P. B. Earnshaw and J. A. Lawford. "Low-Speed Wind-Tunnel Series of Sharp-Edged Experiments on Delta Wings". *Aeronautical research council, Reports and memoranda* (1964).

[4] L. E. Ericsson and J. P. Reding. "Fluid dynamics of unsteady separated flow. Part 1. Bodies of revolution". *Progress in Aerospace Sciences* 23 (1 1986), pp. 1–84.

[5] P. T. Fink and J. Taylor. "Some Early Experiments on Vortex Separation". *Aeronautical research council, Reports and memoranda* (1966).

[6] Wikimedia Commons. *File:F-22 Raptor shows its weapon bay.jpg — Wikimedia Commons, the free media repository*. [Online; accessed 25-March-2024]. 2021.

[7] Wikimedia Commons. *File:F-35 Heritage Flight Team performs in Bell Fort Worth Alliance AirShow.jpg — Wikimedia Commons, the free media repository*. [Online; accessed 25-March-2024]. 2024.

[8] J. E. Rossiter. "Wind tunnel experiments on the flow over rectangular cavities at subsonic and transonic speeds". *Aeronautical research council, Reports and memoranda* (1964).

[9] G. J. M. Loupy and G. N. Barakos. *Understanding Transonic Weapon Bay Flows*. 2018.

[10] S. J. Lawson and G. N. Barakos. "Review of numerical simulations for high-speed, turbulent cavity flows". *Progress in Aerospace Sciences* 47 (3 2011), pp. 186–216. DOI: 10.1016/j.paerosci.2010.11.002.

[11] S. V. Babu, G. Zografakis, G. N. Barakos, and A. Kusyumov. "Evaluation of scale-adaptive simulation for transonic cavity flows". *International Journal of Engineering Systems Modelling and Simulation* 8 (2 2016), pp. 106–124. DOI: 10.1504/IJESMS.2016.075510.

[12] R. Johnson, M. Bruce Davis, and D. Finley. "Relaxed Fidelity CFD Methods Applied to Store Separation Problems". *NATO Report, RTO-MP-AVT-108* (2004).

[13] C. J. Coley and A. J. Lofthouse. "Correlation of weapon bay resonance and store unsteady force and moment loading". *50th AIAA Aerospace Sciences Meeting Including the New Horizons Forum and Aerospace Exposition* (2012). DOI: 10.2514/6.2012-415.

[14] R. M. Cummings and A. Schütte. "Assessment of Stability and Control Prediction Methods for NATO Air and Sea Vehicles". *NATO RTO Technical Report, RTO-AVT-TR-161* (2009).

[15] J. Seifert. "SAGITTA-Nationale Forschungskooperation fuer fortschrittliche UAV-Technologien im Rahmen der Open Innovation Initiative von Cassidian". *61th Deutscher Luft-und Raumfahrtkongress, Berlin, Germany* 1352 (2012).

[16] A. Dillmann, G. Heller, E. Krämer, C. Wagner, C. Tropea, and S. Jakirlić. "New results in numerical and experimental fluid mechanics". *Notes on Numerical Fluid Mechanics and Multidisciplinary Design* 142 (2018).

[17] H. H. Heller, D. G. Holmes, and E. E. Covert. "Flow-induced pressure oscillations in shallow cavities". *Journal of Sound and Vibration* 18 (1971), pp. 545–553.

[18] O. H. Unalmis, N. T. Clemens, and D. S. Dolling. "Cavity Oscillation Mechanisms in High-Speed Flows". *AIAA Journal* 42 (10 2004), pp. 2035–2041. DOI: 10.2514/1.1000.

[19] T. Handa, H. Miyachi, H. Kakuno, T. Ozaki, and S. Maruyama. "Modeling of a feedback mechanism in supersonic deep-cavity Flows". *AIAA Journal* 53 (2 2015), pp. 420–425. DOI: 10.2514/1.J053184.

[20] J. L. Wagner, K. M. Casper, S. J. Beresh, S. Arunajatesan, J. F. Henfling, R. W. Spillers, and B. O. Pruett. "Relationship between acoustic tones and flow structure in transonic cavity flow". *45th AIAA Fluid Dynamics Conference* (2015), pp. 1–16.

[21] X. Gloerfelt, C. Bailly, and D. Juvé. "Direct computation of the noise radiated by a subsonic cavity flow and application of integral methods". *Journal of Sound and Vibration* 266 (1 2003), pp. 119–146. DOI: 10.1016/S0022-460X(02)01531-6.

[22] L. N. Cattasfesta III, S. Garg, M. S. Kegerise, and G. S. Jones. "Experiments on compressible flow-induced cavity oscillations". *AIAA Fluid dynamics conference* 98 (1998), p. 2912.

[23] J. C. Lin and D. Rockwell. "Organized oscillations of initially turbulent flow past a cavity". *AIAA* 39 (6 2001), pp. 1139–1151.

[24] C. H. Woo, J. S. Kim, and K. H. Lee. "Three-dimensional effects of supersonic cavity flow due to the variation of cavity aspect and width ratios". *Journal of Mechanical Science and Technology* 22 (3 2008), pp. 590–598. DOI: 10.1007/s12206-007-1103-9.

[25] J. Henderson, K. Badcock, and B. E. Richards. "Subsonic and transonic transitional cavity flows". *6th Aeroacoustics Conference and Exhibit* (c 2000). DOI: 10.2514/6.2000-1966.

[26] K. Krishnamurty. "Acoustic Radiation from Two-dimensional Rectangular Cutouts in Aerodynamic Surfaces". *Naca Technical Note* (3457 1955), p. 36.

[27] C. W. Rowley, T. Colonius, and A. J. Basu. "On self-sustained oscillations in two-dimensional compressible flow over rectangular cavities". *Journal of Fluid Mechanics* 455 (2002), pp. 315–346. DOI: 10.1017/S0022112001007534.

[28] X. Zhang. "Compressible cavity flow oscillation due to shear layer instabilities and pressure feedback". *AIAA Journal* 33 (8 1995), pp. 1404–1411. DOI: 10.2514/3.12845.

[29] S. H. Shih, A. Hamed, and J. J. Yeuan. "Unsteady supersonic cavity flow simulations usingcoupled k-epsilon and navier-stokes equations". *AIAA Journal* 32 (10 1994), pp. 2015–2021. DOI: 10.2514/3.12246.

[30] L. Larchevêque, P. Sagaut, and O. Labbé. "Large-eddy simulation of a subsonic cavity flow including asymmetric three-dimensional effects". *Journal of Fluid Mechanics* 577 (July 2019 2007), pp. 105–126. DOI: 10.1017/S0022112006004502.

[31] K. Chang, G. Constantinescu, and S. O. Park. "Assessment of predictive capabilities of detached eddy simulation to simulate flow and mass transport past open cavities". *Journal of Fluids Engineering, Transactions of the ASME* 129 (11 2007), pp. 1372–1383. DOI: 10.1115/1.2786529.

[32] H. Wang, M. Sun, N. Qin, H. Wu, and Z. Wang. "Characteristics of oscillations in supersonic open cavity flows". *Flow, Turbulence and Combustion* 90 (1 2013), pp. 121–142. DOI: 10.1007/s10494-012-9434-8.

[33] R. Allen, F. Mendonca, and D. Kirkham. "RANS and DES turbulence model predictions on the M219 cavity at M=0.85". *RTO AVT Symposium* (2004), p. 18.

[34] P. Nayyar, G. N. Barakos, and K. J. Badcock. "Numerical study of transonic cavity flows using large-eddy and detached-eddy simulation". *The Aeronautical Journal* 111 (1117 2007), pp. 153–164. DOI: 10.1017/S0001924000004413.

[35] M. J. Stanek, M. R. Visbal, D. P. Rizzetta, S. G. Rubin, and P. K. Khosla. "On a mechanism of stabilizing turbulent free shear layers in cavity flows". *Computers and Fluids* 36 (10 2007), pp. 1621–1637. DOI: 10.1016/j.compfluid.2007.03.011.

[36] F. R. Menter and Y. Egorov. "The scale-adaptive simulation method for unsteady turbulent flow predictions. part 1: Theory and model description". *Flow, Turbulence and Combustion* 85 (1 2010), pp. 113–138. DOI: 10.1007/s10494-010-9264-5.

[37] S. Girimaji, H. Werner, S. Peng, and D. Schwamborn. "Progress in hybrid RANS-LES modelling". *Notes on Numerical Fluid Mechanics and Multidisciplinary Design* (130 2015), pp. 19–21.

[38] F. R. Menter, A. Garbaruk, P. Smirnov, D. Cokljat, and F. Mathey. "Scale-adaptive simulation with artificial forcing". *Notes on Numerical Fluid Mechanics and Multidisciplinary Design* 111 (January 2010), pp. 235–246. DOI: 10.1007/978-3-642-14168-3_20.

[39] F. Mayer, S. Mancini, and A. Kolb. "Experimental investigation of installation effects on the aeroacoustic behaviour of rectangular cavities at high subsonic and supersonic speed". *Deutscher Luft- und Raumfahrtkongress, Germany* (2020).

[40] S. Langer, A. Schwöppe, and N. Kroll. "The DLR flow solver TAU - status and recent algorithmic developments". *52nd Aerospace Sciences Meeting* (2014). DOI: 10.2514/6.2014-0080.

[41] K. Rajkumar, E. Tangermann, and M. Klein. "Towards high fidelity weapon bay simulations at affordable computational cost". *AIAA Aviation Forum* (2022).

[42] S. M. Hitzel. "Challenges and Needs for the Understanding of Combat Aircraft Aerodynamics". *STO-MP-AVT-307* 19 (2019).

[43] M. Lee and C. M. Ho. "Lecture Notes in Engineering - Frontiers in Experimental Fluid Mechanics, chapter Vortex Dynamics of Delta Wings". *Springer Verlag* (1989), pp. 365–427.

[44] A. Stanbrook and L. C. Squiref. "Possible Types of Flow at Swept Leading Edges". *Aeronautical Quarterly* 15 (1 1964), pp. 72–82. DOI: 10.1017/S0001925900003024.

[45] D. S. Miller and R. M. Wood. "An investigation of wing leading-edge vortices at supersonic speeds". *Proceedings of the AIAA Applied Aerodynamics Conference, Danvers, Massachusetts*, (1983).

[46] E. C. Polhamus. "A concept of the vortex lift of sharp-edge delta wings based on a leading-edge-suction analogy". *NASA Technical Note* (1966).

[47] P. Wilders, A. Ecer, J. Periaux, N. Satofuka, and P. Fox. "Parallel computational fluid dynamics, Practice and Theory" (2002).

[48] C. Breitsamter. *Unsteady flow phenomena associated with leading-edge vortices*. 2008. DOI: 10.1016/j.paerosci.2007.10.002.

[49] I. Gursul. "Recent developments in delta wing aerodynamics". *Aeronautical Journal* 108 (1087 2004), pp. 437–452. DOI: 10.1017/S0001924000000269.

[50] H. Werle. "Quelques resultats experimentaux sur les ailes en flche, aux faibles vitesses, obtenus en tunnel hydrodynamique". *La Recherche Aeronautique* 41 (1954), pp. 15–21.

[51] N. C. Lambourne and D. W. Bryer. "The Bursting of Leading-Edge Vortices Some Observations and Discussion of the Phenomenon". *Aeronautical research council* (1962).

[52] J. H. Faler and S. Leibovich. "Disrupted states of vortex flow and vortex breakdown". *Physics of Fluids* 20 (9 1977), pp. 1385–1400. DOI: 10.1063/1.862033.

[53] F. M. Payne, T. T. Ng, R. C. Nelson, and L. B. Schiff. "Visualization and wake surveys of vortical flow over a delta wing". *AIAA Journal* 26 (2 1988), pp. 137–143. DOI: 10.2514/3.9864.

[54] J. R. Chambers and S. B. Grafton. "Aerodynamic Characteristics of Airplanes at High Angles of Attack". *NASA Technical Memorandum* (1977).

[55] J. R. Chambers and E. L. Analin. "Analysis of lateral-dl rectional stability character1 stics of a twin-jet fighter airplane at high angles of attack". *NASA Technical note* (1969).

[56] T. Brooke Benjamin. "Theory of the vortex breakdown phenomenon". *Fluid mechanics* (1962), pp. 593–629.

[57] J. M. Delery. "Aspects of vortex breakdown". *Progress in Aerospace Sciences* 30 (1994), pp. 1–59.

[58] M. Escudier. "Vortex breakdown: observations and explanations". *Progress in aerospace sciences* 25 (1988), pp. 189–229.

[59] S. Leibovich. "Vortex stability and breakdown - survey and extension". *AIAA Journal* 22 (9 1984), pp. 1192–1206. DOI: 10.2514/3.8761.

[60] S. Morton, J. Forsythe, A. Mitchell, and D. Hajek. "DES and RANS simulations of delta wing vortical flows". American Institute of Aeronautics and Astronautics Inc., 2002. DOI: 10.2514/6.2002-587.

[61] M. Menke, H. Yang, and I. Gursul. "Experiments on the unsteady nature of vortex breakdown over delta wings". *Experiments in Fluids* 27 (1999), pp. 262–272.

[62] A. K Garg and S. Leibovich. "Spectral characteristics of vortex breakdown flowfields". *Physics of fluids* 22 (1979), pp. 2053–2064.

[63] M. V. Lowson. "Some experiments with vortex breakdown". *Journal of Royal Aeronautical Society* 68 (1964), pp. 343–346.

[64] S. Wolfe, J.C. Lin, and D. Rockwell. "Buffeting at the leading-edge of a flat plate due to a streamwise vortex: Flow structure and surface pressure loading". *Journal of Fluids and Structures* 9 (1995), pp. 359–370.

[65] I. Gursul and H. Yang. "On fluctuations of vortex breakdown location". *Physics of Fluids* 7 (1 1995), pp. 229–231. DOI: 10.1063/1.868724.

[66] P. R. Spalart, W. H. Jou, M. Strelets, and S. R. Allmaras. "Comments on the feasibility of LES for wings and on a hybrid RANS/LES approach". *Advances in DNS/LES* 1 (January 1997), pp. 4–8.

[67] S. Pfnür and C. Breitsamter. "Leading-edge vortex interactions at a generic multiple swept-wing aircraft configuration". *Journal of Aircraft* 56 (6 2019), pp. 2093–2107. DOI: 10.2514/1.C035491.

[68] D. H. Peckham and S. A. Atkinson. "Preliminary Results of. Low Speed Wind Tunnel Tests on a Gothic Wing of Aspect Ratio I-0". *Aeronautical research council* (1960), pp. 1–38.

[69] D. L. Darmofal and E. M. Murman. "On the trapped wave nature of axisymmetric vortex breakdown". American Institute of Aeronautics and Astronautics Inc, AIAA, 1994. DOI: 10.2514/6.1994-2318.

[70] L. A. Schiavetta, O. J. Boelens, S. Crippa, R. M. Cummings, W. Fritz, and K. J. Badcock. "Shock effects on delta wing vortex breakdown". *Journal of Aircraft* 46 (3 2009), pp. 903–914. DOI: 10.2514/1.38792.

[71] I. Gursul. "Review of unsteady vortex flows over slender delta wings". *Journal of Aircraft* 42 (2 2005), pp. 299–319. DOI: 10.2514/1.5269.

[72] A. M. Mitchell. "Research into vortex breakdown control". *Progress in Aerospace Sciences* 37 (2001), pp. 385–418.

[73] Z. Rusak and D. Lamb. "Prediction of vortex breakdown in leading-edge vortices above slender delta wings". *Journal of Aircraft* 36 (4 1999), pp. 659–667. DOI: 10.2514/2.2508.

[74] M. Jones, A. Hashimoto, and Y. Nakamura. "Criteria for vortex breakdown above high-sweep delta wings". *AIAA Journal* 47 (10 2009), pp. 2306–2320. DOI: 10.2514/1.37177.

[75] S. Pfnür, A. Hövelmann, D. Sedlacek, and C. Breitsamter. "Vortex Flow Interaction Phenomena on Multi Swept Delta Wings at Subsonic Speeds". *NATO - 1STO-MP-AVT-307* (1), pp. 1–23.

[76] S. Hitzel. "Status of Vortex Interaction on Combat Aircraft-Physics Understood, Simulation Tool Demands, Quality and Cost". *AIAA Paper No. 2022-0159, AIAA SciTech Forum* (2022).

[77] S. Hitzel. "Combat Aircraft Vortex Interaction-Design, Physics and CFD-Tools". *AIAA Paper No. 2022-0156, AIAA SciTech Forum* (2022).

[78] A. Hövelmann, A. Winkler, S. M. Hitzel, K. Richter, and M. Werner. "Analysis of Vortex Flow Phenomena on Generic Delta Wing Planforms at Transonic Speeds". *New Results in Numerical and Experimental Fluid Mechanics XII* (2020). Ed. by Gerd, Krämer Ewald, Wagner Claus, Tropea Cameron, Jakirlić Suad Dillmann Andreas, and Heller, pp. 307–316.

[79] S. Hitzel, A. Winkler, and A. Hövelmann. "Vortex Flow Aerodynamic Challenges in the Design Space for Future Fighter Aircraft". Ed. by Gerd, Krämer Ewald, Wagner Claus, Tropea Cameron, Jakirlić Suad Dillmann Andreas, and Heller. Springer International Publishing, 2020, pp. 297–306.

[80] A. Schütte and R. N. Marini. "Computational Aerodynamic Sensitivity Studies for Generic Delta Wing Planforms". Ed. by Gerd, Krämer Ewald, Wagner Claus, Tropea Cameron, Jakirlić Suad Dillmann Andreas, and Heller. Springer International Publishing, 2020, pp. 338–348.

[81] T. Di Fabbio, K. Rajkumar, E. Tangermann, and M. Klein. "Towards the understanding of vortex breakdown for improved RANS turbulence modeling". *Aerospace Science and Technology* 146 (2024), p. 108973. DOI: 10.1016/j.ast.2024.108973.

[82] O. Reynolds. "An experimental investigation of the circumstances which determine whether the motion of water shall be direct of sinuous, and of the law of resistance in parallel channels". *Philosophical transactions* 174 (1883), pp. 935–982.

[83] A. N. Kolmogorov. "The local structure of turbulence in incompressible viscous fluid for very large Reynolds numbers". *Proceedings of the Royal Society of London. Series A: Mathematical and Physical Sciences* 434 (1890 1991), pp. 9–13. DOI: 10.1098/rspa.1991.0075.

[84] H. Schlichting and K. Gersten. *Boundary-layer theory*. 9th ed. Springer, 2016.

[85] J. L. Lumley and H. Tennekes. "A first course in turbulence". *The statistical fluid mechanics, The MIT Press* (1972).

[86] H. K. Versteeg and W. Malalasekera. *An introduction to computational fluid dynamics*. 1st ed. Longman scientific and technical, 1995.

[87] Jiri Blazek. *Computational fluid dynamics: principles and applications*. Butterworth-Heinemann, 2015.

[88] D. J. Mavriplis and A. Jamesont. "Multigrid Solution of the Navier-Stokes Equations on Triangular Meshes". *AIAA Journal* 28 (8 1989), pp. 1415–1425.

[89] J. Blaze. *Computational Fluid Dynamics: Principles and Applications*. 3rd ed. Butterworth-Heinemann, 2015.

[90] A. Jameson. "Transonic Flow Calculations". *MAE Report* (1983).

[91] D. C. Wilcox. *Turbulence Modeling for CFD*. 3rd ed. DCW Industries Inc, 2006.

[92] A. N. Kolmogorov. "The Local Structure of Turbulence in Incompressible Viscous Fluid for Very Large Reynolds Numbers". *Proceedings: Mathematical and Physical Sciences* 434 (1890 1991), pp. 9–13.

[93] O. Reynolds. "On the dynamical theory of incompressible viscous fluids and the determination of the criterion". *Philosophical Transactions of the Royal Society of London* 186 (1985), pp. 123–164. DOI: https://doi.org/10.1098/rsta.1895.0004.

[94] R. J. Adrian, K. T. Christensen, and Z. C. Liu. "Analysis and interpretation of instantaneous turbulent velocity fields". *Experiments in Fluids* 29 (3 2000), pp. 275–290. DOI: 10.1007/s003489900087.

[95] J. Boussinesq. "Essai sur la th´eorie des eaux courantes". *M´emoires pr´esent´es par divers savants ´a l'Acad´emie des Sciences XXIII* (1877), pp. 1–680.

[96] A. J. Favre. "The equations of compressible turbulent gases". *Institut de Mecanique statistique de la turbulence* (1965).

[97] P. R. Spalart and S. R. Allmaras. "A one-equation turbulence model for aerodynamic flows". *La Recherche aerospatiale* (1 1994), pp. 5–21. DOI: 10.2514/6.1992-439.

[98] S. R. Allmaras, F. T. Johnson, and P. R. Spalart. "Modications and Clarications for the Implementation of the Spalart-Allmaras Turbulence Model". *Seventh International Conference on Computational Fluid Dynamics* (2012), pp. 9–13.

[99] D. C. Wilcox. "Reassessment of the scale-determining equation for advanced turbulence models". *AIAA Journal* 26 (11 1988), pp. 1299–1310. DOI: 10.2514/3.10041.

[100] F. R. Menter. "Two-equation eddy-viscosity turbulence models for engineering applications". *AIAA Journal* 32 (8 1994), pp. 1598–1605. DOI: 10.2514/3.12149.

[101] F. R. Menter. "Zonal two equation k-w turbulence models for aerodynamic flows". American Institute of Aeronautics and Astronautics Inc, AIAA, 1993. DOI: 10.2514/6.1993-2906.

[102] J. Smagorinsky. "General circulation experiments with the primitive equations". *Monthly weather review* 91 (3 1963).

[103] J. W. Deardorff. "A numerical study of three-dimensional turbulent channel flow at large Reynolds numbers". *Journal of fluid mechanics* 41 (2 1970), pp. 453–480.

[104] U. Schumann. "Subgrid-scale model for finite difference simulation of turbulent flows in plane channels and annuli". *Journal of computational physics* 18 (4 1975), pp. 376–404.

[105] Y. Zhiyin. "Large-eddy simulation: Past, present and the future". *Chinese Journal of Aeronautics* 28 (1 2015), pp. 11–24. DOI: 10.1016/j.cja.2014.12.007.

[106] U. Piomelli. "Wall-layer models for large-eddy simulations". *Progress in Aerospace Sciences* 44 (6 2008), pp. 437–446. DOI: 10.1016/j.paerosci.2008.06.001.

[107] P. R. Spalart, S. Deck, M. L. Shur, K. D. Squires, M. Kh Strelets, and A. Travin. "A new version of detached-eddy simulation, resistant to ambiguous grid densities". *Theoretical and Computational Fluid Dynamics* 20 (3 2006), pp. 181–195. DOI: 10.1007/s00162-006-0015-0.

[108] R. H. Kraichnan. "Diffusion by a random velocity field". *Physics of Fluids* 13 (1 1970), pp. 22–31. DOI: 10.1063/1.1692799.

[109] Hans Reichardt. "Vollständige Darstellung der turbulenten Geschwindigkeitsverteilung in glatten Leitungen". *ZAMM-Journal of Applied Mathematics and Mechanics/Zeitschrift für Angewandte Mathematik und Mechanik* 31.7 (1951), pp. 208–219.

[110] K. Rajkumar, E. Tangermann, and M. Klein. "Efficient Scale-Resolving Simulations of Open Cavity Flows for Straight and Sideslip Conditions". *Fluids* 8 (8 2023), p. 227. DOI: 10.3390/fluids8080227.

[111] A. N. Kolmogorov. "The Local Structure of Turbulence in Incompressible Viscous Fluid for Very Large Reynolds Numbers." *Doklady Akademii Nauk SSSR* 30 (1941), pp. 301–304.

[112] J. C. Kok. "A High-Order Low-Dispersion Symmetry-Preserving Finite-Volume Method for Compressible Flow on Curvilinear Grids". *Journal of Computational Physics* 228 (18 2009), pp. 6811–6832.

[113] A. Jameson, W. Schmidt, and E. Turkel. "Numerical solution of the Euler equations by finite volume methods using Runge Kutta time stepping schemes". *AIAA Journal* (1981). DOI: 10.2514/6.1981-1259.

[114] M. Galle, T. Gerhold, and J. Evans. "Parallel Computation of Turbulent Flows around Complex Geometries on Hybrid Grids with the DLR-Tau Code". *11th Parallel CFD Conference* (1999).

[115] W. Sutherland. "The viscosity of gases and molecular force". *The London, Edinburgh, and Dublin Philosophical Magazine and Journal of Science* 36 (223 1893), pp. 507–531. DOI: 10.1080/14786449308620508.

[116] T. Di Fabbio, E. Tangermann, and M. Klein. "Transonic aerodynamic investigation on a triple-delta wing in side slip conditions". *CEAS Aeronautical Journal* 13 (2 2022), pp. 453–470.

[117] J. R. Forsythe, W. Z. Strang, and K. A. Hoffmann. "Validation of several reynolds-averaged turbulence models in a 3-D unstructured grid code". American Institute of Aeronautics and Astronautics Inc., 2000. DOI: 10.2514/6.2000-2552.

[118] K. Rajkumar, E. Tangermann, M. Klein, S. Ketterl, and A. Winkler. "Time-efficient simulations of fighter aircraft weapon bay". *CEAS Aeronautical Journal* (2023). DOI: 10.1007/s13272-022-00630-1.

[119] K. Rajkumar, E. Tangermann, M. Klein, S. Ketterl, and A. Winkler. "DES of Weapon Bay in Fighter Aircraft Under High-Subsonic and Supersonic Conditions". *Notes on Numerical Fluid Mechanics and Multidisciplinary Design* 151 (2021), pp. 656–665. DOI: 10.1007/978-3-030-79561-0_62.

[120] J. Lowe, A. Probst, T. Knopp, and R. Kessler. "Low-dissipation low-dispersion second-order scheme for unstructured finite volume flow solvers". Vol. 54. American Institute of Aeronautics and Astronautics Inc., 2016, pp. 2961–2971. DOI: 10.2514/1.J054956.

[121] T. Handa, H. Miyachi, H. Kakuno, and T. Ozaki. "Generation and propagation of pressure waves in supersonic deep-cavity flows". *Experiments in Fluids* 53 (6 2012), pp. 1855–1866. DOI: 10.1007/s00348-012-1400-7.

[122] J. C. R. Hunt, A. A. Wray, and P. Moin. "Eddies, Streams and convergence zones in turbulent flows". *Technical Report CTR-S88, Center for turbulence research* (1988), pp. 193–208.

[123] I. M. Kalkhoran and M. K. Smart. "Aspects of shock wave-induced vortex breakdown". *Progress in Aerospace Sciences* 36 (2000), pp. 63–95.

[124] R. E. Spall, T. B. Gatski, and C. E. Grosch. "A criterion for vortex breakdown." *Physics of fluids* 30 (11 , Nov. 1987 1987), pp. 3434–3440. DOI: 10.1063/1.866475.

[125] B. A. Robinson, R. M. Barnett, and S. Agrawal. "Simple numerical criterion for vortex breakdown". *AIAA Journal* 32 (1 1994), pp. 116–122. DOI: 10.2514/3.11958.

[126] A. N. Lipatnikov, S. Nishiki, and T. Hasegawa. "A direct numerical simulation study of vorticity transformation in weakly turbulent premixed flames". *Physics of Fluids* 26 (10 2014). DOI: 10.1063/1.4898640.

[127] G. Erlebacher, M. Y. Hussaini, and C. W. Shu. "Interaction of a shock with a longitudinal vortex". *Journal of Fluid Mechanics* 337 (1997), pp. 129–153. DOI: 10.1017/S0022112096004880.